

# COMPOSITE NANOPARTICLES FOR BIOMEDICAL APPLICATIONS

by

ANDREY ZAKHARCHENKO

(Under the Direction of Sergiy Minko)

## ABSTRACT

Cancer remains a second leading cause of death in the United States, according to recent statistics<sup>1</sup>. There is an immediate demand for targeted delivery to affected tissues that will allow to decrease therapeutic dose, lower toxicity and manage side effects. Recently, there was a significant rise of interest on development and applications of composite nanomaterials. These materials hold unique chemical and physical properties for applications in biotechnology, medicine and pharmaceuticals. Advancements in synthetic methods led to rise of multifunctional nanomaterials that could simultaneously be used for multiple applications such as active targeting, medical imaging or drug delivery. The aim of current work was to expand recent findings and accomplishments and develop a drug delivery system for biomedical uses. Synthetic routes and strategies were designed to obtain well-defined and reproducible core-shell superparamagnetic nanoparticles. The nanomaterial is based on magnetite core, amorphous silica shell and polymer brush coating capable of carrying biomolecules. The system demonstrated magnetically-triggered catalytic activity with a well-controlled drug release with significant efficiency against cancer cells.

INDEX WORDS: Nanoparticles, Drug delivery, Enzymatic Catalysis, Cancer Cells

COMPOSITE NANOPARTICLES FOR BIOMEDICAL APPLICATIONS

by

ANDREY ZAKHARCHENKO

B.S., Moscow State University, Russia, 2009

M.S., Moscow State University, Russia, 2011

A Thesis Submitted to the Graduate Faculty of The University of Georgia in Partial Fulfillment  
of the Requirements for the Degree

DOCTOR OF PHILOSOPHY

ATHENS, GEORGIA

2018

© 2018

Andrey Zakharchenko

All Rights Reserved

# COMPOSITE NANOPARTICLES FOR BIOMEDICAL APPLICATIONS

by

ANDREY ZAKHARCHENKO

Major Professor:      Sergiy Minko

Committee:            Suraj Sharma  
                              Ian R. Hardin  
                              Leidong Mao

Electronic Version Approved:

Suzanne Barbour  
Dean of the Graduate School  
The University of Georgia  
May 2018

## ACKNOWLEDGEMENTS

First of all, I would like to give a special thanks to Prof. Sergiy Minko for giving me the opportunity to work and study in his group and supervising me during my PhD program. It was my pleasure to work and study at the University of Georgia in the Nanostructured Materials Lab under supervision of Dr. Minko with his continuous support, motivating and mentoring. I would like to thank current and past members of Minko's group for their wonderful attitude, support, great cooperation and all the good memories. I would also like to thank my good colleague, friend and collaborator, Dr. Evgeniy Katz for his continuous help, constructive discussions and advices.

## TABLE OF CONTENTS

	Page
ACKNOWLEDGEMENTS .....	IV
LIST OF TABLES .....	VII
LIST OF FIGURES .....	VIII
CHAPTER	
1 INTRODUCTION .....	1
2 MAGNETIC NANOPARTICLES .....	4
2.1 Synthesis of Magnetic Nanoparticles.....	7
2.2 Stabilization of Magnetic Nanoparticles.....	12
3 POLYMER MODIFICATION .....	17
3.1 Thin polymer films .....	17
3.2 Synthesis of polymer brushes .....	19
4 BIOMEDICAL APPLICATIONS.....	24
5 MAGNETIC FIELD REMOTELY CONTROLLED HIGHLY-SELECTIVE BIOCATALYSIS.....	30
5.1 Design of biocatalytic nanoparticles.....	34
5.2 Magnetic-field-controlled biocatalysis .....	39
5.3 Magnetic-field-controlled drug release.....	43

6	EXPERIMENTAL DETAILS .....	49
6.1	Synthesis of magnetite–silica core–shell nanoparticles .....	50
6.2	Labelling of the nanoparticles with fluorescent dyes .....	51
6.3	Grafting of PAA-b-PPEGMA block copolymer from the nanoparticle surface .....	53
6.4	Functionalization of nanoparticles with proteins and DOX .....	56
6.5	Aggregation of particles in magnetic field.....	60
6.6	Smart compartmentalization .....	61
6.7	Experiments with cell culture .....	62
6.8	Characterization of the Polymer Brushes .....	64
6.9	Evaluation of biocatalytic activity of the conjugated enzymes .....	69
6.10	Gel-electrophoresis method for testing of biocatalytic proteolysis of S- nanoparticles .....	72
6.11	Spectroscopic estimation of loading and release of dox .....	74
6.12	Cell viability.....	75
7	CONCLUSIONS.....	79
8	FUTURE STUDIES.....	81
	REFERENCES .....	83

## LIST OF TABLES

	Page
<b>Table 1:</b> Structure and characteristics of biocatalytic NP .....	34
<b>Table 6.1:</b> Molecular characteristics of the polymer brushes grafted from the surface of silica particles and Si-wafers .....	65
<b>Table 6.2:</b> Loading of E- and S-nanoparticles.....	59
<b>Table 6.3:</b> Kinetic experiments for proteolysis of FD-BSA by Papain-PAA .....	71



## LIST OF FIGURES

	Page
Figure 2.1: Hysteresis loops of magnetic materials .....	4
Figure 2.2: Scanning electron microscopy of 40 nm magnetite cubical nanoparticles .....	8
Figure 2.3: Transmission electron microscopy of 10 nm magnetite nanoparticles obtained by emulsion synthesis .....	9
Figure 2.4: Transmission electron microscopy of 10 nm magnetite nanoparticles obtained by thermal decomposition synthesis .....	10
Figure 2.5: Transmission electron microscopy of 12 nm magnetite nanoparticles .....	11
Figure 2.6: Silica condensation reaction by Stöber process in ethanol.....	13
Figure 2.7: Transmission electron microscopy of silica coated single magnetic nanoparticles ....	14
Figure 2.8: Transmission electron microscopy of silica coated magnetic nanoparticles.....	15
Figure 2.9: General schematics of silane chemistry .....	16
Figure 3.1: Polymer chains at different grafting density and solvent conditions .....	17
Figure 3.2: Schematic illustration of possible morphologies of polymer brushes.....	19
Figure 3.3: Schematics of “grafting to” and “grafting from” approaches to functionalize silica- coated magnetic nanoparticles .....	20
Figure 3.4: Amide linkage formation between the carboxylic group on the particle surface and the amino group .....	21
Figure 3.5: The mechanism of ATRP .....	22
Figure 4.1: Schematic of cells interaction with thermosresponsible pNIPAM brush.....	26

Figure 4.2: Schematic of the enzymogel nanoparticle. a) swollen PAA at pH 7 b) shrunken PAA brush at pH 7 and pH 4.5, respectively. c) The brush is uniformly loaded with CEL enzymes at pH 4.5 .....	27
Figure 5.1 E- and S-type superparamagnetic nanoparticles carrying the enzyme and the substrate . .....	35
Figure 5.2: Monitoring of the magnetic-field-triggered release of fluorescein dye .....	37
Figure 5.3: Chains of biocatalytic nanoparticles.....	38
Figure 5.4: Magnetically controlled release of the drug .....	40
Figure 5.5: Magnetic-field-triggered blocking of cancer cell proliferation .....	42
Figure 5.6: Magnetic-field-triggered biocatalysis in the cell culture.....	45
Figure 6.1: Characterization of magnetic nanoparticle.....	52
Figure 6.2: Schematic of the synthesis of functional NPs .....	54
Figure 6.3: DLS particle analysis in aqueous dispersions at pH 7.5.....	55
Figure 6.6: Reference experiments for the nanoparticles with no dark-brown iron oxide core for improved color contrast .....	56
Figure 6.7: DOX release monitored with fluorescence spectroscopy.....	58
Figure 6.8: Schematic for the fluorescence spectroscopic analysis of the DOX conjugation and release .....	59
Figure 6.12: TEM images of NPs aggregates .....	60
Figure 6.16: Fluorescent microscopy images of 4T1 cell with internalized S-particles.....	63
Figure 6.4: DLS measurements of silica nanoparticles in aqueous suspensions .....	66
Figure 6.5: AFM analysis of silica particles .....	67
Figure 6.9: Concentration of papain in the dialysis flask .....	69

Figure 6.10: Kinetics of proteolysis of FD-BSA catalyzed by Papain-PAA conjugates.....	70
Figure 6.11: Kinetics of proteolysis of FD-BSA catalyzed by Papain-PAA.....	71
Figure 6.13: Proteolysis of FD-BSA (500 $\mu$ g) in PBS buffer solution.....	72
Figure 6.14: Release of products of proteolytic process.....	73
Figure 6.15: Release of products of proteolytic process.....	73
Figure 6.18: Cell viability: reference experiments with no magnetic field applied.....	75
Figure 6.19: Cell viability .....	76
Figure 6.17: Blocking cancer cell proliferation .....	77

## CHAPTER 1

### INTRODUCTION

In recent decades, there was a significant rise of interest on development and applications of nanoparticles<sup>2-4</sup>. These materials hold unique chemical and physical properties and hold a tremendous potential for scientific and industrial applications in biotechnology<sup>5,6</sup>, medicine<sup>7-9</sup> and pharmaceuticals<sup>10,11</sup>. Nanomaterial properties, such as biocompatibility, biodegradability, size, shape, composition, and surface morphology, could be controlled by tuning synthetic conditions, opening vast possibilities to create novel materials with desired characteristics<sup>12,13</sup>. Thus, advancement in formulation of materials with well-defined properties depends on successful selection of synthesis steps. Synthesis of composite nanomaterials is usually a multistep procedure that utilizes a combination of inorganic and organic chemistry methods. Different approaches could be used for synthesis, coating, and stabilization of nanoparticles. The use of biocompatible and biodegradable materials for synthesis and stabilization will lead to creation of new bio-safe materials<sup>14,15</sup>. Currently, the application of polymer for surface modification of materials is the most developed and broadly used approach to generate versatile materials with controlled physical and chemical interfacial properties. Advancement in controlled polymerization methods, such as atom transfer radical polymerization (ATRP), led to rise of novel nanomaterials with multifunctional applications for active targeting, medical imaging or drug delivery<sup>16,17</sup>.

The thesis consists of literature review describing superparamagnetic phenomena, main synthetic routes and strategies to obtain superparamagnetic nanoparticles, routes for their coatings and functionalization for biomedical applications.

This work is focused on development of novel drug delivery system based on composite nanoparticles. This platform combines two different kinds of core-shell magnetic nanoparticles: one loaded with enzymes and another with substrate-bound therapeutic molecules. Both cargos are shielded with a polymer brush structure of the nanoparticle shell, which prevents any kind of enzyme-substrate interactions by steric repulsion. The shield's barrier is overcome when a relatively weak external magnetic field is applied, and the enzyme and the substrate are merged and forced to interact in the generated nanocompartment. The merged biocatalytic nanoparticles liberate the substrate-bound therapeutic drugs when the enzymes degrade the substrate. The developed platform provides a proof-of-concept for a remotely-controlled release of drugs by using energy of a noninvasive weak magnetic field. Significant efficiency against cancer cell models was demonstrated with promising potential for magnetically guided targeted delivery of therapeutic drugs.

The aim of the current work is the development of a novel drug delivery system based on composite nanoparticles. This platform combines two different kinds of core-shell magnetic nanoparticles: one loaded with enzymes and another - with substrate-bound therapeutic molecules. Both cargos are shielded with a polymer brush structure of the nanoparticle shell, which prevents any kind of uncontrolled enzyme-substrate interactions. The shield's barrier is overcome when a relatively weak external magnetic field is applied and the enzyme and the substrate carrying nanoparticles are merged and forced to interact in the generated nanocompartment in the merged areas. The merged biocatalytic nanoparticles liberate the

substrate-bound therapeutic drugs when the enzymes degrade the substrate. The developed platform provides a proof-of-concept for a remotely-controlled release of drugs by using energy of a noninvasive weak magnetic field. Significant efficiency against cancer cell models was demonstrated with the promising potential for advanced targeted delivery of therapeutic drugs.

## CHAPTER 2

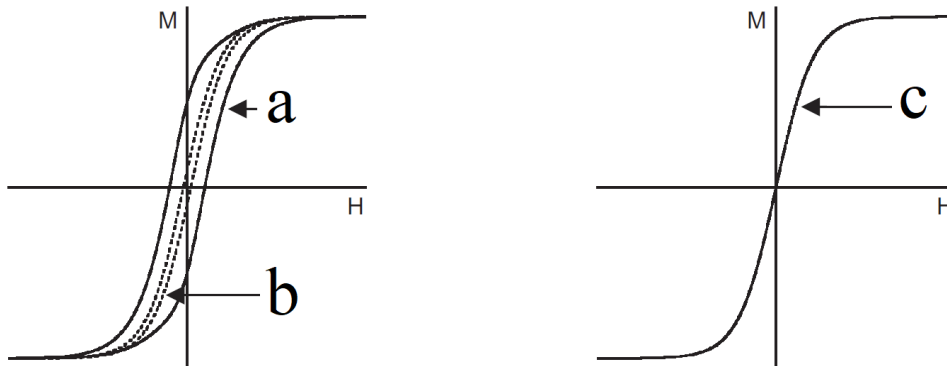
### MAGNETIC NANOPARTICLES

Magnetic nanoparticles stand out as one of the most important classes of nanomaterials and used in many applications due to their unique and tunable magnetic properties<sup>2,9</sup>. A great variety of magnetic nanoparticles of different shapes, sizes and compositions were synthesized<sup>18</sup>.

Nanoparticles with superparamagnetic properties (such as Fe, Ni, Co) found the most widespread use due to their magnetic characteristics, simple synthesis and biocompatibility<sup>19,20</sup>. To better understand the properties of magnetic nanoparticles, it is important to give brief overview of magnetism phenomena<sup>21,22</sup>.

Magnetism originates from the atom's electron spin and orbital electron motion around the nucleus. The total magnetic moment of the given atom is the sum of all orbital and spin magnetic moments. When material is placed in a magnetic field with the strength  $H$ , individual magnetic moments will contribute to the overall response and the magnetic induction will be:

$$B = \mu_0(H + M)$$



**Figure 2.1.** Hysteresis loops of magnetic materials: **a**- small particles, **b**- large particles, and **c**- superparamagnetic particles (with permission 03 Appl. Phys. 36 R167)

where  $\mu_0$ - is the permeability of the media,  $\mathbf{M} = \mathbf{m}/V$  is the magnetization (the magnetic moment  $\mathbf{m}$  per unit volume  $V$ ) of the material. In general, all materials exhibit magnetic properties when placed in magnetic field  $\mathbf{H}$  and could be characterized in terms of magnetic susceptibility,  $\chi$ :

$$\mathbf{M} = \chi \mathbf{H}$$

where  $\mathbf{M}$  is the magnetization induced by the magnetic field. Depending on  $\mathbf{M}$ , all materials are classified as paramagnets for which  $10^{-6} < \chi < 10^{-1}$  or diamagnets, when  $10^{-6} < \chi < 10^{-3}$ . There are, however, some materials that show magnetization values several orders of magnitude higher, up to  $10^4$  times and classified as ferromagnets. Susceptibility of magnetic materials depends on the temperature and strength of the external magnetic field<sup>23</sup>. These materials characterized by distinctive sigmoidal  $\mathbf{M}$ - $\mathbf{H}$  curves, where  $\mathbf{M}$  approaches the saturation at high  $\mathbf{H}$  values. The shape of these loops is determined by the material's structure such as impurities and grain boundaries inside the particle. In small particles, there is a single domain ground state which leads to a broader hysteresis loop (*Fig. 2.1A*). In larger particles, such as 1  $\mu\text{m}$  and larger, multiple domains give rise to a narrow hysteresis loop (*Fig. 2.1B*) since it takes less energy to move domain walls. When particle size is in nanometers (less than 50 nm), a superparamagnetic effect is observed, where the magnetic moment of the entire particle fluctuates under the influence of the thermal energy, but individual atomic moments remain in an ordered state in relevance to each other. This leads to the sigmoidal and anhysteretic curve (*Fig. 2.1B*) with an extremely low relaxation time so their magnetic moments are quickly reoriented after the magnetic field is removed.

It is important to understand the magnetic behavior of nanoparticles to foresee their behavior in biological systems. Depending on the particle's size, the material will exhibit a multidomain,



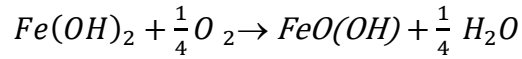
single domain or superparamagnetic behavior. For larger particles, the energy delivered by the external field is characterized by the area enclosed in the hysteresis loop. This effect is used in the method called “hyperthermia”, where particles are localized at the area of interest and a time-varying magnetic field is applied, providing a constant flow of energy. The magnetic field energy is converted into the thermal energy and could be used to suppress surrounding tissues (for example cancer) or trigger a response from the particles, such as thermosensitive materials<sup>24</sup>. Another widespread application is magnetic separation, when large multi-domain particles are used to separate biomolecules or cells<sup>25</sup>. It has proven to be a highly sensitive method to isolate single rare cells from the blood<sup>26</sup>, small amounts of DNA<sup>27</sup> and protein molecules<sup>28</sup>. Separation by magnetic beads has been successfully applied in many areas of biological research and undergone progressive commercialization<sup>29</sup>.

Superparamagnetic particles (SPM) are widely used as drug delivery carriers owing to their biocompatibility, biological stability, long circulation time and simple functionalization methods<sup>15</sup>. Unmodified nanoparticles larger than 30 nm are rapidly uptaken by liver and spleen, while particles of 10 nm or less in diameter have a much longer half-life in the blood and are collected by reticuloendothelial cells<sup>30,31</sup>. Cancer cells do not possess an effective reticuloendothelial system as healthy cells, so they have increased uptake levels of particles. Another successful application of superparamagnetic material is MRI contrast enhancement<sup>12,32,33</sup>. During the MRI measurement, nanoparticles are saturated by the external magnetic field, establishing a substantial local magnetic field that leads to decrease of the total relaxation time comparing to untreated samples. SPM particles have also been used for vascular imaging, cell labeling and monitoring gene expression with the aid of MRI<sup>34-37</sup>.

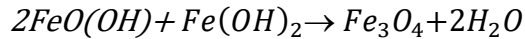
## 2.1 Synthesis of Magnetic Nanoparticles

Iron oxide nanoparticles were extensively used in many biological applications due to straightforward synthesis, modification, biocompatibility and colloidal stability. Iron oxide nanoparticles below 30 nm in diameter exhibit superparamagnetic behavior. The main synthetic routes for iron oxide particles include controlled reduction<sup>38,39</sup>, emulsion<sup>40</sup>, salt precipitation<sup>41,42</sup> and thermal decomposition<sup>43</sup> methods. The nanoparticles are formed in two stages: nucleation of seeds and nanoparticles growth<sup>44</sup>.

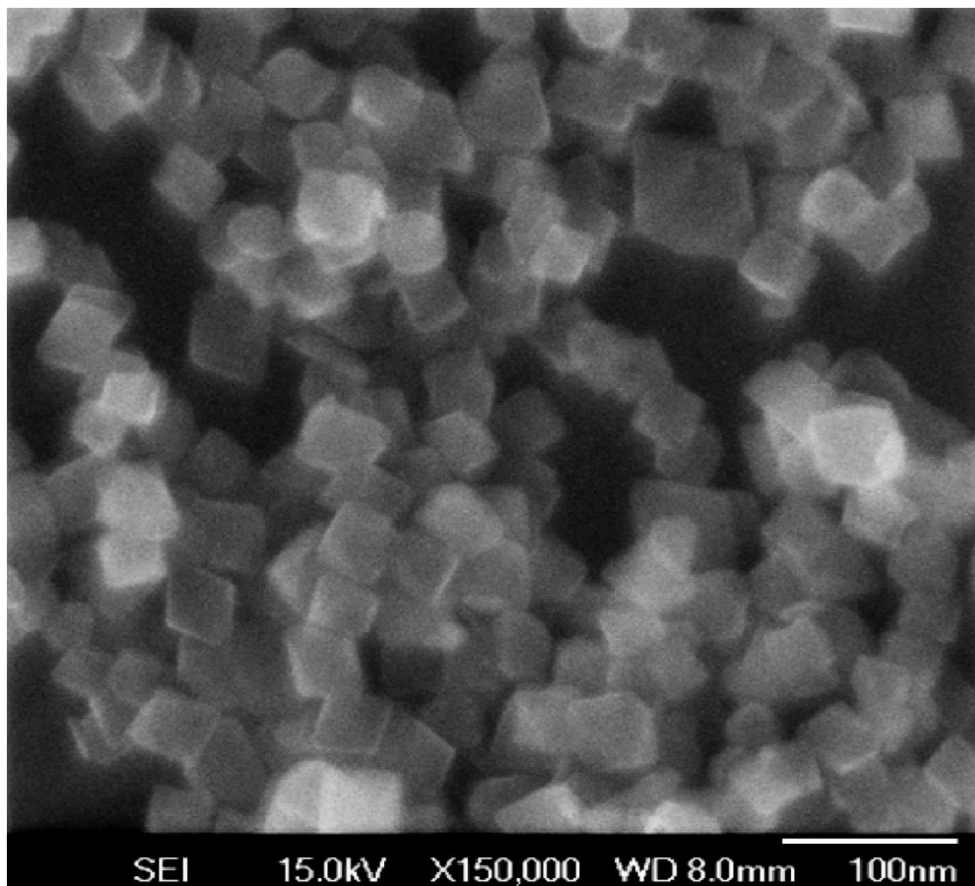
Reduction method is used to produce magnetite nanoparticles from iron hydroxide in the presence of nitrate ions. This method consists of two steps: first, iron chloride (II) is dissolved in water under stirring; sodium hydroxide is added to precipitate  $Fe(OH)_2$  while oxygen is bubbled through the reactor:



The suspension is heated at 70-100°C under mechanical stirring; magnetite is formed according to the reaction:



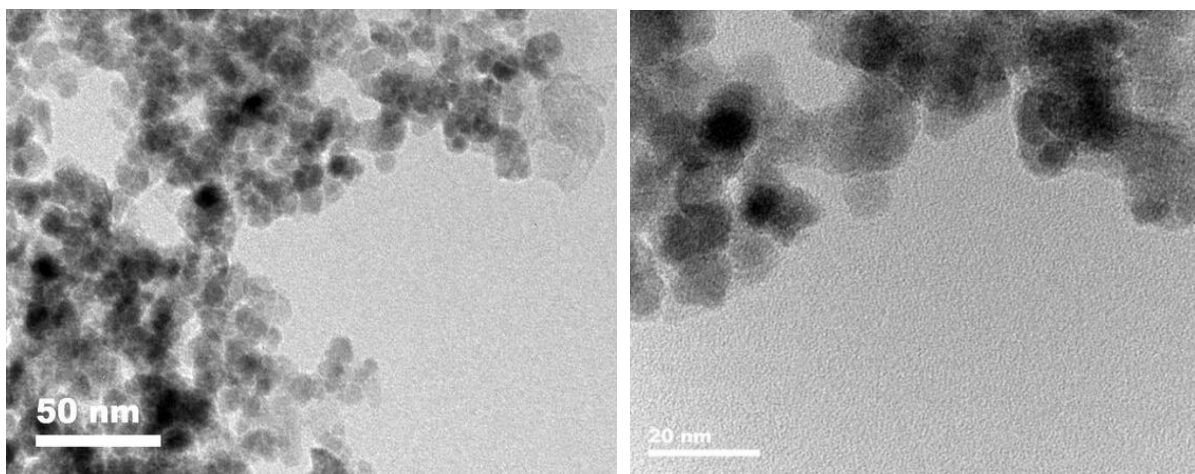
It is difficult to control size and geometry of synthesized particles. Nanoparticles with a diameter ranging from 10 nm to 1µm could be obtained by this method by varying the reaction temperature, incubation time and iron salt. A scanning electron microscopy image of nanoparticles prepared by this technique is shown in Figure 2.



**Figure 2.2.** *Scanning electron microscopy of 40 nm magnetite cubical nanoparticles*

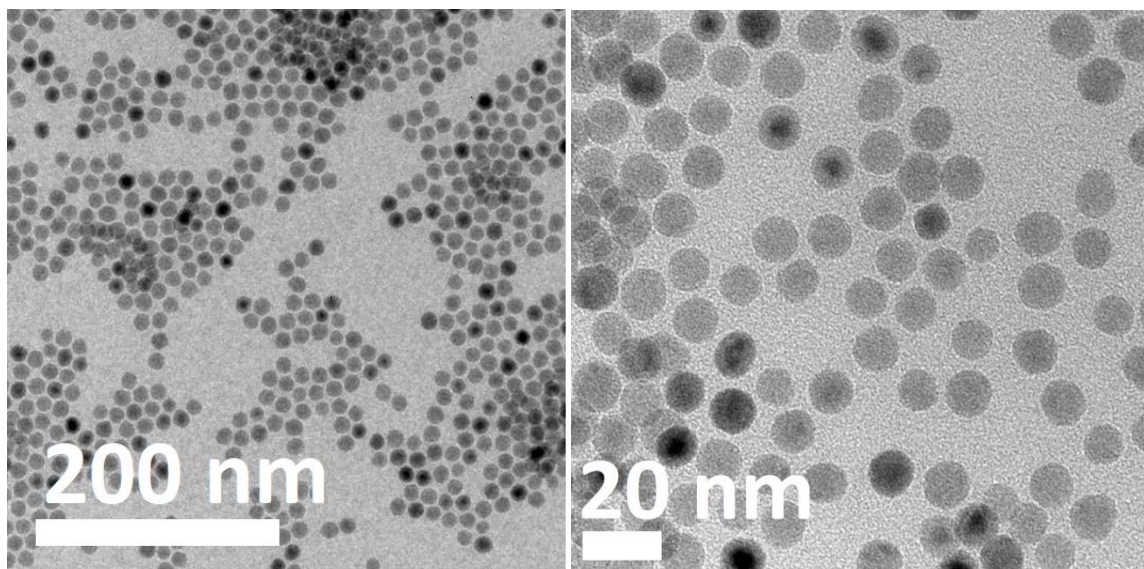
Emulsion synthesis of magnetite nanoparticles consists of the preparation of nanosized water droplets in oil phase stabilized by surfactant molecules. These nanoreactors regulate nanoparticles nucleation, growth and agglomeration. The advantage of this technology is a flexibility in selection of surfactants, oil, reaction conditions. The method is also used to form a shell (coatings) for the synthesis of composite nanoparticles in “one pot”<sup>44</sup>. For the synthesis of iron oxide nanoparticles cetyltrimethylammonium bromide (CTAB) surfactant was dissolved in toluene under mechanical stirring. Water solution of  $FeCl_2 + FeCl_3$  was slowly added by droplets to form water in toluene emulsion.

After 12 hours of stirring, ammonium hydroxide was added, and solution turned black as magnetite forms. Obtained nanoparticles are precipitated by addition of acetone to destabilize the emulsion and washed with ethanol to remove unreacted species. Particles were analyzed with DLS, TEM and measured to be  $10 \pm 3$  nm in size. The analysis of TEM images (Fig.3) showed a consistent spherical structure of the obtained nanoparticles. The disadvantage of this method is associated with residual surfactants and difficulties to scale-up the synthesis.



**Figure. 2.3.** *Transmission electron microscopy of 10 nm magnetite nanoparticles obtained by emulsion synthesis*

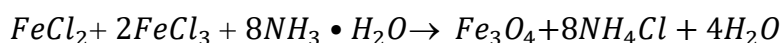
Thermal decomposition is the method of nanoparticles synthesis from organometallic precursors in organic solvents with surfactant capping agents in an inert atmosphere. The method could be used for synthesis of various metal oxide particles. The thermal decomposition method provides great control over size, shape, polydispersity and composition<sup>45</sup> of nanoparticles. In a typical magnetite synthesis protocol, iron (III) acetylacetonate is added to the mixture of oleylamine and benzyl ether under stirring in room temperature. Benzyl ether serves as a high temperature



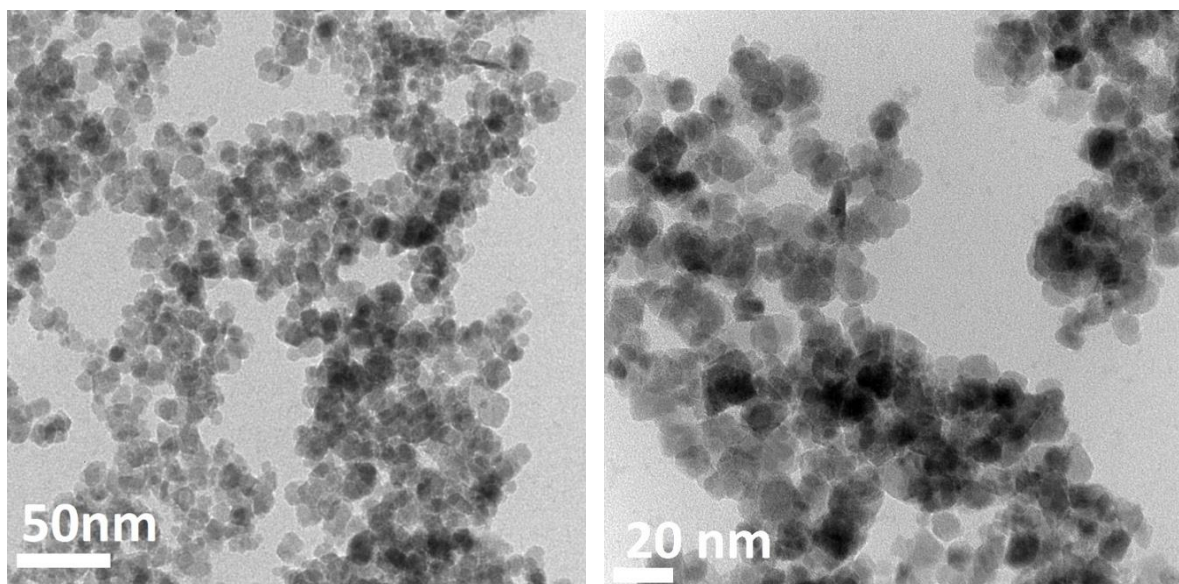
**Figure 2.4.** *Transmission electron microscopy of 10 nm magnetite nanoparticles obtained by thermal decomposition synthesis*

organic solvent for iron precursor and oleylamine serves as mild base and stabilizes nanoparticles. During the reaction, the solution turns black. The solution is cooled to room temperature and the particles are precipitated by addition of ethanol. The nanoparticles are separated by centrifugation at 10000 rpm, washed three times with ethanol and transferred to an organic solvent, hexane for example, to form a stable dispersion. The particles were characterized by DLS and TEM. The measured diameter was 12 nm with a very low polydispersity (*Fig. 4*). The disadvantage of this method is that the synthesized particles are dispersed in organic solvent while for the most biological applications aqueous dispersions are preferential. To overcome this problem, nanoparticles are transferred into an aqueous media by dispersing particles in chloroform and adding the dispersion to the equal volume of aqueous CTAB solution under mechanical stirring. After 12 hours, the largest fraction of the nanoparticles is transferred to the aqueous phase and could be extracted by precipitation or using a magnet.

Salt coprecipitation technique is one of the most widely used to prepare magnetite nanoparticles of a diameter of 12-15 nm (Fig.5). The nanoparticles formation is based on the precipitation of  $\text{Fe}_3\text{O}_4$  by hydrolysis of iron chloride (II) and iron chloride (III) in ratio 2:3 at basic media under mechanical stirring:



A black precipitate is formed immediately upon mixing and collected using a magnet. To stabilize nanoparticles, the surface charge is switched from negative to positive by washing the precipitate with nitric acid and then trisodium citrate while maintaining a highly acidic pH. After washing with water, the particles form a highly stable dispersion of the nanoparticles with superparamagnetic properties measured by magnetic relaxometry. The dispersion is stable for many months, however, after a 2-month incubation time partial oxidation occurs. This method allows to obtain large amounts of highly stable magnetic nanoparticles in an aqueous media. By varying reaction parameters such as a base ( $\text{NH}_4\text{OH}$ ,  $\text{NaOH}$ ,  $\text{KOH}$ ), reaction time, iron salts ratio,



**Figure 2.5.** Transmission electron microscopy of 12 nm magnetite nanoparticles

or addition of other metal salts (Mg, Mn) it is possible to tune final particles properties: size, shape and composition.

Magnetic nanoparticles could also be obtained by variety of other methods such as hydrothermal synthesis<sup>46</sup>, laser pyrolysis<sup>47</sup>, spray synthesis<sup>48</sup> and electrochemical synthesis<sup>49</sup>. Although these methods could achieve good quality nanoparticles, they require the use of complex equipment and very sensitive to the selection of solvents. Synthesis methods based on reduction of metal salts in aqueous solutions became most popular due to their simplicity, a high speed of reaction and good control of nanoparticles' size, in some cases shape, and morphology. In most cases, synthesized metal nanoparticles tend to form polydisperse aggregates and require additional stabilization.

## **2.2 Stabilization of Magnetic Nanoparticles**

The major methods of stabilization of nanoparticle dispersion employ the mechanism of electrostatic, sterical or combined stabilization.

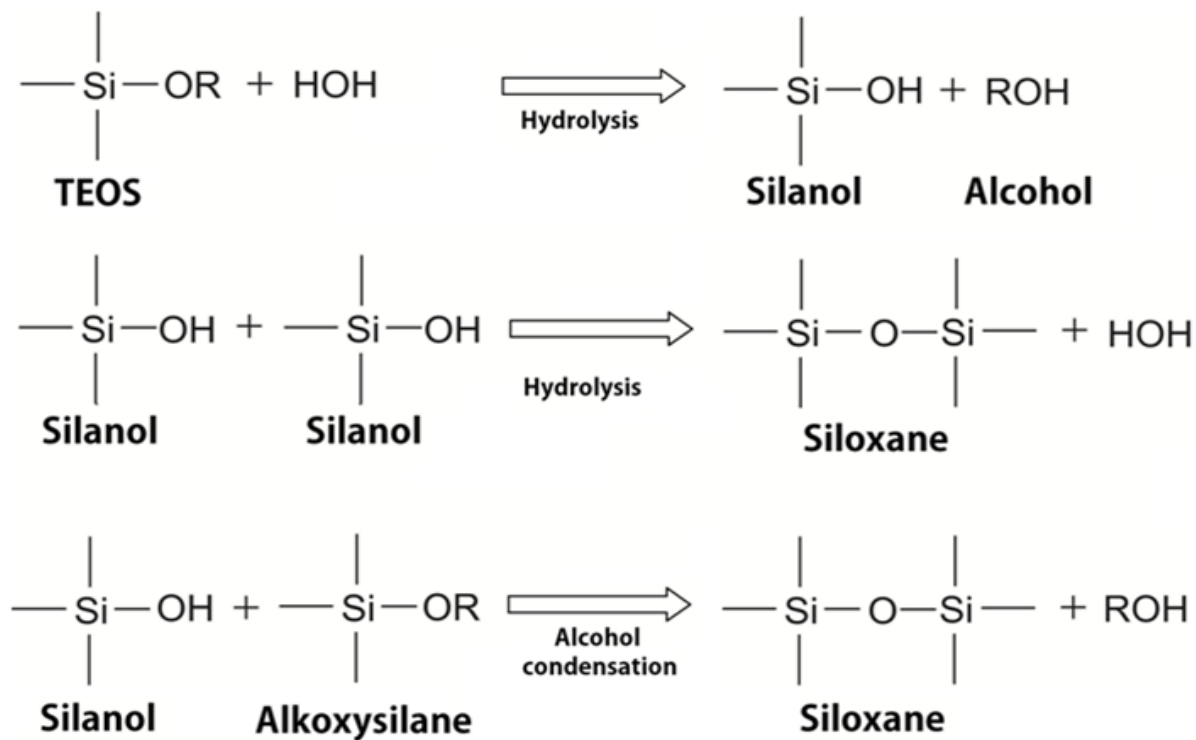
Electrostatical stabilization is achieved by ionizable molecules that adsorb on the surface of the particles. The adsorbed ions form an electrical double layer that stabilizes nanoparticles owing to a the Coulombic repulsion. The classical example is the synthesis of noble metal nanoparticles (gold, platinum, palladium) in the presence of citrate salts to achieve a stable dispersion of 1-2 nm particles without aggregation.<sup>50,51</sup>

Sterical stabilization is based on the functionalization of the nanoparticles surface by large-size molecules such as surfactants or polymers, which form steric barriers and prevent the close contact between individual nanoparticles<sup>52,53</sup> Using ionizable polymers or surfactants allows to combine both mechanisms of stabilization<sup>54</sup>. This method is also used to form multifunctional liposomes<sup>55</sup>. The disadvantage of this approach is that surfactants are not strongly bound to the

particle surface. Surfactant desorption could lead to partial aggregation. A solution of this problem relies on the encapsulation of nanoparticles with strongly bound shell made of organic, inorganic, polymeric or biomolecules<sup>56,57</sup>. The structure and composition of the stabilizing shell greatly influences the particles properties. Most advanced coatings are composite organic-inorganic shells when organic and inorganic layer serve for specific purposes<sup>58</sup>. Inorganic components can control nanoparticle size, chemical and biological stability. Polymer components are responsible for surface properties, steric stabilization, temperature response, and rheological properties of the dispersions.

A stabilizing shell made of silica is broadly used for magnetic nanoparticle encapsulation.

Synthesis of silica shell is simple and reproducible allowing to achieve stable nanoparticles in a variety of sizes from 30 nm to 1  $\mu\text{m}$ . The encapsulation process is based on the Stöber method, that is used in nanotechnology for over 50 years since its introduction in 1968<sup>59</sup>.

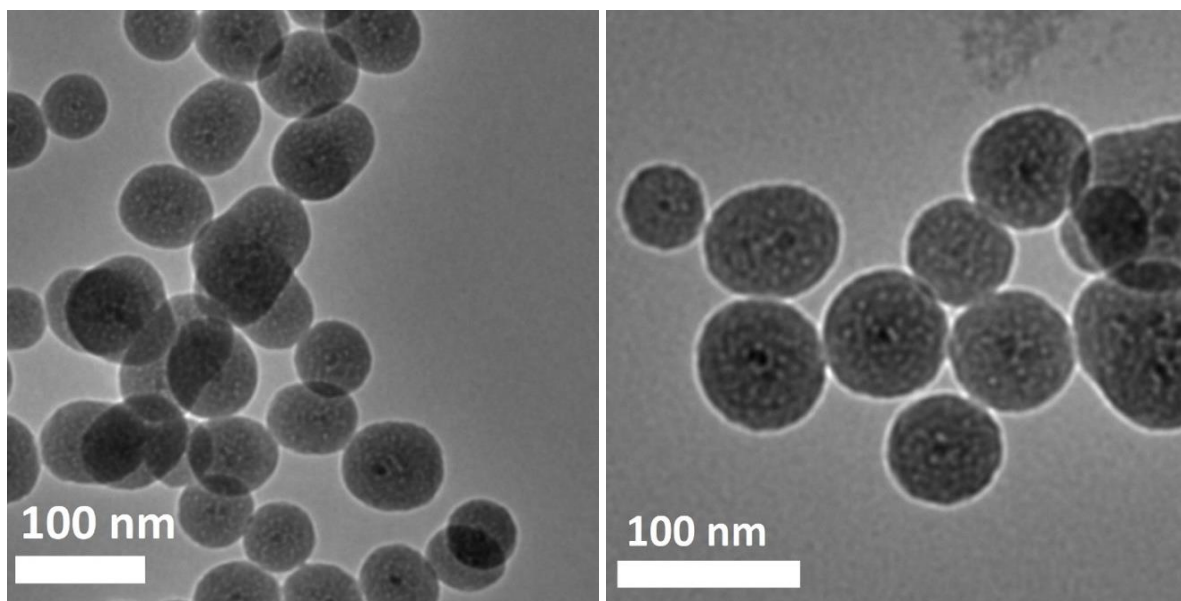


**Figure 2.6.** Silica condensation reaction by Stöber process in ethanol

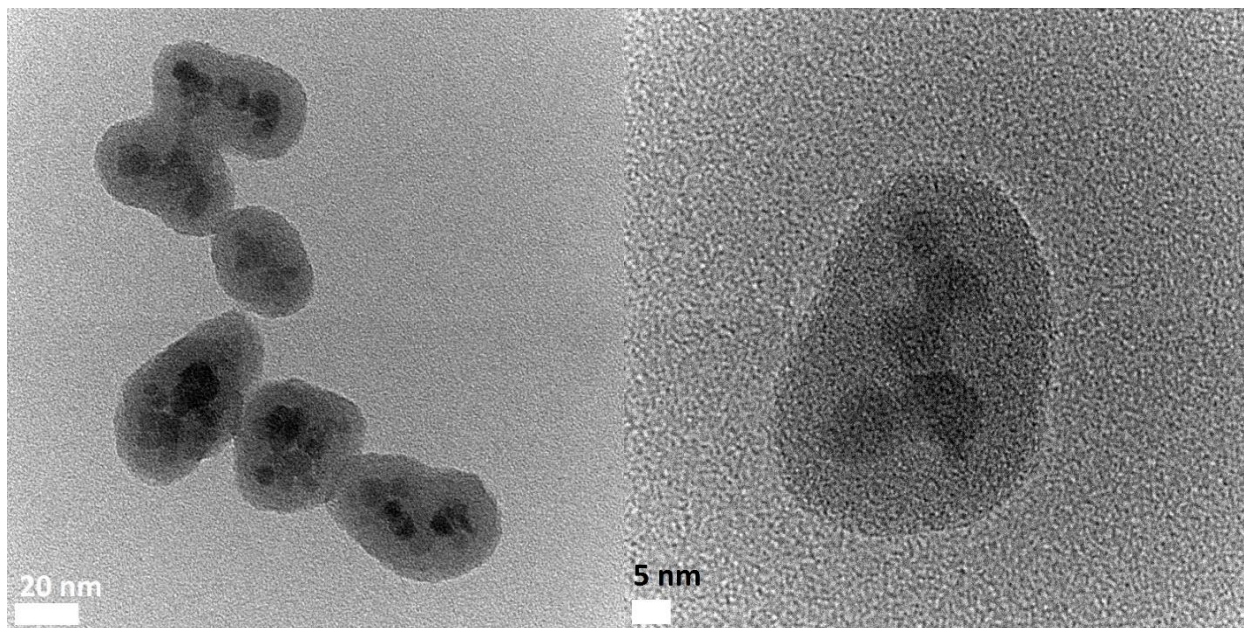


The reaction is a sol-gel process wherein a tetraethylorthosilicate (TEOS) molecule is hydrolyzed in a water-ethanol mixture to produce reactive intermediates which further react with each other to form stable spherical nanoparticles with a narrow size distribution (*Fig. 6*). This procedure could be adapted to coat magnetic nanoparticles with uniform silica shell by dispersing magnetic nanoparticles in an ethanol-water mixture. Ammonium hydroxide is added to stabilize the magnetic particles. TEOS is added dropwise to secure the polycondensation reaction specifically at the surface of magnetic nanoparticles to generate a uniform silica shell. (*Fig. 7*). Silica encapsulation ensures preservation of the magnetic particles from interaction with ingredients of aqueous dispersions.

The encapsulation with a silica shell was adapted for many types of nanoparticles, quantum dots, dyes and fluorescent molecules<sup>60-62</sup>. Binding to or embedding into the silica shell of functional



***Figure 2.7. Transmission electron microscopy of silica coated magnetic nanoparticles***



***Figure 2.8. Transmission electron microscopy of silica coated magnetic nanoparticles***

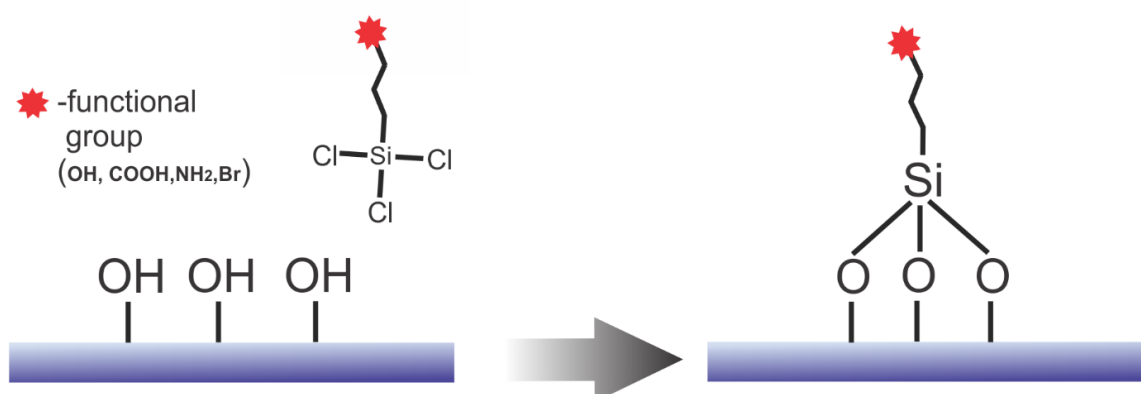
molecules or fine particles could be used to amplify magnetic or optical properties of the nanoparticles<sup>63,64</sup>.

To improve magnetic properties of composite nanoparticles, multiple magnetite cores could be embedded in the silica shell. The latter is achieved at increased nanoparticles concentration and sonication or reaction mixture. Initially formed nanoparticles have irregular shape (Fig. 8) due to the formation of polydisperse particle aggregates from multiple nanoparticles aggregates.

Spherical shape nanoparticles are formed after loading of an additional amount of TEOS and stirring of the reaction mixture for 48 hours. The dispersion is destabilized by adding of hydrochloric acid. The particles are separated by a magnet. After rinsing of the particles using centrifugation-dispersing cycles, they form stable aqueous dispersions that could be used for further functionalization.

### *Silane Stabilization of Magnetic Nanoparticles*

Silane chemistry is a commonly used method of covalent modification of silica coated nanoparticles with a variety of functional groups. Carboxylic, halogen, hydroxide, amino and fluorescent groups are routinely introduced via silica shell reactions with functional silanes (Fig. 2.9).



**Figure 2.9.** General schematics of silane chemistry

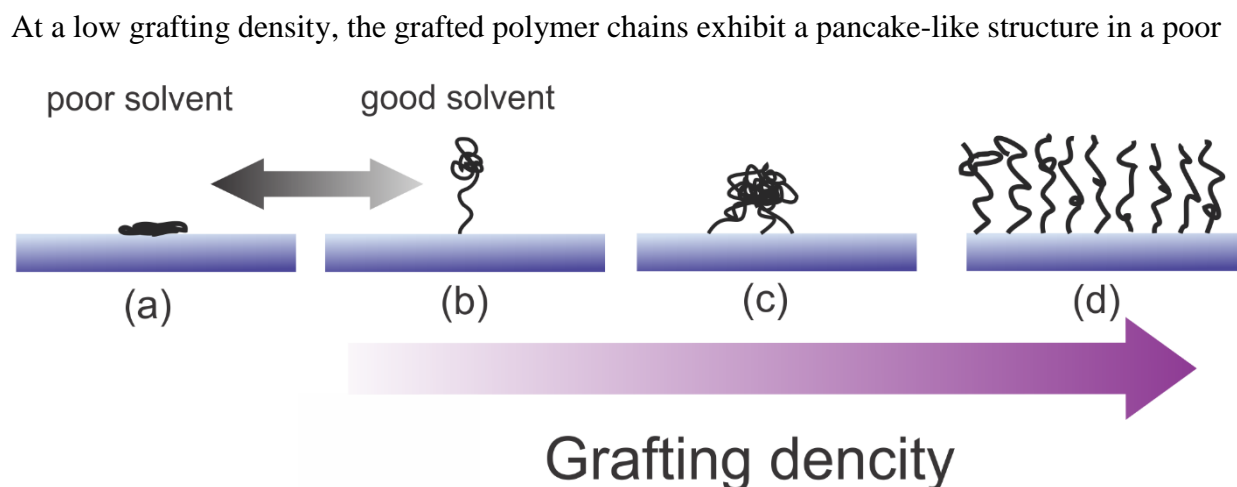
## CHAPTER 3

### POLYMER MODIFICATION

#### 3.1 Thin polymer films.

Functionalizing of material's surface with ultrathin polymer layer is a versatile tool for the surface modification with precisely controlled and adjusted physical and chemical properties<sup>65</sup>.

Composition and properties of the surface interfacial layer plays a critical role for many applications of nanoparticles<sup>66</sup>. Surface functionalization of nanoparticles is used to control colloidal stability, adhesion, rheology and interaction with biomolecules<sup>54,67</sup>. Covalent modification of the nanoparticles surface with tethered polymer chains ensures stability of grafted layers and the structure of the thin film coating. For polymer molecules bound to the surface of nanoparticles, there are different structural regimes that depend on the grafting density of the grafted polymer chains and the interaction of the grafted polymer with solvent. (Fig.3.1).



**Figure 3.1.** Polymer chains at different grafting density and solvent conditions. (a)-pancake regime, (b)-mushroom regime, (c)-chains interaction, (d)-brush

solvent (a), or mushroom- like structure in a good solvent. When grafting density is increased, the chains begin to interact with each other and form aggregates (micelles) in a poor solvent (c) or slightly stretch away from the surface in a good solvent. Further increase of grafting density results in transition of the thin film structure into the polymer brush regime (d) when the grafted chains are strongly stretched from the surface due to the excluded volume effect.

This stretching results in a deformation of the polymer coil, thus in reduction of the entropy of the chains. The polymer film possesses a new equilibrium state with the higher energy when the chains are stretched away perpendicular to the surface. Polymer brush transition occurs when the size of the grafting chains approaches the distance between grafting points, so the following conditions are met:

$$h > \langle r^2 \rangle^{1/2}, \quad d \ll \langle r^2 \rangle^{1/2}$$

Where  $h$  is the polymer brush height,  $\langle r^2 \rangle^{1/2}$  is the end to end distance for the same non-grafted chains, dissolved in the same solvent.

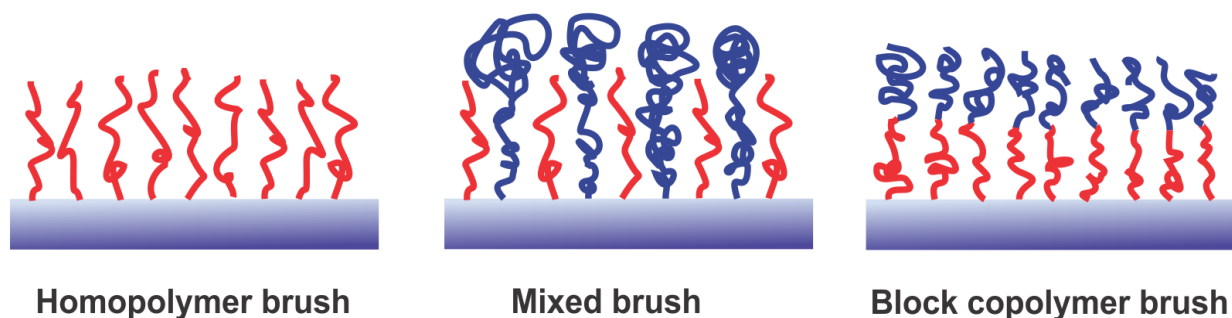
System could be characterized by introducing the parameter for this transition, ( $\Sigma$ ):

$$\Sigma = \sigma * \pi * R_g^2$$

Where  $R_g$  is radius of gyration of tethered chain,  $\sigma = (h\rho N_A)/M_n$ ,  $h$  is brush thickness,  $\rho$  is a bulk density of the brush and  $N_A$  is Avogadro's number. When  $\Sigma < 1$  the system described with a mushroom regime with a weak interchain interactions,  $\Sigma \approx 1$  is a transition conformation and  $\Sigma > 1$  is highly stretched regime. In real systems, no sharp transition between the mushroom and brush regimes is observed because of random distribution of the grafting points and polydispersity of the polymer.

### 3.2 Synthesis of polymer brushes

Polymer brushes could be made of homopolymers (a homopolymer brush) or many polymers (a multicomponent brush) (Fig. 2). Multicomponent brushes attracted significant interest since they offer vast possibilities for preparation of functional interfaces with tunable and stimuli-responsive properties<sup>68-70</sup>. Phase behavior of multicomponent brushes depend on the polymer-polymer and polymer-solvent interactions. The brush properties are dictated by the thin film structure<sup>71</sup>. Multicomponent brushes could be prepared from two or more incompatible polymers by grafting two polymers to the same surface (a mixed brush) or by grafting of block-copolymers (a block copolymer brush).

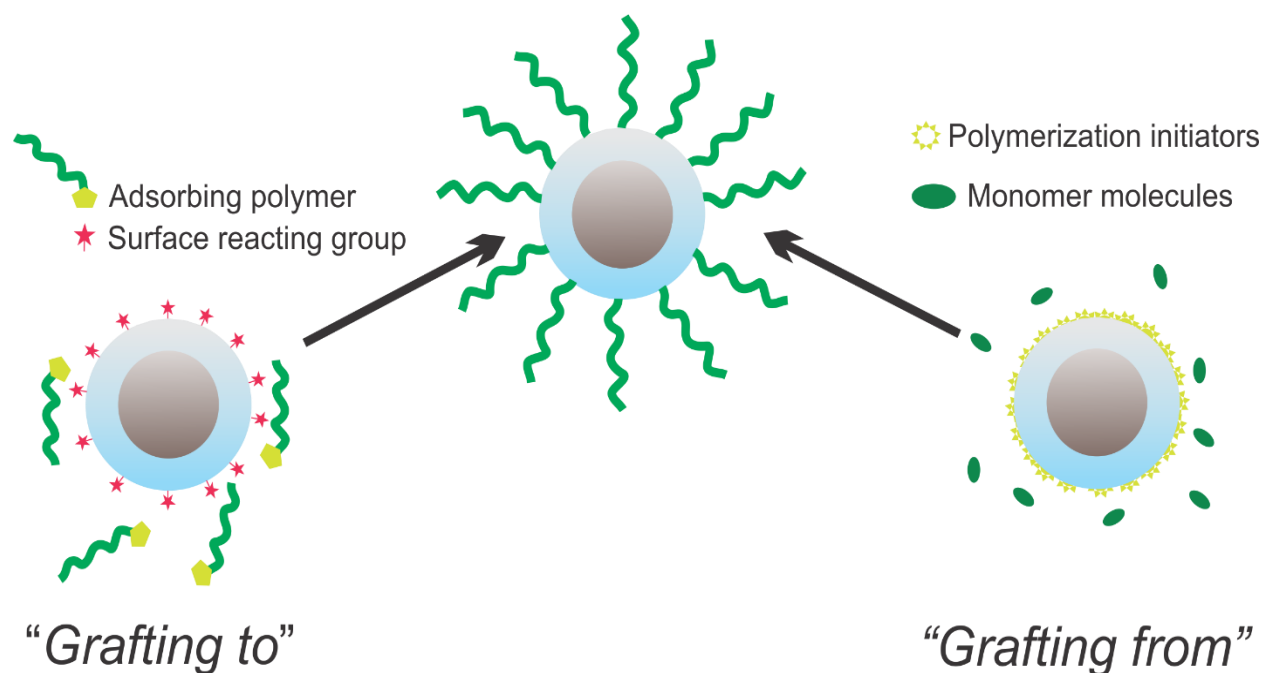


**Figure 3.2.** Schematic illustration of possible morphologies of polymer brushes: *a- homopolymer brush, b-mixed brush and c- block-copolymer brush.*

For example, multicomponent polymer brushes demonstrated switching behavior in their changeable environment (temperature, solvent, pH, etc.) when the brush properties were changed from hydrophobic to hydrophilic<sup>72</sup>, conductive to nonconductive<sup>73</sup>, adhesive-to nonadhesive<sup>74</sup> or adsorbing/nonadsorbing of target molecules<sup>75</sup>.

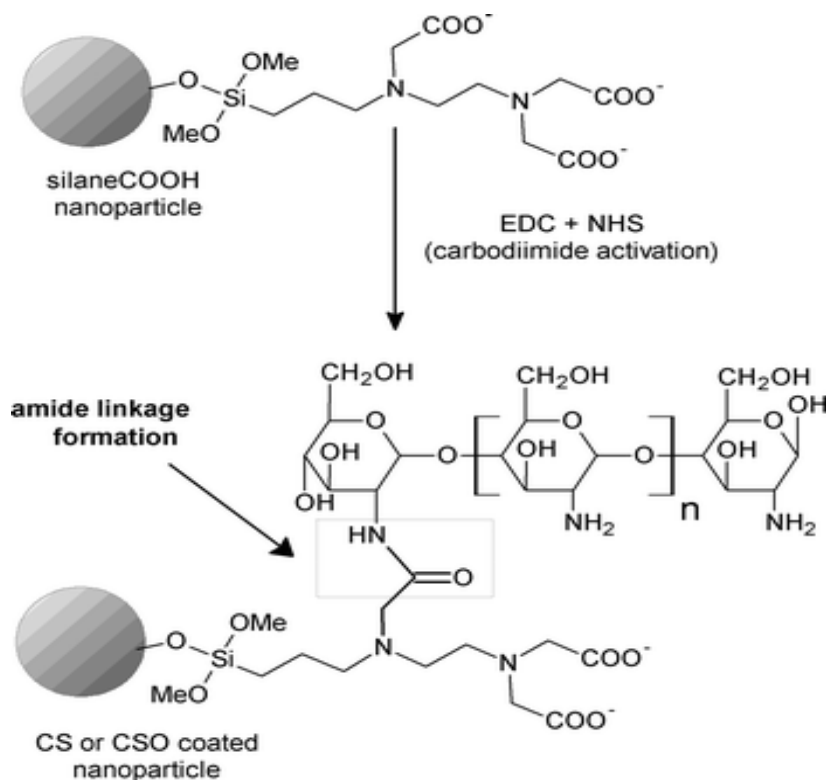
There are two major approaches to introduce polymer brush onto the solid surface (Fig. 3). The first method is termed “*Grafting to*” and it involves reactions of functional groups carried by the polymer molecules (typically end-functional groups) and the complimentary functional groups

on the surface-modified nanoparticles<sup>76</sup> (Fig. 3 left). For example, silica coated magnetic nanoparticles were functionalized by a chitosan polysaccharide to improve biocompatibility<sup>77</sup>(Fig. 4).



**Figure 3.3.** Schematics of “grafting to” and “grafting from” approaches to functionalize silica-coated magnetic nanoparticles.

To introduce a reactive layer on the nanoparticles surface, silica coated particles were functionalized with carboxyl terminated silane<sup>78</sup>. Then, carboxylic groups were activated with EDC-NHS click chemistry and reacted with solution of chitosan resulting in uniformly coated particles. Grafting to method is widely used by many scientists due to its simplicity and ability to use “click chemistry” methods. Prior to the grafting, the polymers could be extensively characterized by various analytical methods. The well characterized polymers with narrow molecular weight distribution form well-defined uniform grafted layers. The reaction could be performed in solutions or in polymer melts. Despite all the benefits, the method has its



**Figure 3.4.** Amide linkage formation between the carboxylic group on the particle surface and the amino group. (With permission from *J. Mater. Chem.*, 2009, 19, 6870-6876)

limitations such as a low grafting density of the brush because of the diffusion limitation of the grafting to reaction.

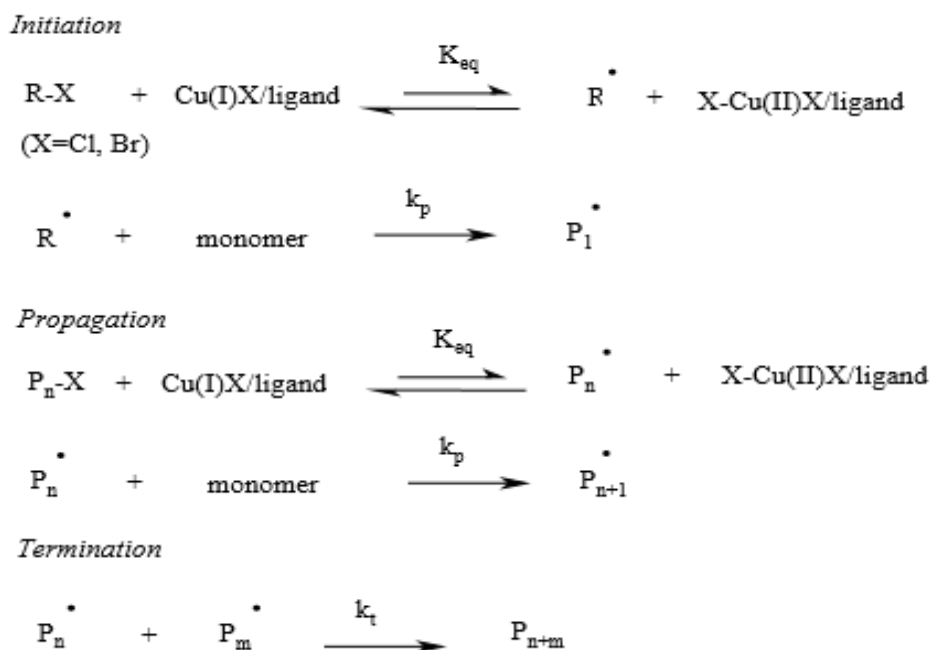
Grafting from melt helps to minimize the excluded volume interactions and results in the grafting of denser brushes.

*Grafting from* method (Fig. 3 right) is based on the synthesis of a covalently grafted polymer layer grown *in situ* from the surface attached initiator<sup>79</sup>. Grafting from methods was developed based on various polymerization mechanisms including radical polymerization<sup>80,81</sup>, anionic polymerization, and atom transfer radical polymerization (ATRP).



ATRP is a frequently used polymerization mechanism to grow high-density polymer brushes with well- controlled molecular weight<sup>82,83</sup>. One of the major advantages of using ATRP for grafting from is the ability to synthesized polymer films with well-controlled thickness. After polymerization, the end groups could remain active or deactivated depending on the following synthetic strategy<sup>84</sup>.

ATRP reaction mechanism is based on maintaining of a low concentration of free radicals in solution and establishment of a fast-dynamic equilibrium between active and dormant species. Reaction consists of two steps, initiation and propagation. In the first step, the organometallic complex abstracts halogen from the alkyl halide, forming an active radical in the reverse redox process. To maintain a low concentration of the reacting species, the deactivation rate must be higher than the activation rate. In other words, the equilibrium is shifted towards the dormant species, otherwise the reaction becomes uncontrolled. The reaction rate is also dependent on the redox potential of metal complexes. The termination reaction is typically very slow.



**Figure 3.5.** The mechanism of ATRP

The molecular mass of the grafted polymer is controlled in two ways. First, the length of the grafted chain depends on the concentration of the reactants and the polymerization time. Secondly, a sacrificial initiator is added to the reaction solution, forming a fraction of the non-attached bulk polymer that could be analyzed to estimate molecular mass of the grafted polymer assuming that the reaction kinetics in solution is the same as for the surface-growing brush. The amount of the added initiator affects the degree of polymerization of the grafted polymer.

A number of monomers have been successfully polymerized using the ATRP polymerization mechanism including acrylamides<sup>85</sup>, acrylates<sup>86</sup>, methacrylates<sup>87,88</sup>, monomers with hydroxide<sup>86</sup>, epoxide and other functional groups. In particular, polyelectrolyte brushes (PEB) attracted interest due to their biocompatibility and similarity to many biological molecules<sup>89-91</sup>. PEB carries ionizable functional groups. In PEB, counter ions are trapped in the brush. The brush thickness is determined by the balance between osmotic pressure of the trapped counter ions and stretching entropy of the chains. The contribution of excluded volume will dominate at high densities, while at moderate density electrostatic interactions (repulsive interactions between similarly charged chains) affect the brush properties. If brush carries a strong base or strong acid ionizable functional groups, the brush properties are not affected by pH or salts (unless the ionic strength of solution approaches the ionic strength in the brush). The behavior of PEB is different for polyelectrolytes that carry weak acid or base functional groups. In this case, polyelectrolytes respond to changes in pH and ionic strength<sup>92,93</sup>. Weak PEB carrying amino-functional groups (for example, polyvinyl pyridine) expands upon a decrease of pH, while acidic PEB (for example, polyacrylic acid) expands upon pH increase. Overall, polymer brushes are extensively studied and used as a building block for biointerfaces in biotechnology, drug delivery and stimuli-responsive coatings.

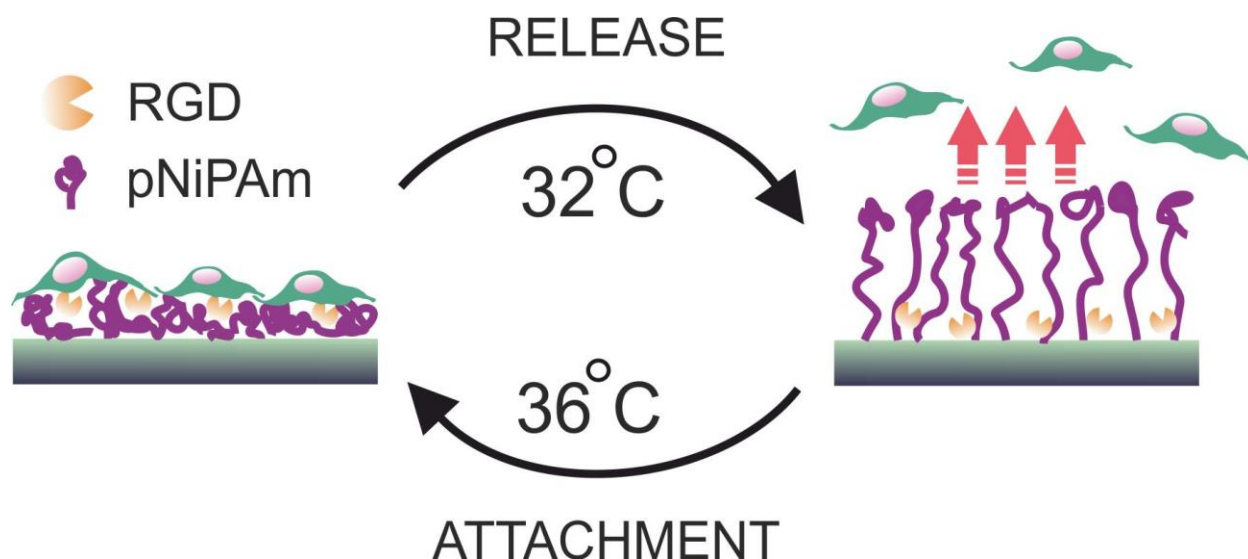
## CHAPTER 4

### BIOMEDICAL APPLICATIONS

Polymer brushes offer great flexibility to modify surfaces with molecular structures for adding new functionalities and tuning surface properties. Recently, there was a significant number of studies published on applications of polymer brushes in biomedical, biomaterial and drug delivery applications.

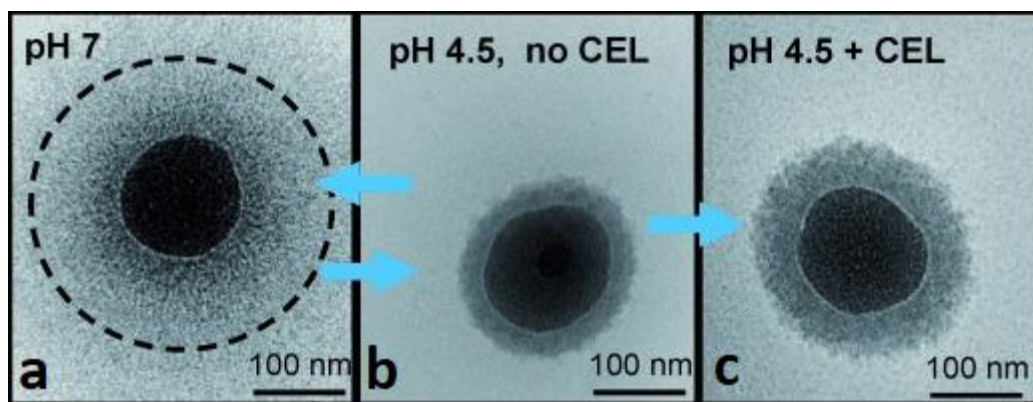
When a synthetic material is introduced into the body, it faces immediate non-specific adsorption of biomolecules, followed by the response from the immune system which typically leads to inflammation. Another concern is contaminations of synthetic materials with microorganisms. Bacterial biofilms formation is the major problem of implant applications leading to post-surgery complications due to inflammation and implant rejection. Antimicrobial coatings carrying antibiotic molecules often are not highly efficient, since the accumulation of dead bacteria promotes formation of biofilms. Polymer brush-based antimicrobial coatings have shown promising results to create bacteria-repelling films with stimuli-responsive properties such as antibiotic release upon local pH change during bacterial attachment<sup>94</sup>. For example, this could be achieved by coating of the surface with polyacrylic acid (PAA)-chitosan block copolymer brush<sup>95</sup>. When system is exposed to physiological media with pH 7.4, PAA polyelectrolyte layer expands forming a barrier film. Adsorption of bacteria results in a drop of pH at the interface due to carbohydrates fermentation and accumulation of organic acid. The latter causes shrinking of PAA and exposing chitosan which is known for its antibacterial properties. The exposure of chitosan blocks bacteria spread leading to restoring of pH when PAA returns to the original state.

On the contrary, tissue culture applications require controlled proliferation of mammalian cells on the surface of the supporting (scaffolding) materials. The surface modification is usually done with self-assembled monolayers (SAM) carrying cell-binding peptide motifs such as arginine-glycine-aspartic acid (RGD)<sup>96</sup>. The limitation to use this approach is due to the poor control of nonspecific cell-protein interaction which leads to non-specific adsorption and contaminations. Another barrier is mechanical properties of SAM layers that have a relatively short and stiff molecular structure as compared to cells natural environment. In natural conditions, cells proliferate in three dimensions upon interaction with other cells and scaffolding molecular aggregates. Grafting of polymer brush with the attached RGD sequence proved to be an excellent solution to mimic cellular environment<sup>97</sup>. Moreover, controlled polymerization methods allow for the regulation of RGD surface density and create specific patterns that target cell adhesion and motion<sup>98</sup>. For application related to tissue regeneration, it is required to grow live cell sheets. Detachable cell sheets were prepared on thermo-responsive polymer brush layers with low critical solution temperature (LCST). The most widely studied example is poly(N-isopropylacrylamide) (PNiPAm) with LCST phase transition in water at 32 °C (Fig. 1). The cells could be seeded and incubated on the pNIPAM layers decorated with RGD at 36 °C followed by the detachment of the grown cell sheets by decreasing temperature to 32 °C<sup>99,100</sup>.



**Figure 4.1.** Schematic of cells interaction with thermo-responsive pNIPAM brush

Enzymes and other proteins could also be adsorbed by polymer brushes. Enzymes applications are steadily increasing in the areas of biotechnology<sup>101,102</sup>, textiles processing<sup>103,104</sup>, pharmaceuticals<sup>105</sup> and other fields of biocatalysis<sup>106</sup>. The widespread use of enzymes is limited by their costs (mainly related to separation and purification). Adsorption of protein molecules on the surface is usually irreversible process. Therefore, most enzymes are used only in single use applications and are not recycled. However, reversible adsorption of many proteins regardless of protein net charge by PAA brushes was observed<sup>90</sup>. Adsorption of proteins depends strongly on pH and salt concentration. At low salt concentrations and at pH below 5 a strong adsorption of proteins by PAA brushes was documented. The adsorption remains unchanged until pH is raised to 6-7; then proteins are released. The proposed mechanism of this process is that adsorption of proteins by poorly charged PAA brush at pH5 leads to release of counter ions from the brush and



**Figure 4.2.** Schematic of the enzymogel nanoparticle. *a) swollen PAA at pH 7 b) shrunk PAA brush at pH 4.5, respectively. c) The brush is uniformly loaded with CEL enzymes at pH 4.5*

positively charged domains of the protein interact with the brush<sup>107,108</sup>. Remarkably, proteins and enzymes adsorption by PAA does not affect protein secondary conformation and its enzymatic activity remains nearly unchanged<sup>109,110</sup>.

Based on these findings, we developed a novel composite material termed “enzymogel” for remote-controlled phase-boundary biocatalysis of cellulose biomass with the ability to recover and reuse catalytically active Cellulase enzymes<sup>111</sup>. Enzymogel demonstrated remotely directed binding to and engulfing insoluble substrates, high mobility, and stability of cellulases. The enzymogel nanoparticles are made of a superparamagnetic core with a silica shell, coated by PAA polymer brush via grafting from approach. Enzymogel was used to hydrolyze cellulose by adsorbing Cellulase enzymes. The loading of the enzymes was conducted from the solution at pH 4.5 (Fig. 2) and releasing them into the bioreactor at pH 7 owing to the stimuli-responsive behavior of the enzymogel brush. The encapsulated Cellulase retains its biocatalytic activity in the brush and after the release of the enzyme to the buffer. After bioconversion of the cellulosic biomass, the enzymogel nanoparticles can be magnetically extracted and transferred into a freshly loaded bioreactor for reuse. The experiments demonstrated that this methodology

provides an about four-fold increase in glucose per enzyme when compared with the traditional single use of cellulases for cellulose conversion.

Drug delivery applications often face challenges of delivery of highly toxic or poorly soluble drugs to the affected tissues. Extensive research has been undertaken in the areas of controlled drug delivery applications using liposomes<sup>112,113</sup>, nanoparticles<sup>2</sup>, control release interfaces and hydrogels<sup>114</sup>. Liposomes (phospholipid bilayer vesicles) has shown promising potential as drug delivery vehicles in cell culture, however their clinical use faced problems associated with their stability. To improve liposome stability and enhance their circulation time in the blood, sterical stabilization mechanism are often used. For example, introduction of a PEG shell is a commonly used approach<sup>115</sup>. Nanoparticles, on contrary, offer significant advantages over liposomes owing to their mechanical stability, precise size control and ability to functionalize with high density polymer brushes. For anti-cancer therapy, nanoparticles of less than 100 nm are used since they demonstrated prolonged blood circulation time and passive capturing by a tumorous tissue. Tumor tissues are characterized by an overdeveloped microvasculature system that captures nanoparticles as a result of the enhanced permeability and retention (EPR) phenomenon, first described by Maeda and Matsumura<sup>116,117</sup>. This phenomenon is actively used for magnetic nanoparticles tumor therapy by hyperthermia<sup>118</sup>, imaging by MRI contrast<sup>119</sup>, and photoacoustic imaging<sup>120</sup>. Modification of nanoparticles by polymer brushes allows to increase their plasma half-life from a few minutes up to several days due to “stealth effect”<sup>121,122</sup>. Various ligands could also be grafted to the polymer chains, allowing the targeted delivery. The most advanced delivery systems combine multifunctional properties; for example, magnetically targeted delivery, targeting and release. Majority of these systems consist of magnetic nanoparticles associated with thermo-responsive materials that hold cargo molecule by adsorption or physical

entrapment<sup>123-125</sup>. Many tumorous tissues have acidic environment, so pH mediated systems were also widely reported<sup>126-128</sup>.

In summary: the possibility to tailor of psychochemical properties of nanostructured materials by modifying with polymer brushes opened a new phase of pharmaceutical and biotechnological applications. Nanomaterials approaches for enzyme delivery are actively employed in industrial processes improving biofuel production efficiency, lowering the processing costs and promoting sustainability.

Emerging novel biomaterials based on multifunctional nanoparticles are currently involved in numerous trials for the chemotherapy, immunotherapy, and drug delivery showing promising safety results. Translation research will lead to rise of less toxic, safer and affordable treatments and improve quality of life.



## CHAPTER 5

### MAGNETIC FIELD REMOTELY CONTROLLED HIGHLY-SELECTIVE BIOCATALYSIS

**Andrey Zakharchenko<sup>1</sup>, Nataliia Guz<sup>2</sup>, Amine Mohamed Laradji<sup>1</sup>, Evgeny Katz<sup>2</sup> and  
Sergiy Minko<sup>1\*</sup>**

Many applications for medical therapy, biotechnology and biosensors rely on efficient delivery and release of active substances. Here, we demonstrate a platform that explores magnetic-field-responsive compartmentalization of biocatalytic reactions for well-controlled release of chemicals or biological materials on demand. This platform combines two different kinds of core-shell magnetic nanoparticle: one loaded with enzymes and another with substrate-bound therapeutic (bio)chemicals. Both cargos are shielded with a polymer brush structure of the nanoparticle shell, which prevents any enzyme-substrate interactions. The shield's barrier is overcome when a relatively weak (a fraction of 1 T) external magnetic field is applied and the enzyme and the substrate are merged and forced to interact in the generated nanocompartment. The merged biocatalytic nanoparticles liberate the substrate-bound therapeutic drugs when the enzymes degrade the substrate. The developed platform provides a proof of concept for the remotely controlled release of drugs or (bio)chemicals using the energy of a non-invasive, weak magnetic field.

<sup>1</sup>Nanostructured Materials Lab, University of Georgia, Athens, GA, USA. <sup>2</sup>Department of Chemistry and Biomolecular Science, Clarkson University, Potsdam, NY, USA.

Accepted by Nature Catalysis. Reprinted here with permission of publisher, (Apr. 10, 2018)

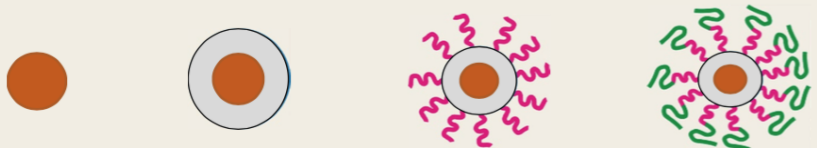
Materials that efficiently release biological molecules or therapeutic chemicals on demand using exposure to remotely controlled and safe external sources of energy, such as magnetic fields, could find applications for drug delivery<sup>130</sup>, biotechnology<sup>131,132</sup> and biosensors<sup>133</sup>. Because live tissue and synthetic polymers are not responsive to weak magnetic fields, the development of magnetic-field-responsive soft materials has been reported by combining magnetic nanoparticles and stimuli-responsive soft materials<sup>134</sup>. Magnetic nanoparticles interact with magnetic fields and transduce magnetic field energy into physical or chemical changes in the soft material. Materials that control enzymatic processes are one example of such soft materials. Enzymes are extensively used to change or degrade colloidal particles, capsules, and their assemblies to trigger release of the cargo via biocatalytic reactions<sup>135,136</sup>.

In all eukaryotes, metabolic pathways are precisely organized and regulated. This precise control is based in part on the high selectivity of biocatalytic reactions and controlled transport of chemicals and biomacromolecules across membranes that compartmentalize cells, organelles and organs. Highly selective biocatalysis alone cannot orchestrate complex systems of biochemical reactions without the supporting role of signal-triggered synthesis, release, secretion, conversion and degrading processes that take place in different compartments in cells and organs. Despite being highly selective, enzymes cannot provide 100% selectivity. In particular, enzymes could interact with a number of substrates of a similar chemical structure (for example, proteases are highly promiscuous catalysts), be degraded by other enzymes or even by self-digestion upon secretion into a complex biological environment, or undergo undesired aggregation, crystallization or nonspecific adsorption, which would strongly damage the efficiency of the biocatalytic process. However, the overall high specificity of biocatalytic processes is strengthened by localizing the enzymatic reactions within a specific environment and spatial

compartments. Inspired by this hierarchical design in live systems, diverse stimuli-responsive functional materials have been reported, involving various architectures that respond to changes in magnetic fields<sup>137–139</sup>. However, it remains challenging to create a reactive system that preserves enzyme molecules from destructive environments and undesired interactions while being able to initiate the designated reaction when needed. Different approaches have been developed to preserve enzymes for storage and delivery before activating them on demand in a magnetic field at the targeted location. A number of studies aimed at controlling the kinetics of biocatalytic reactions in model systems<sup>140–144</sup> have explored magnetic-field-triggered changes of the local concentration and mobility of enzymes. However, it is difficult to apply many of such approaches to live tissue because of limitations associated with degradation of many biological molecules in complex biological milieu, toxicity of the materials and a narrow variation range of physiological conditions. The most common approach is to embed magnetic nanoparticles in a thermoresponsive material and expose them to an alternating magnetic field. The local temperature rise due to transformation of electromagnetic energy into heat is used to trigger changes in the thermoresponsive material without a need to elevate the temperature of the entire system<sup>145</sup>. This scenario is not always appropriate for enzymes because of their generally poor thermal stability.

We report here a proof-of-concept study of magnetic-field- controlled biocatalysis, which does not rely on commonly used alterations of local temperature, pH, salt concentration or light absorbance. Our biocatalytic platform uses a biomimetic concept of compartmentalization, magnetic-field-controlled transport and interactions of substrates and biocatalysts across semi-permeable walls of the compartments. In our system, the biocatalytic process is achieved via magnetic-field-triggered interactions when two distinctive nanoparticles—one loaded with an

enzyme (for example, protease) and another with a substrate (for example, polypeptide)—are brought into the merging vicinity of each other. The enzyme and substrate molecules bound to the nanoparticles are framed by semi-permeable barriers with gating properties—polymer brushes—which prevent interactions of both the enzyme and the substrate with other competitive molecules and with each other. This design resembles compartments that accommodate and preserve the substrate and enzyme from interactions ahead of time. The biocatalytic reaction is turned on only in the presence of a magnetic field that triggers merging of the compartments. In addition, the compartments are tailored to provide the most favorable environment for the enzymatic process, for example, an acidic environment favorable for hydrolytic reactions catalyzed by many proteases could be achieved using a weak polyacid brush architecture even if the environment outside the polyacid brush was buffered at pH 7<sup>146</sup>. The method proposed here could be realized by using either uniform or non-uniform magnetic fields generated by a permanent magnet or an electromagnet, with a low strength magnetic field achievable in biological systems with remote magnet positioning.

**Table 1 | Structure and characteristics of the biocatalytic NPs**


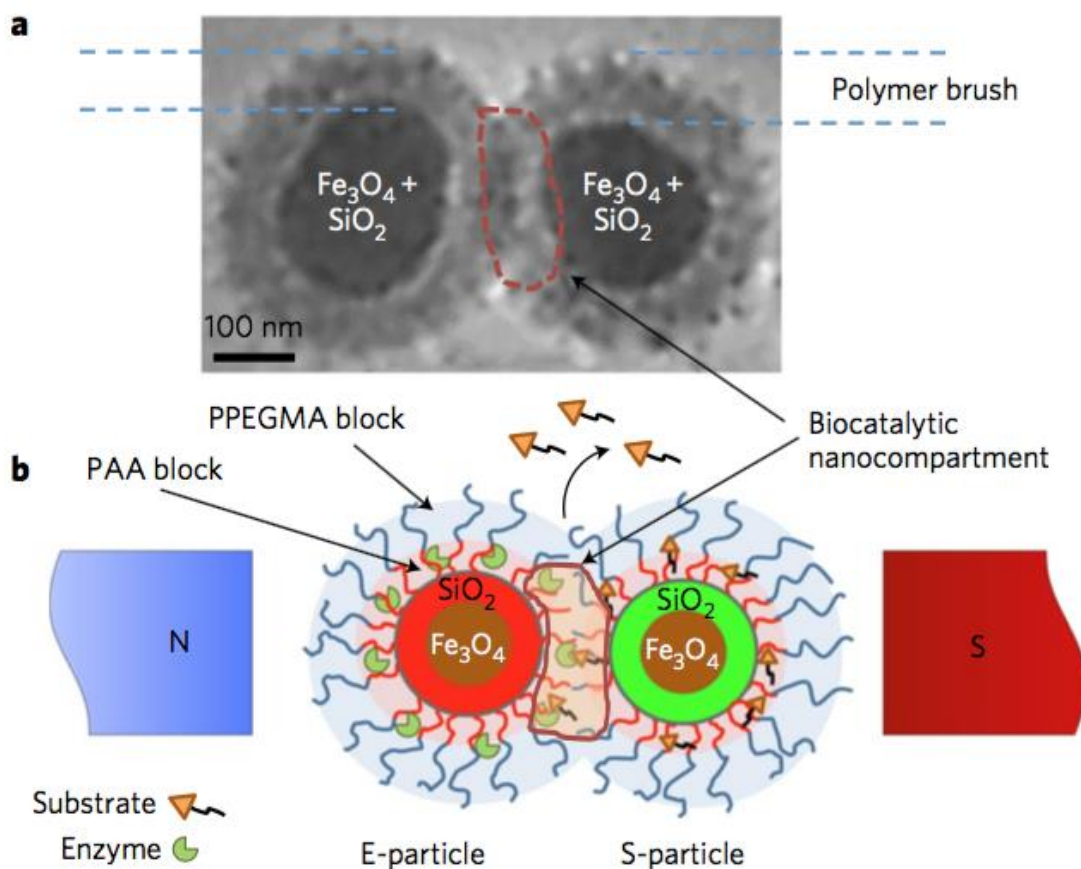
	Iron oxide core	Iron oxide core in silica shell	Core-shell particles with grafted PAA	Core-shell particle with grafted PAA-b-PPEGMA
Diameter at pH 7.5 ( $\pm 5$ nm)	16	50	82	115
$\zeta$ -potential ( $\pm 10$ mv)	-10	-40	-50	-5
Brush thickness swollen/dry ( $\pm 5$ nm)	—	—	16/4.5	32.5/9.3
Number average molecular mass $M_n$ ( $\text{g mol}^{-1}$ , $\pm 5\%$ )	—	—	8,600	17,000
Grafting density ( $\pm 0.06 \text{ nm}^{-2}$ )	—	—	0.36	0.36
Distance between grafting points ( $\pm 0.15$ nm)	—	—	1.9	1.9
Loading with FD-BSA ( $\text{mol g}^{-1}$ )	—	—	—	$4.1 \pm 0.2 \times 10^{-6}$
Loading with papain ( $\text{mol g}^{-1}$ )	—	—	—	$15 \pm 0.8 \times 10^{-6}$
Loading with DOX ( $\text{mol g}^{-1}$ )	—	—	—	$141 \pm 6 \times 10^{-6}$

Methods of characterizations and calculations are explained in the Supplementary Information.

**Table 1. Structure and characteristics of biocatalytic NP**

## Results

**5.1 Design of biocatalytic nanoparticles.** Here, we demonstrate that papain—a highly promiscuous protease—can be utilized in a selective biocatalytic process using our concept of magnetically controlled biocatalysis. According to this concept, we perform covalent conjugation of enzymes and polymer brushes linked to nanoparticles. The conjugation has minimal effect on the chemical structure, conformation and hence the specificity of the enzyme. We change only topological aspects of the biocatalytic reaction when we secure interactions of the enzyme with the designated substrate by exploring specific architecture of the compartmentalized system. The concept is realized by using the architecture of a spherical core–shell nanoparticle (NP). The system contains two kinds of NP: E and S, where E-nanoparticles are loaded with the enzyme and S-nanoparticles are loaded with the substrate. The two NPs possess a very similar architecture: a superparamagnetic core is enveloped by a silica shell with a grafted block-copolymer brush.



**Fig.5.1 | E- and S-type superparamagnetic nanoparticles carrying the enzyme and the substrate. a,b, Cryo-transmission electron microscopy (cryo-TEM) image (a) and schematic (b) explaining the concept of the magnetic-field-triggered biocatalysis. The particle superparamagnetic core is made of  $\text{Fe}_3\text{O}_4$  nanoparticles enveloped by silica.**

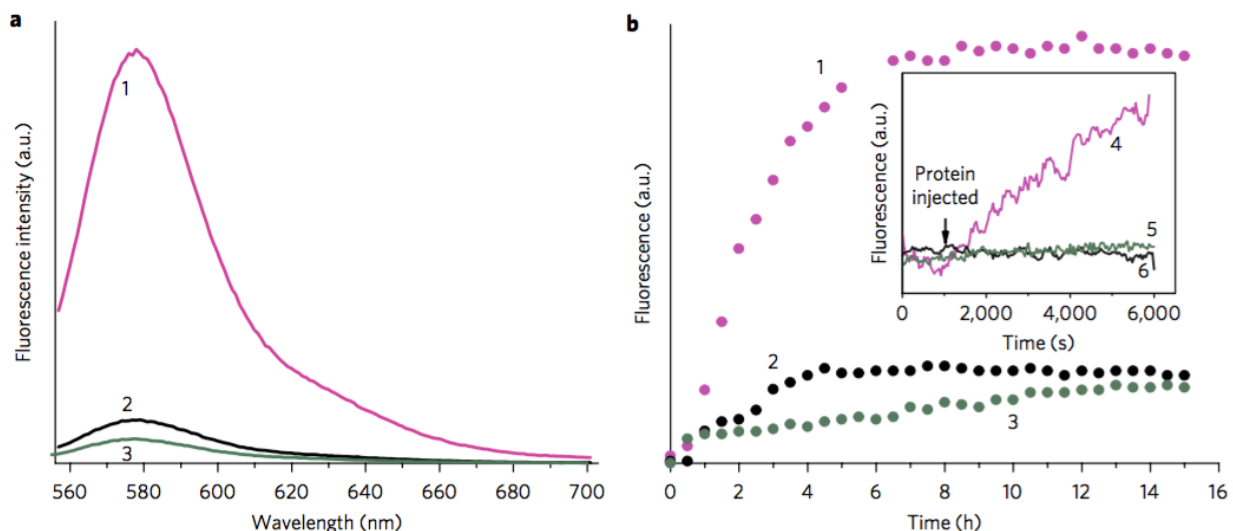
The silica envelope is labelled with covalently bound fluorescent dyes (red for E-particles and green for S-particles). In the magnetic field, due to dipole–dipole interactions, the particles are brought into contact, so that the brush-like double-layer shells merge and intertwine, enabling interactions between the enzyme and substrate. The inner layers of the brush-shell are made of polyacrylic acid (PAA), which carries conjugated molecules of enzymes and substrates and provides the acidic environment for hydrolytic reactions. The external shell of poly(ethylene glycol methyl ether acrylate) polymer (PPEGMA) secures a barrier function to block ‘unauthorized’ or premature reactions of the enzyme and the substrate. The biocatalytic reaction is localized within the biocatalytic nanocompartment, which is generated in the magnetic field. The reaction is monitored by detecting the released cargo molecules.

The grafted block is polyacrylic acid (PAA) and the external block is a polymer of poly(ethylene glycol methyl ether acrylate) macromer (PPEGMA) with an average number of ethylene glycol monomeric units per macromer of 9.3. The molecular mass of PAA-b-PPEGMA block copolymer is  $17\text{ kg mol}^{-1}$  where the PAA and PPEGMA blocks are  $8.5\text{ kg mol}^{-1}$  each.

Carbodiimide conjugation chemistry was used to covalently bind papain and the substrate—fluorescent dye (FD)-labelled bovine serum albumin (FD-BSA)—to the E- and S-nanoparticles, respectively. A cryo-transmission electron microscopy (cryo-TEM) image of a two-particle aggregate comprising E- and S-nanoparticles and a schematic of the concept are presented in Fig. 1. The nanoparticle characteristics are listed in Table 1 and Tables 1 and 2. NPs carry 20% wt of PAA-b-PPEGMA and about 30% wt of proteins. The details of characterization can be found in Methods and Experimental Details.

The architecture described above enables the magnetic-field- triggered proteolysis of FD-BSA, which results in the liberation and release of FD. The latter can be detected using fluorescence spectrometry (Fig. 2). Indeed, FD release took place immediately after the magnetic field was turned on in contrast to the reference experiments when a blend of E- and S-nanoparticles experienced no magnetic field. Both E- and S-nanoparticles are mixed and coexist in the same container as a stable aqueous dispersion with no interactions if the magnetic field is off (Fig. 2b).

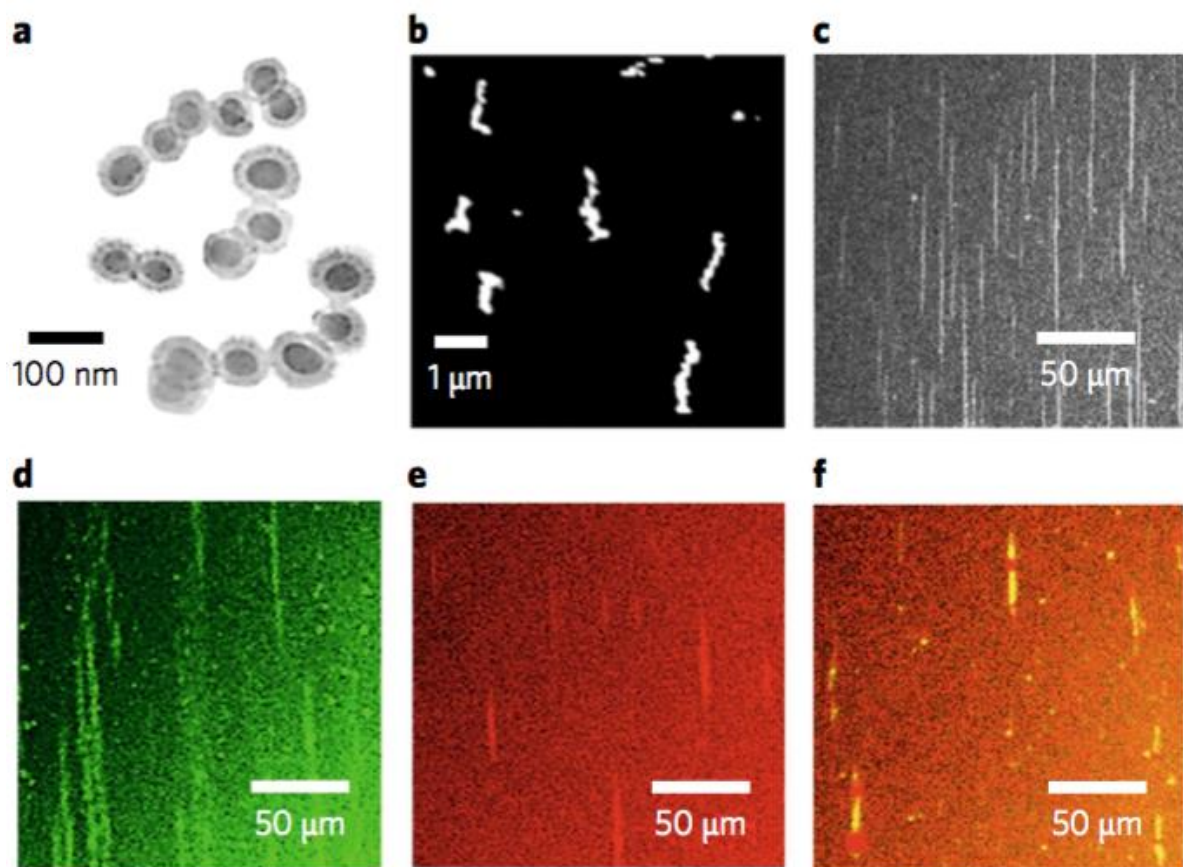
The fluorometric data suggest that high selectivity of the magnetically triggered biocatalytic reaction is achieved owing to the NPs' unique architecture. The zero-field control experiments demonstrate that E- and S-nanoparticles do not interact in the aqueous suspension. Papain proteolytic behavior is not specific to BSA. At the same time, FD-BSA is a substrate that is not specific to papain. FD-BSA could be degraded by other proteases while papain could degrade



**Fig. 5.2 | Monitoring of the magnetic-field-triggered release of fluorescein dye.** Fluorescent dye (FD) is released from a mixture of *E*- and *S*-nanoparticles in phosphate-buffered saline (PBS, pH 7.4). **a**, Emission spectra of FD in solution: 16 h after the magnetic field is turned on (line 1), and the reference experiments, 16 h after the nanoparticle mixing with no magnetic field (line 2) and the spectrum acquired immediately after mixing of the NPs with no magnetic field (line 3). **b**, Kinetics of FD release: triggered by magnetic field (line 1), and reference experiments, *E*- and *S*-nanoparticle mixture with no magnetic field (line 2) and only *S*-nanoparticles in a PBS solution (line 3). The graphs are representative data of multiple repetitions of the experiments (three or more repetitions). The inset shows the reference experiments with no magnetic field when FD-labelled bovine serum albumin (FD-BSA) is mixed with papain in a buffered solution (line 4), FD-BSA is mixed with *E*-nanoparticles (line 5) and papain is mixed with *S*-nanoparticles (line 6). All reference experiments are negative. The ‘authorized’ release of the cargo is possible only in the case when both *E*- and *S*-nanoparticles are present and the magnetic field is on.

various proteins. Thus, in complex biological systems that contain various proteins, the reaction between papain and FD-BSA is not selective and not controlled. This reaction is one of many parallel and competitive reactions catalyzed by different proteases, and it begins immediately upon mixing the ingredients. However, the specially crafted structure of *E*- and *S*-nanoparticles was used here to convert non-selective proteolysis into a selective reaction that rejects all other proteins and turns off the self-digestion of the proteolytic enzyme. Thus, this architecture





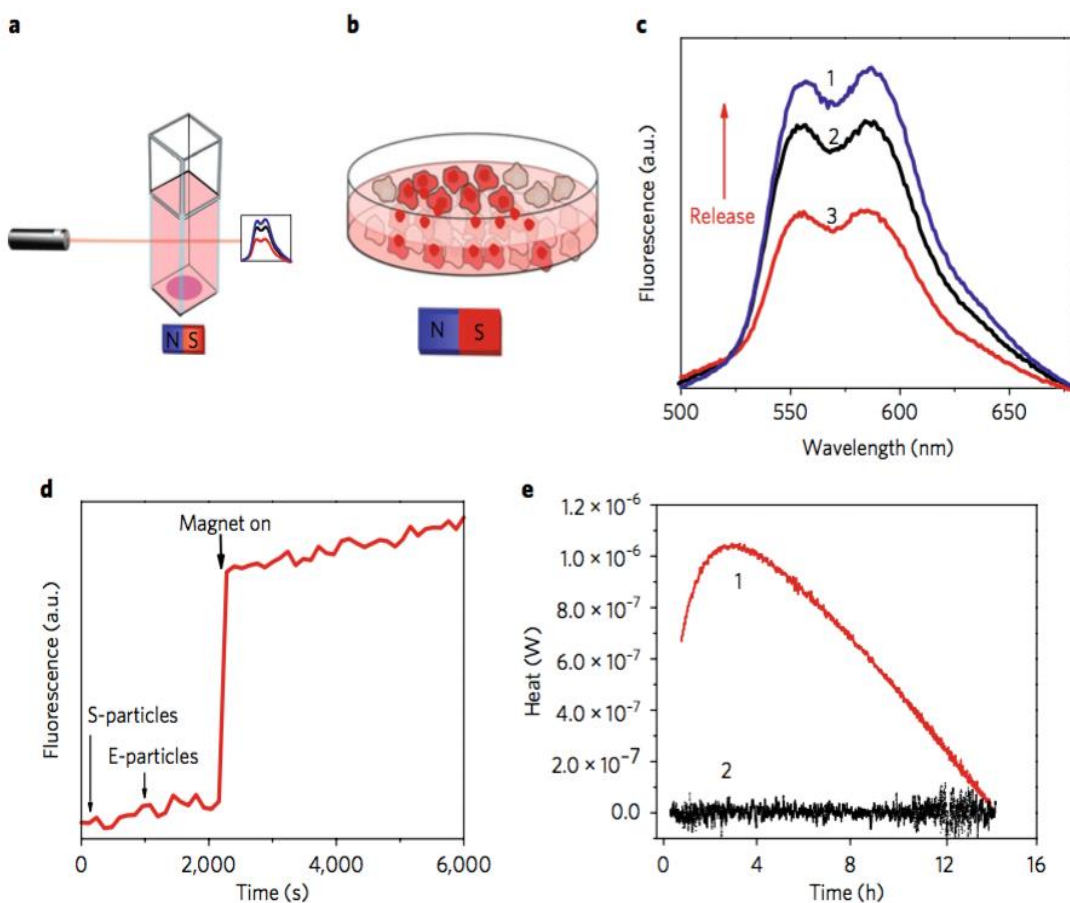
**Fig. 5.3 | Chains of biocatalytic nanoparticles.** *a–f*, The chains of the nanoparticles (NPs) are formed in magnetic field at low (0.01%, **a,b**) and high (1%, **c–f**) NP concentrations. **a,b**, Cryo-TEM (**a**) and atomic force microscopy (**b**) images of small aggregates deposited on the Si wafer. **c–e**, Dark-field optical microscopy of string-like aggregates, and aggregates visualized with confocal microscopy (**c**) when formed by green fluorescein-silica-shell-labelled S-nanoparticle chains (**d**) and red rhodamine-B-silica-shell-labelled E-nanoparticle chains (**e**). **f**, Additive yellow colour of the chains owing to randomly mixed green S-nanoparticles and red E-nanoparticles.

excludes ‘unauthorized’ reactions of papain and FD-BSA (Fig. 2b, inset). Importantly, the biocatalytic activity of papain bound to PAA is not compromised, as was shown in reference experiments with the conjugated enzyme (*Experimental details* Figs. 10 and 11 and Table 3). These conclusions were confirmed using gel-electrophoresis to monitor release of degraded

fragments of the BSA conjugates. We observed release of BSA fragments only if a mixture of S- and E-nanoparticles was exposed to the magnetic field. The experiments with zero-field and for mixtures with native enzymes in solution did not reveal essential release of BSA fragments (Experimental data Figs. 13–15).

**5.2 Magnetic-field-controlled biocatalysis.** The brush-like structure of the nanoparticle shell is a key element to achieving control over the biocatalytic reaction and cargo release and to turning the papain–FD-BSA reaction into a selective biocatalytic reaction. Owing to the brush architecture, the enzyme can reach the biocatalytic nanocompartment with the designated substrate only if the magnetic field is turned on, as discussed above.

In a magnetic field, dipole–dipole interactions between super- paramagnetic NPs result in the formation of aggregates that grow and form chain-like structures. The size of the aggregates depends on NP concentration and exposure time to the magnetic field as visualized by cryo-TEM, atomic-force microscopy (AFM) and dark-field optical microscopy (Fig. 3a–c). TEM images of the aggregates are presented in *Experimental Details* Fig. 12. For a 1:1 blend of E- and S-nanoparticles, the probability of finding two different NPs that form an E–S sequence in two-particle aggregates or in the chain is 50%. While the magnetic field is on, the chain structure is growing in length and diameter, eventually consuming all the magnetic NPs in the solution. The probability of finding at least one E–S sequence in each aggregate approaches 1 for large aggregates so that virtually each particle aggregate is involved in the biocatalytic reaction. Chains of dipolar particles are subject to strong Landau–Peierls thermal fluctuations<sup>147–149</sup>.

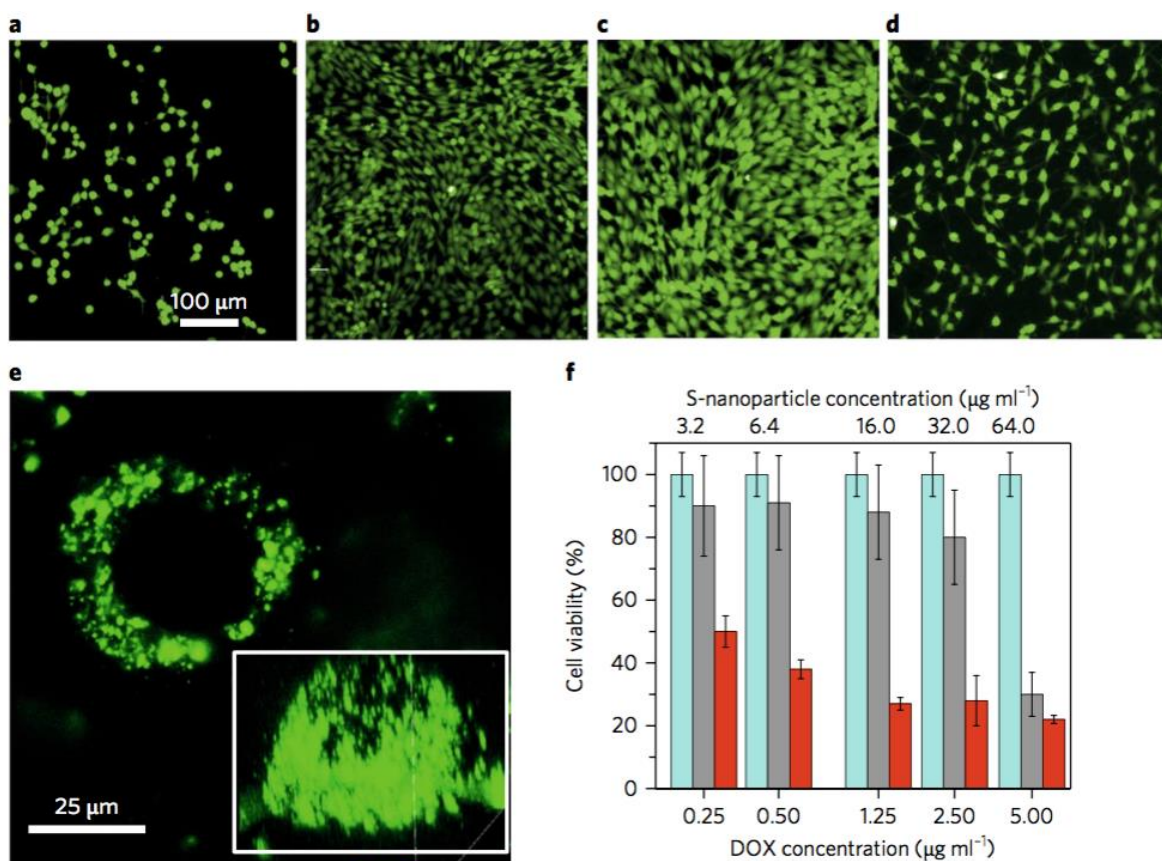


**Fig. 5.4 | Magnetically controlled release of the drug.** **a,b**, Schematics of magnetically controlled release of doxorubicin (DOX) chemotherapy agent in the presence of a permanent magnet with E- and S-nanoparticles loaded in a spectroscopic cuvette (**a**) and a cell culture dish (**b**)—the magnet was placed within 1 cm of the particle dispersion. **c**, Time-dependent change of emission spectra of DOX released in the cuvette after 24 h (line 1), after 1 h (line 2) and immediately after mixing in magnetic field (line 3). **d**, Kinetics of DOX release on loading of the S- and E-nanoparticles and on the placement of the permanent magnet to the bottom of the cuvette. The arrows mark the moments of addition of the S- and E-nanoparticles and the turning on of the magnetic field. **e**, Microcalorimetric monitoring of the DOX release showing thermal activity (line 1) versus the base line (line 2).

Theoretical analysis and experiments revealed that the field-induced aggregation process of dipolar particles is a complex phenomenon and the structure of aggregates depends on the balance of magnetic forces, thermal fluctuations and other interaction mechanisms between NPs. NPs in the aggregates may undergo rearrangements<sup>150–153</sup>. The dynamics of the aggregates facilitates an increased efficiency of biocatalytic reactions in the nanocompartments generated in the aggregates. The mechanism of the mixed chain (made of E- and S-nanoparticles) formation is illustrated in Fig. 3d–f. In this experiment, S- and E-nanoparticles were labelled with fluorescein and rhodamine-B fluorescent dyes, respectively. The dyes were encapsulated in the silica shell of the magnetic core. Both NPs form chain-like structures in the magnetic field visualized with fluorescent microscopy as green and red chains, respectively (Fig. 3d,e). In Fig. 3f, it is clearly seen that the NP blend forms yellow chains originating from the additive colour mixing of green- and red-labelled NPs in the same chain.

Within the magnetic chains, the force of dipole–dipole interactions is proportional to the strength of the magnetic field. The force generated by the magnetic field results in an attraction between the NPs and a compression of the block-copolymer brush. The compressed brush exerts a repulsive interaction between the NPs. An equilibrium compression of the brush will depend on the brush's molecular characteristics, magnetic properties of the NPs and the strength of the magnetic field. The repulsive interaction is proportional to the molecular mass of the polymer brush and grafting density, and is reciprocal to the compressed brush thickness. The dipole–dipole interaction between the NPs is proportional to the strength of the magnetic field, size of the magnetic core and its magnetic susceptibility. Adjustments of these characteristics of the brush, magnetic NPs and magnetic field, loading and saturation of the brush with proteins in combination provide ample opportunities to optimize the biocatalytic system to achieve

magnetic-field-controlled biocatalysis in real-life applications. A quantitative theoretical analysis of this adjustment has been published elsewhere<sup>\*</sup>.



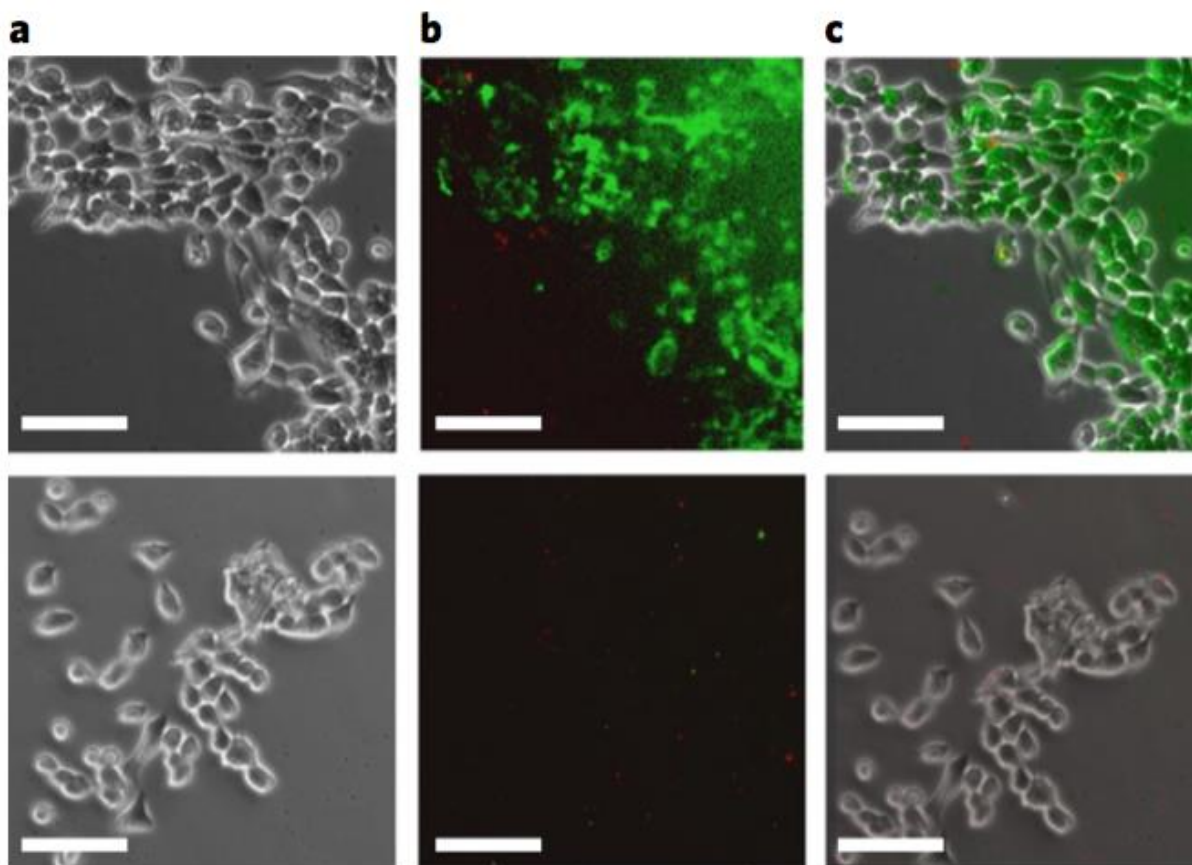
**Fig. 5.5 | Magnetic-field-triggered blocking of cancer cell proliferation.** *a*, 4T1 breast cancer cells were incubated with a 1:1 mixture of S- and E-nanoparticles for 24 h. *b–f*, Then the magnetic field was applied and the culture was examined at 24 h following the magnet attachment: PBS control experiment (*b*); no magnetic field was applied (*c*); and the magnetic field was turned on (*d*). *e*, 2D (main) and 3D (inset) confocal images clearly showed cell uptake of the fluorescein-silica-shell-labelled S-nanoparticles. *f*, Cell counts at different concentrations of S- and E-nanoparticles (1:1 mixture) 12 h after the application of the magnetic field (red bars) versus the experiment with no magnetic field (grey bars) and the control (no NPs added, blue bars); nanoparticle concentrations are shown in terms of E-particle concentration (50% of the overall E- and S-nanoparticle concentration) and in terms of conjugated doxorubicin concentration. The error bars show the standard deviation obtained from three experimental repeats.

**5.3 Magnetic-field-controlled drug release.** One important application of the developed architecture is magnetic-field-controlled drug release. It is commonly recognized that side effects of uncontrolled drug release cause severe intoxication and even death of patients. In general, targeted drug delivery should allow optimal dosages only in disease-affected areas, thus reducing toxic side effects. However, in a specific example of cancer treatment, recent analysis shows that only a small fraction of the administered drug dose is delivered to a solid tumour<sup>155</sup> because of immune system response and organ competition mechanisms that shorten nanoparticle circulation in blood. At the same time, a prolonged circulation could cause premature drug release. The solution to this problem relies on a well-controlled initiation and duration of the drug release in the targeted location. A number of studies have demonstrated great potential of magnetic guidance of drug carriers with improved drug accumulation in solid tumours when the drug accumulation can be monitored using magnetic resonance imaging<sup>139</sup>. In those studies, magnetic guidance was combined with controlled release using heat generation in an oscillating magnetic field. The local temperature at the vicinity of the drug carrier is, however, difficult to control.

The biocatalytic system reported here is a versatile platform enabling the development of well-controlled targeted drug delivery systems. We propose two possible scenarios for drug administration. According to the first scenario, S- and E-nanoparticles are blended and injected. The particles circulate in blood and accumulate in the target tissue via passive or active (if appropriately functionalized<sup>156,157</sup>) targeting mechanisms. Application of magnetic field upon confirmed accumulation of NPs in the target will trigger the drug release. The second possible scenario is a two-step drug administration in which S-nanoparticles are magnetically guided to

the target<sup>158</sup> first. This stage could be conducted as long as needed to accumulate the therapeutic dosage of the drug carried by the S-nanoparticles. A premature release is prevented by the architecture of the S-nanoparticles, as shown in Fig. 2b inset. In the second step, E-nanoparticles are injected and guided to the same target location. The two-step approach avoids E- and S-nanoparticles interacting in blood if a magnetic field is applied prior to NP arrival in the target zone. Upon arrival, the E-nanoparticles merge with already accumulated S-nanoparticles in a magnetic field to release the drug-cargo. The particle accumulation could be confirmed using magnetic resonance imaging technology<sup>159,160</sup>. This concept is demonstrated here using a chemotherapy agent doxorubicin (DOX) loaded in S-nanoparticles via conjugation to BSA (DOX-BSA). Fluorescence spectra, isothermal microcalorimetry and gel-electrophoresis experiments were used to monitor release of DOX from the S-nanoparticles in a buffer solution at pH 7.4. The fluorescent spectroscopy experiment was conducted in a glass cuvette with a magnet attached to the bottom (Fig. 4a). The released DOX diffused into the bulk solution in the cuvette, and the spectra were acquired at different time intervals (Fig. 4c). Initially, the S-nanoparticles with DOX-BSA were loaded in the cuvette. No DOX was detected in the solution after a waiting period, meaning no leakage of the drug in the absence of the magnetic field (Fig. 4d). Note, that the background fluorescent signal originated from the DOX molecules bound to the NPs. Then, the E-nanoparticles were added to the cuvette. No DOX spectra were detected in the mixed dispersion either. However, a burst release of DOX was observed as soon as the magnet was placed in the vicinity of the cuvette (Fig. 4d). Note, the non-zero base line is due to a weak fluorescence of quenched DOX in the conjugate. Upon release, the DOX fluorescent intensity increases and recovers<sup>161</sup> (see Supporting Fig. 7). Quantitative analysis of the spectra revealed about 95±5% release of the drug. This result was obtained amid the formation of only





**Fig. 5.6 | Magnetic-field-triggered biocatalysis in the cell culture.** **a–c,** *Optical images of 4T1 breast cancer cells incubated for 4.5 h with a 1:1 mixture of S-nanoparticles and rhodamine-B-silica-shell-labelled E-nanoparticles loaded with FD-BSA and papain, respectively. The images were obtained for samples with an attached magnet (top row) and with no magnet (bottom row): bright-field optical microscopy (a), fluorescent microscopy (b) and overlay of a and b images (c) demonstrating the uptake of NPs by the cells (red) and the release of the fluorescent dye in the cell location areas. All scale bars, 100  $\mu\text{m}$ .*

50% of S–E contacts in the aggregates, thus indicating that NPs form dynamic aggregates in the magnetic field and virtually all DOX–BSA is degraded and DOX is liberated in the biocatalytic reaction. Gel-electrophoresis experiments (*Experimental Details* Figs. 14 and 15) with DOX–BSA loaded NPs qualitatively confirmed the conclusions derived from the spectroscopic studies: BSA and DOX–BSA are degraded in the presence of papain into small fragments (15 kDa and



lower) within 1h; S-nanoparticles release fragments of DOX– BSA in the presence of E-nanoparticles if the magnetic field is on whereas much fewer low-molecular-mass fragments are observed if the magnetic field is off; and DOX–BSA is well preserved in S-nanoparticles as concluded from the control experiment with S-nanoparticles mixed with papain in solution.

Alternatively, the magnetically triggered release of DOX was monitored using microcalorimetry. A microcalorimeter was equipped with two glass ampules, one loaded with a mixture of the E- and S-nanoparticles and another with buffer. The thermal activity of the biocatalytic reaction was recorded by subtracting a signal of the buffer ampule from the reference NP-loaded ampule. Both ampules were equipped with a special shaft for insertion of the magnet. In the control experiment, the reaction was monitored without application of the magnet and no thermal activity was recorded from the first vial. The biocatalytic reaction was initiated by moving both preloaded magnets from the dry upper compartment of the ampule to the bottom compartment. The thermal activity associated with the reaction was monitored for more than 12 h (Fig. 4e). The feasibility of the developed drug delivery system in a biological environment was studied in vitro using 4T1 cells (murine breast cancer cell line). S- and E-nanoparticles were mixed in a 1:1 ratio and were added to the incubation medium (Fig. 5a).

A calcein AM cell assay was performed after 24 hours of incubation (Fig. 5b) and the per cent cell viability was evaluated based on cell counting. Relative to the PBS control experiment, at least 70% of cells remained alive when the nanoparticle concentration was below  $1.25\mu\text{g ml}^{-1}$  (Fig. 5c,f). When a magnet was attached to the bottom of the cell culture dish, there was a significant drop of cancer cell viability at all particle concentrations (Fig. 5d,f). This was attributed to magnet-triggered DOX release and the following cell apoptosis. In a separate

experiment, we obtained proof of the nanoparticle internalization. The 4T1 cells were incubated in the presence of fluorescein-silica-shell-labelled S-nanoparticles. Plane and 3D-confocal images clearly demonstrate the internalization of the NPs by the cells (Fig. 5e). The internalization was proved also using fluorescence properties of S-nanoparticles loaded with DOX-BSA conjugate (*Experimental Details* Fig. 16).

The experiments with the cell culture demonstrated NP internalization and their cytotoxicity upon application of the magnetic field. The reference experiments with NPs with no polymeric shell and polymer brush decorated NPs loaded with FD-BSA and papain showed no obvious cytotoxicity at concentrations below  $50\mu\text{g ml}^{-1}$  (*Experimental Details* Figs. 18 and 19). The low cytotoxicity of NPs was confirmed by multiple repetitions of the reference experiments, which were in good agreement with the literature<sup>162,163</sup>.

To exclude possible artefacts associated with cell viability we designed additional experiments that proved magnetic-field- triggered biocatalysis in the cell culture. The cells were incubated with a 1:1 mixture of the S- and rhodamine-B-silica-shell-labelled E-nanoparticles ( $0.05\text{mg ml}^{-1}$  total concentration) loaded with FD-BSA and papain, respectively. FD is quenched in the FD-BSA conjugate, as shown in the reference experiment using fluorescence microscopy (Fig. 6b, bottom). However, application of the magnet led to merging NPs and initiation of the biocatalytic reaction of FD-BSA proteolysis in the nanocompartments. The latter was detected by the intense fluorescent signal of the liberated unquenched FD (Fig. 6b, top). A less intense red fluorescence of rhodamin-B embedded in the silica shell of NPs is observed for both samples with a magnet and for the control experiment (Fig. 6b). The overlaid bright field (Fig. 6a) and fluorescent microscopy (Fig. 6b) images of the same area of the cell culture confirmed that the

FD was released in the areas occupied by the cells upon the application of the magnetic field (Fig. 6c). The areas occupied by NPs and released FD appear yellow owing to the combination of red NPs and green FD. A large surface area is indeed coloured green because of a much higher concentration of the released FD.

## CHAPTER 6

### EXPERIMENTAL DETAILS

**Materials.** Ferric chloride, ferrous chloride, copper(ii) bromide, concentrated nitric acid, hydrochloric acid, trisodium citrate, silicon tetraethoxide (TEOS), (3-aminopropyl)triethoxysilane (APS), triethylamine,  $\alpha$ -bromoisobutyryl bromide (BIB), ethyl  $\alpha$ -bromoisobutyrate (EBIB), *N,N,N',N'',N'''*-pentamethyldiethylenetriamine (PMDTA), ascorbic acid, tin(ii) 2-ethylhexanoate (THE), methanesulfonic acid, glutaraldehyde, 1-ethyl-3-(3-dimethylaminopropyl) carbodiimide hydrochloride (EDC), *N*-hydroxysuccinimide (NHS), papain, uorescein-labelled bovine albumin (FD-BSA), uorescein isothiocyanate (FITC), rhodamine B isothiocyanate (RITC), suberic acid bis(*N*-hydroxysuccinimide ester) (SABNHS), and organic solvents ethanol, anisole, chloroform and dichloromethane were purchased from Sigma-Aldrich and used as received. Monomers for grafting of a block copolymer of polyacrylic acid (PAA) and poly(ethylene glycol) methyl ether acrylate (PEGMA) or PAA-*b*-PPEGMA: *tert*-butyl acrylate (TBA) and PEGMA with a number average molecular mass of 480 g mol<sup>-1</sup> were purchased from Sigma-Aldrich and purified using a flash- chromatography column containing inhibitor removers (Sigma #311340 and Sigma #311332). Doxorubicin hydrochloride (DOX) was purchased from Oakwood Chemical and used as received.

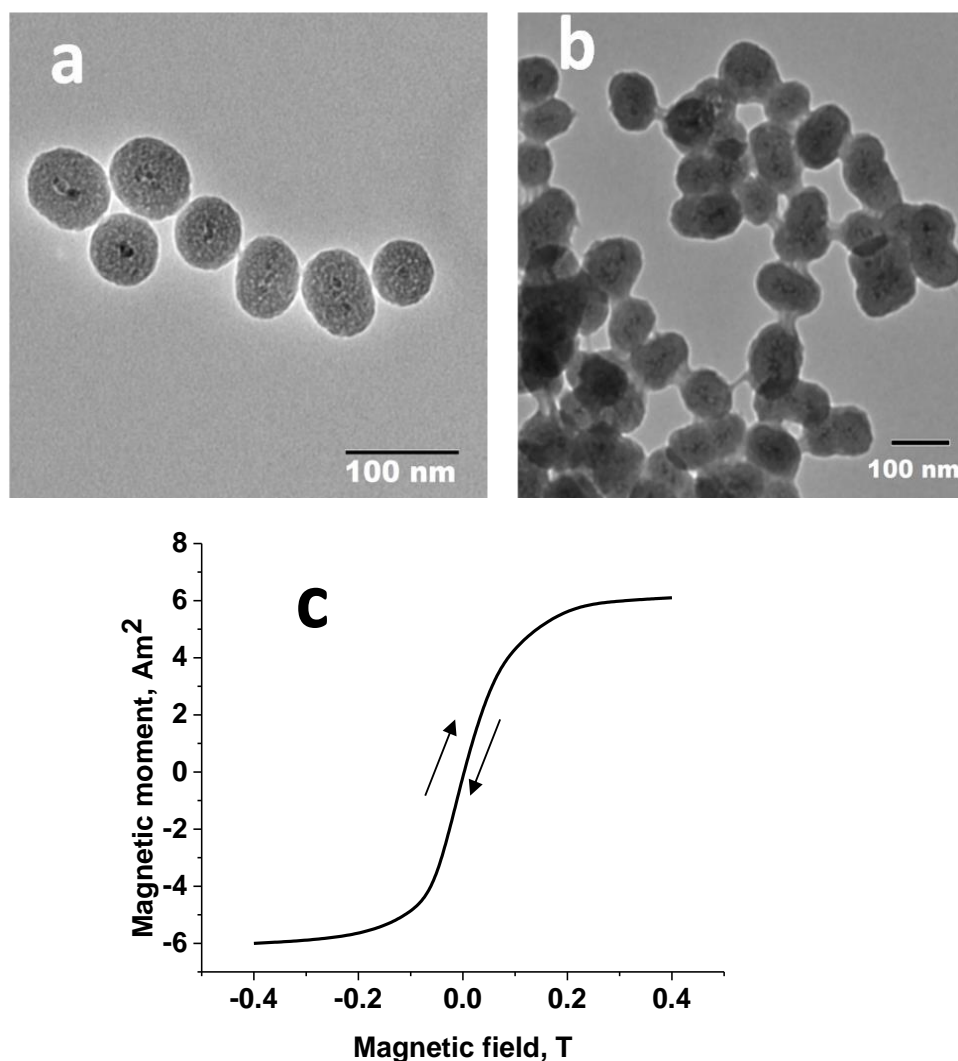
Phosphate-buffer saline (PBS), pH 7.4 at 25 °C was prepared using one Sigma pouch by dissolving it in 1 l of deionized (DI) water. 2-(*N*-morpholino) ethanesulfonic acid buffer (MES; 0.1 M; pH 4.7–5.0 at 25 °C) was prepared by dissolving 0.1 mol MES and 0.07 mol NaCl in 1 l

DI water. A Bradford protein assay, BCA Protein Assay Kit, Zeba Spin Desalting Columns and LIVE/DEAD Viability/Cytotoxicity Kit for mammalian cells were purchased from Thermo Fisher Scientific. Roswell Park Memorial Institute medium (RPMI 1640), 0.25% trypsin-EDTA, fetal bovine serum, and antibiotics: penicillin and streptomycin were purchased from Sigma-Aldrich. The mouse 4T1 breast tumour cells used for the present cultures were provided by J. Xie, University of Georgia, USA. A permanent magnet NdFeB, Grade N42 (K&J Magnetics, Pipersville, PA) was used in the experiments.

**6.1 Synthesis of magnetite–silica core–shell nanoparticles.** The superparamagnetic NPs were synthesized using a co-precipitation method as described elsewhere<sup>164</sup>. Iron chloride salts, 4.43 g  $\text{FeCl}_3 \cdot 6\text{H}_2\text{O}$  and 1.625 g  $\text{FeCl}_2 \cdot 4\text{H}_2\text{O}$ , were dissolved in 190 ml of DI water with a stoichiometric ratio  $\text{Fe}^{3+}:\text{Fe}^{2+} = 2:1$  with magnetic stirring at room temperature. Then, 10 ml of 25% ammonium hydroxide was added immediately. Formation of a black precipitate was observed. The solution was stirred for an additional 10 min, then the precipitate was separated with a magnet and rinsed three times with DI water using magnetic separation. The colloidal dispersion of NPs was stabilized with citrate ions by a rapid rinsing of the precipitate twice with 2 M nitric acid aqueous solution, followed by the addition of 5 ml of 0.5 M trisodium citrate in water while maintaining pH 2.5 using a sodium hydroxide aqueous solution. After stirring for 1.5 h, NPs were magnetically separated, rinsed with DI water and diluted to obtain 100 ml (pH = 6) of the dispersion. The concentration of NP in the final stock dispersion was 2% wt. A modified Stöber method<sup>165</sup> was applied to coat NPs with a silica layer: 2 ml of the NP stock solution was diluted in a mixture of 160 ml ethanol and 40 ml DI water. Then, 5 ml of ammonium hydroxide was added to the NP dispersion. After 10 min of treatment in an ultrasonic bath, 1 ml of TEOS

was added dropwise into the reactor. The synthesis was carried out at 0 °C and under sonication for 3 h. The reaction was terminated by the addition of several droplets of 10% HCl followed by precipitation of silica-coated NPs. The precipitate was collected by a magnet and rinsed three times with DI water. Then the precipitate was suspended in 50 ml DI water with sonication. The resulting product is a stable 2 mg ml<sup>-1</sup> dispersion of NPs. The particle structure (TEM image) and dimensions are shown in *Experimental Details* Figs. 1a and 3 (line 1). The NPs were characterized using a magnetometer AGM 2900 (Alternating Gradient Magnetometer by Princeton Inc.). As shown in *Experimental Details* Fig. 1c, the NPs demonstrate superparamagnetic behaviour with no spontaneous magnetization. In the following experiments with the NPs, the external magnetic field was in a range from 0.1 to 0.2 T when magnetization of NPs is close to its saturation.

**6.2 Labelling of the nanoparticles with fluorescent dyes.** Magnetic nanoparticles were labelled via inclusion of two different fluorescent dyes in the silica shell of NPs: 0.094 g of APS was added to 0.12 g of FITC or RITC (for green and red particles, respectively) dissolved in 10 ml of anhydrous ethyl alcohol; the reaction was carried out for 17 h by stirring the reaction mixture in dark conditions under a dry nitrogen gas. The synthesized conjugates, APS–FITC and APS–RITC, were used immediately after preparation: 4.8 ml of the stock solution of the magnetic nanoparticles was added to a mixture of 760 ml ethanol and 200 ml DI water; ammonium hydroxide (24 ml, as received) was added and the mixture was stirred and sonicated for 10 min to disperse the nanoparticles; afterwards, a mixture of 240 µl of TEOS and 300 µl of APS–RITC (or APS–FITC) were added dropwise to the particle dispersion and the mixture was stirred for 4 h in dark conditions. The silica-coated NPs were precipitated by adding hydrochloric acid, centrifuged and dispersed in ethanol. Rinsing in a fresh portion of ethanol was



**Figure 6.1. Characterization of magnetic nanoparticle.** Transmission electron microscopy (TEM) images of NPs: a)  $50 \pm 5$  nm silica coated NPs reveal an 15 nm iron oxide magnetic core and a 20 nm thick silica shell; b) NPs with  $12.5 \pm 5$  nm grafted PAA-*b*-PPEGMA brush observed as polymer structures bridging between the aggregated particles (note that the particle aggregates are formed among the NPs deposited on the TEM grid during solvent evaporation) ; c) magnetic properties of the NPs are consistent with superparamagnetic behavior.

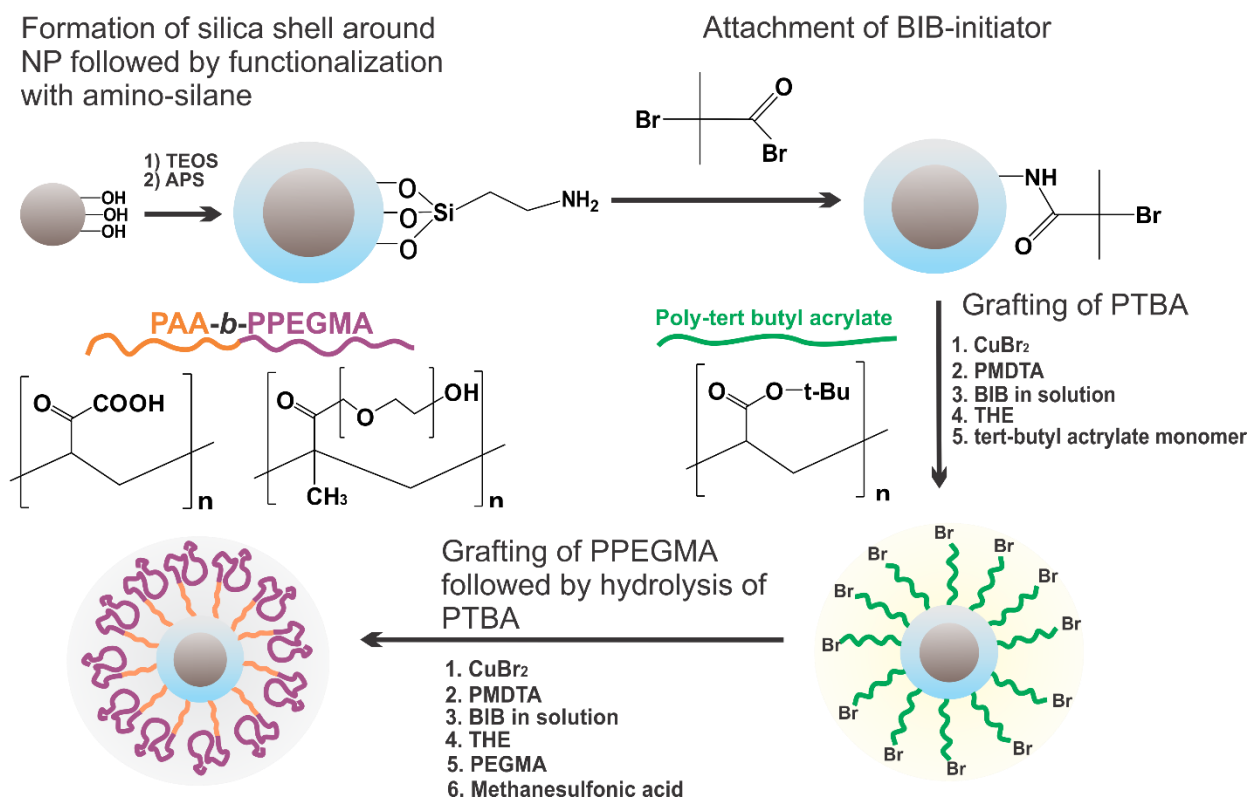
repeated three times to purify the nanoparticle dispersion. The dye-loaded silica shell was sealed with an additional silica coating to preserve fluorescent molecules. The nanoparticles were dispersed in a mixture of 30 ml ethanol and 7 ml DI water; 700  $\mu$ l of ammonium hydroxide was added and then 3  $\mu$ l of TEOS was added to the dispersion. The mixture was stirred overnight and particles were rinsed with three centrifugation–precipitation cycles in ethanol.

**6.3 Grafting of PAA-b-PPEGMA block copolymer from the nanoparticle surface.** Grafting of the PAA-b-PPEGMA block copolymer from the surface of nanoparticles was conducted using the activator generated by electron transfer for atom transfer radical polymerization (AGET-ATRP) mechanism<sup>166</sup>. The polymerization was conducted in two steps. First, poly *tert*-butyl acrylate (PTBA) was grafted by polymerization of TBA. The AGET-ATRP of PTBA was followed by grafting of PPEGMA blocks using the same AGET-ATRP mechanism. Finally, the post polymerization treatment was applied to hydrolyse the PTBA blocks and convert them into PAA blocks. The synthetic steps are shown in Experimental details Fig. 2. The polymerization steps are described below in detail.

*Immobilization of initiator.* Silica-coated NPs were transferred to an ethanol dispersion; the stock NP solution was mixed with ethanol and the nanoparticles were extracted using magnetic separation. This was repeated several times to decrease the concentration of water in the NP ethanol dispersion. Finally,

the NPs were added to a 1% APS ethanol solution and stirred for 12 h. APS immobilization was followed by three rinses with ethanol. NPs were incubated for 1 h in 100 ml dry dichloromethane with 2 ml of triethylamine and 1 ml of BIB. The initiator-functionalized particles were rinsed three times with chloroform and ethanol.



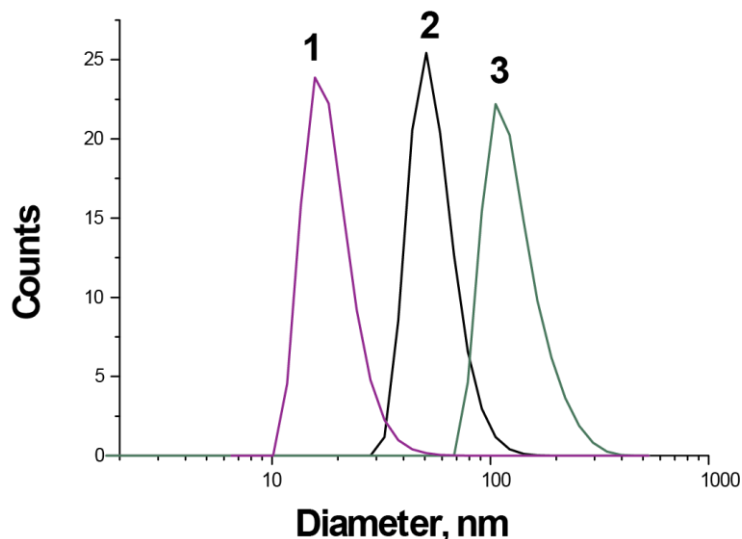


**Figure 6.2. Schematic of the synthesis of functional NPs.** The schematic depicts the synthesis of NPs step-by-step as described in Methods.

*Polymerization.* A TBA monomer was purified using a flash-chromatography column loaded with inhibitor removers. 210  $\mu$ l of a 0.1 M CuBr<sub>2</sub> ethanol solution, 320  $\mu$ l of a 0.5 M PMDTA ethanol solution and 37.5  $\mu$ l of a 0.68 M EBIB ethanol solution were added to 45 ml of a 30% monomer solution in anisole. About 1 g (NPs by dry weight) of a concentrated slurry of the initiator-functionalized NPs was added to the solution. In this solution, EBIB (or Br-initiator in solution) was added to synthesize the block-copolymer in solution for the molecular mass analysis. The reaction mixture was deoxygenated by purging nitrogen for 20 min and then the solution was heated at 70 °C. 500  $\mu$ l of 1 M ascorbic acid (or in some experiments 500  $\mu$ l THE) was added to the solution and the reactor was sealed. The polymerization reaction was

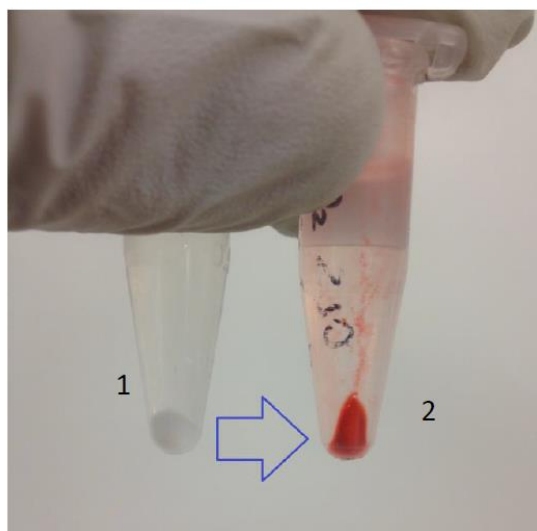
terminated in 76 h by opening the vial to air and rapidly cooling the reactor. The polymer from the solution was separated from the nanoparticles by centrifugation, re-precipitated three times with 30% aqueous ethanol and analyzed with gel permeation chromatography (GPC). A choice of ascorbic acid versus THE was dictated by the adjustment of the polymerization rate. The polymerization reaction in the presence of THE was slower.

Grafting of the second PPEGMA block was carried out by a similar procedure: a 25% PEGMA solution in ethanol was polymerized for 60 min at room temperature. PTBA-*b*-PPEGMA was converted to PAA-*b*-PPEGMA using 1% methane sulfonic acid in ethanol. After hydrolysis, the nanoparticles were rinsed three times with chloroform, ethanol, and water and dried at 50 °C in an oven. The NP powder is easily redispersible in water and forms a stable colloidal dispersion with an average nanoparticle size of 45 nm (Experimental details Fig. 3, line 2) and zeta potential  $\zeta = -30$  mV (pH 7.4).



**Figure 6.3. DLS particle analysis in aqueous dispersions at pH 7.5. 1) NPs, 2) silica coated NPs, 3) NPs with grafted PAA-*b*-PPEGMA.**

**6.4 Functionalization of nanoparticles with proteins and DOX.** EDC-NHS conjugation was used for the conjugation of papain and FD-BSA to the polymer-coated magnetic nanoparticles. Carboxylic acid groups of the PAA polymeric layer reacted with EDC-NHS reagents to form an intermediate active ester that then reacts with primary amines of FD-BSA or papain to form covalent amide bonds. The nanoparticles were dispersed in a 10 ml MES buffer solution (pH 4.5) at a concentration of  $1.6 \text{ mg ml}^{-1}$ . Then, 3 mg of EDC (2 mM) and 6 mg of NHS (5 mM) were added to the nanoparticle dispersion; the reaction was conducted for 20 min at  $36^\circ\text{C}$ . The nanoparticles were rinsed twice with PBS buffer and then 5 ml of the dispersion was divided between two vials with a concentration of  $3 \text{ mg ml}^{-1}$  in each.

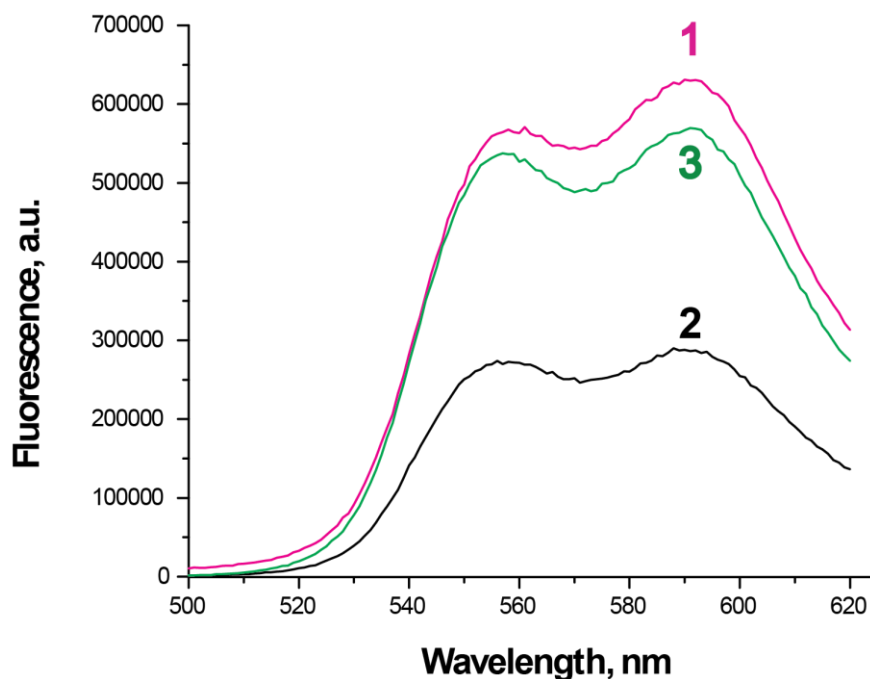


**Figure 6.6. Reference experiments for the nanoparticles with no dark-brown iron oxide core for improved color contrast.** The silica nanoparticles decorated with PAA-*b*-PPEGMA brush were used for loading (conjugation) with DOX-BSA. Appearance of the purified and centrifuged NPs: (1) - prior to conjugation and (2) after conjugation and purification.

Afterwards, 3 mg of the FD-BSA powder was added to the first vial and 125  $\mu\text{l}$  of a 28-mg  $\text{ml}^{-1}$  papain solution was added to the second. Both enzymes were added in great excess to approach the saturation of the brush loading with the proteins. The conjugation reaction was carried out for 4 h at room temperature with delicate shaking. The nanoparticles were washed five times using centrifugation for their separation. The supernatant was periodically analysed to monitor the presence of proteins using a fluorometer. Rinsing was repeated until no trace of the labelled proteins were observed in the supernatant.

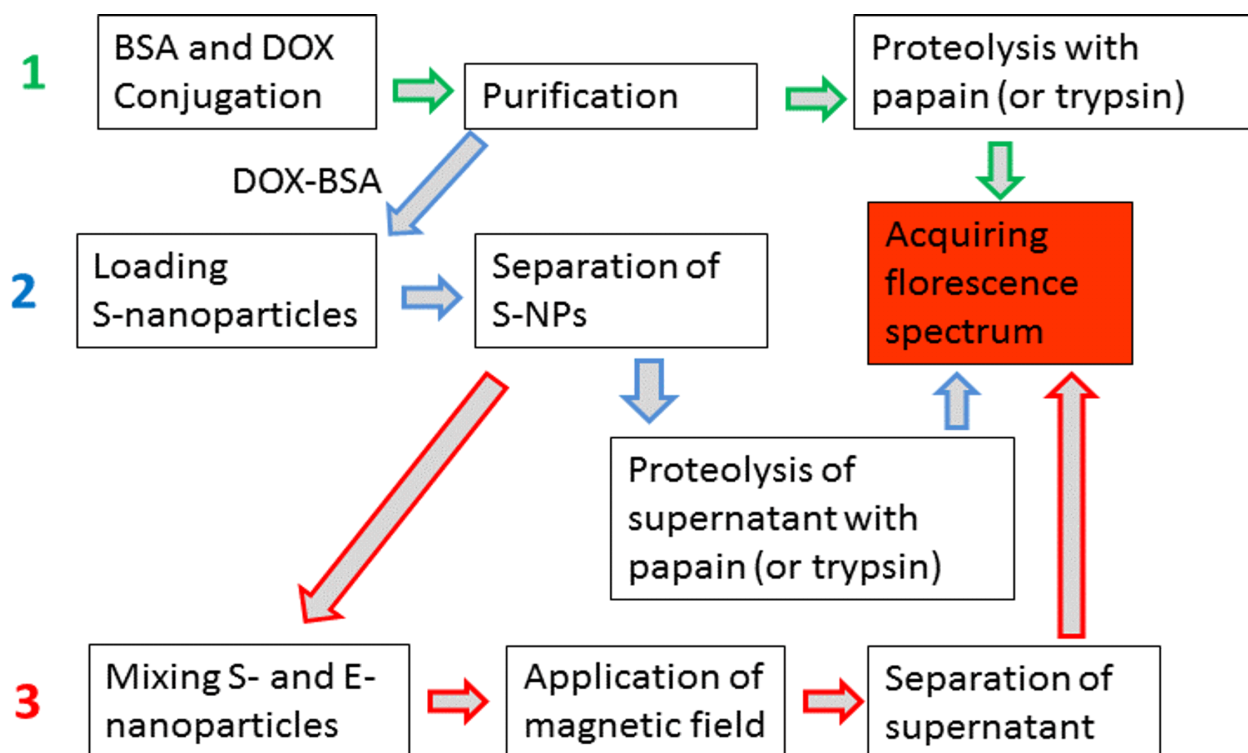
*Conjugation of DOX.* First, DOX was conjugated to BSA. 2 mg of BSA and 1 mg of DOX were added to 1 ml of 0.1% glutaraldehyde solution in PBS. DOX was dissolved first in 20  $\mu\text{l}$  dimethylsulfoxide (DMSO) and then added to the aqueous solution of BSA. The reaction proceeded for 30 min at room temperature. The synthesized BSA-DOX conjugate was purified using a Zeba Spin chromatographic column. The purified BSA-DOX was analysed spectroscopically to confirm

and quantitatively evaluate the conjugation, as described below. The results show that about 50% of the initially reacted amount of DOX was bound to BSA (see *Experimental Details* Methods and Fig. 9). Afterwards, BSA-DOX was conjugated with S-nanoparticles as described above (the same protocol as for conjugation of FD-BSA). The S-nanoparticles appeared as red-coloured material (*Experimental Details* Fig. 6). Loading of the nanoparticles with proteins was estimated with fluorescence spectroscopy (*Experimental Details* Figs. 7 and 8) and gravimetrically by spectra and weight change before and after loading (*Experimental Details* Table 2). The discrepancy between the two methods was less than 5%.



**Figure 6.7. DOX release monitored with fluorescence spectroscopy.**

*Fluorescence spectra (emission) of: (1) a mixture of BSA (2 mg/ml) and DOX (1 mg/ml) prior to conjugation; (2) after conjugation, and (3) after proteolysis with papain.*



**Figure 6.8. Schematic for the fluorescence spectroscopic analysis of the DOX conjugation and release.** (1) DOX and BSA conjugation; (2) DOX-BSA loading into S-nanoparticles; (3) release of DOX from a mixture of S- and E-nanoparticles at the applied magnetic field.

**Table 6.2. Loading of E- and S-nanoparticles.**

Protein	E-nanoparticles			S-nanoparticles		
	mol/g	%	mol/single particle	mol/g	%	mol/single particle
PAA-b-PPEGEMA	$11.2 \pm 2 \cdot 10^{-6}$	$20.4 \pm 2$	$6.9 \pm 1 \cdot 10^{-21}$	$11.2 \pm 2 \cdot 10^{-6}$	$20.4 \pm 2$	$6.9 \pm 1 \cdot 10^{-21}$
BSA	-	-	-	$4.9 \pm 0.2 \cdot 10^{-6}$	$32.7 \pm 1.5$	$2.8 \pm 0.1 \cdot 10^{-21}$
DOX	-	-	-	$140 \pm 6 \cdot 10^{-6}$	$8.0 \pm 0.3$	$80 \pm 3.5 \cdot 10^{-21}$
papain	$15 \pm 0.8 \cdot 10^{-6}$	$35 \pm 2$	$9.2 \pm 0.4 \cdot 10^{-21}$	-	-	-

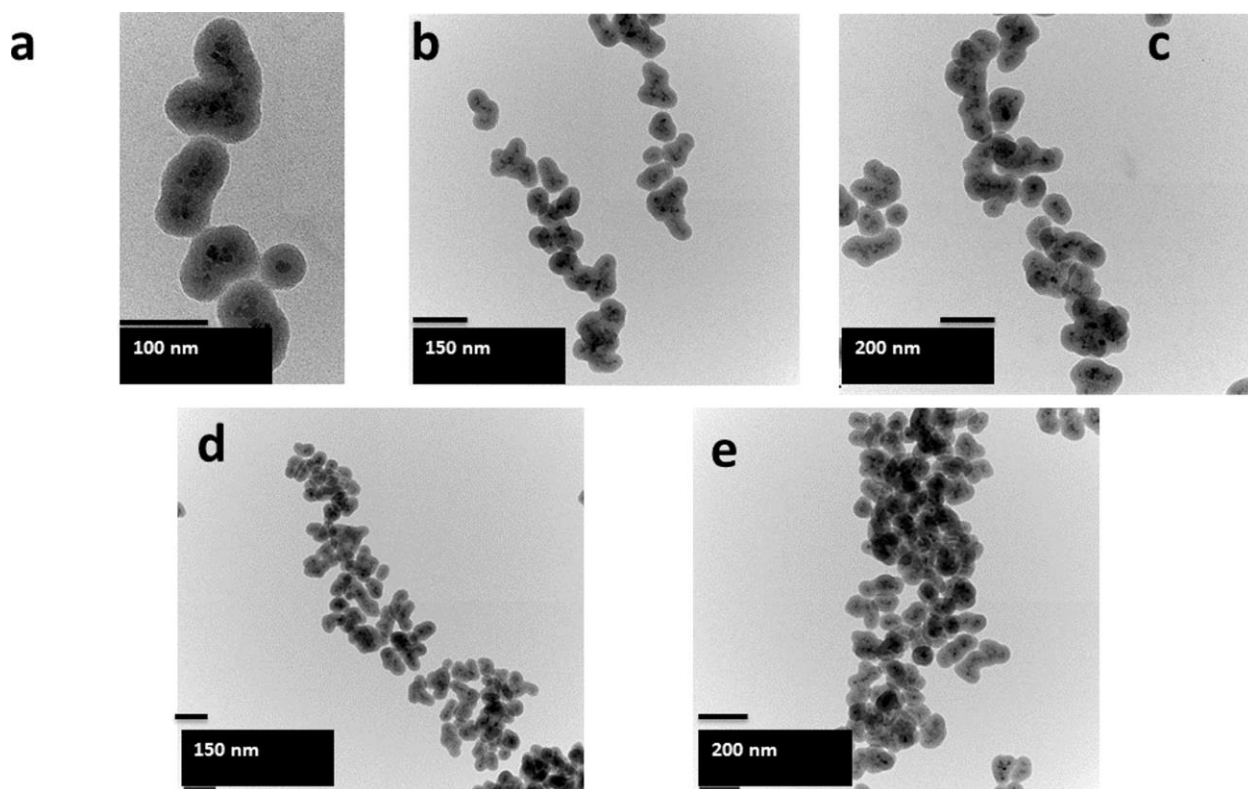
*Molar ratios of the conjugated components:*

*Molar ratio (polymer brush):BSA = 1:0.4;*

*Molar ratio (polymer brush):papain= 1:1.3;*

*Molar ratio DOX:BSA= 28.6:1.*

**6.5 Aggregation of particles in magnetic field.** Dispersions of NPs of different concentrations (0.001–1%) were prepared in PBS solutions and exposed to the magnet using several different experimental set-ups. The formed aggregates were visualized in dry conditions as shown in *Experimental Details* Fig. 12, where exposure time increases from (a) to (e).



**Figure 6.12. TEM images of NPs aggregates.** The aggregates were deposited on the TEM grid from a 0.01% dispersion upon exposure to magnetic field for different periods from 5 s (a) to 100 s (e).

Aggregate formation is rapid, so the exact time for each aggregate size was not determined exactly. Similar experiments were conducted using Si wafers when the aggregates were deposited and visualized using AFM (Fig. 3b). The formation of aggregates in solution was visualized using cryo-TEM (Fig. 3a) or for a greater concentration of NPs (1%) using dark-field optical microscopy (Fig. 3c). The results proved that increased time and NP concentration result

in an increase of the aggregate size from 2–3-mers to larger 3D-strings of NPs.

**6.6 Smart compartmentalization.** EDC-NHS conjugation is conducted at pH 4.5–5.0 when PAA acid is partially negatively charged (the  $pK_a$  of PAA is a function of the degree of dissociation and ionic strength, at pH 5 and a relatively high local concentration of PAA in the brush, the  $pK_a$  is in the range 4.5–5.0; ref. <sup>167</sup>) while papain is positively charged (the isoelectric point of papain is between 8.5 and 9.5, Sigma Papain P4762 datasheet) and FD-BSA has no overall charge (the isoelectric point of FD-BSA is 4.8; ref. <sup>168</sup>). The interaction of proteins with polyelectrolyte brushes is a complex phenomenon<sup>169</sup>. Here we partially simplify the discussion and focus on the major conclusions. Although with high ionic strength buffer solutions (about 160 mM) electrostatic interactions are largely screened, electrostatic interactions are beneficial for the introduction of enzymes in the PAA polymer brush in the first stage prior to covalent binding. The conjugation is conducted in conditions of a very high excess of proteins to saturate the PAA brush. PPEGMA block stabilizes particles sterically, however they create a relatively low barrier for the transport of small globular proteins such as papain and FD-BSA.

The performance of the brush-decorated NPs was studied in PBS buffer solutions or a cell culture medium at physiological pH 7.4. At these conditions PAA should be much more negatively charged. However, the presence of the conjugated proteins and high ionic strength of the environment results in screening of electrostatic interactions, so that the major repulsive properties of the brush are caused mainly by the osmotic pressure in the PAA blocks highly loaded with proteins. This steric repulsion mechanism is enhanced by the additional steric repulsion of PPEGMA blocks. A combination of these two effects results in the ‘insulation’ of the conjugated and hidden proteins inside the brush. We term this mechanism smart



compartmentalization. The semi- permeable block-copolymer brush becomes virtually impermeable for proteins and other large molecules as soon as it becomes saturated in the conjugation step. This smart compartmentalization explains negative reference experiments demonstrated in Fig. 2b: protein in solution cannot interact with proteins loaded into the PAA brush. If magnetic field is on, the magnetic force overcomes the osmotic pressure and nanoparticles merge together to form a biocatalytic nanocompartment.

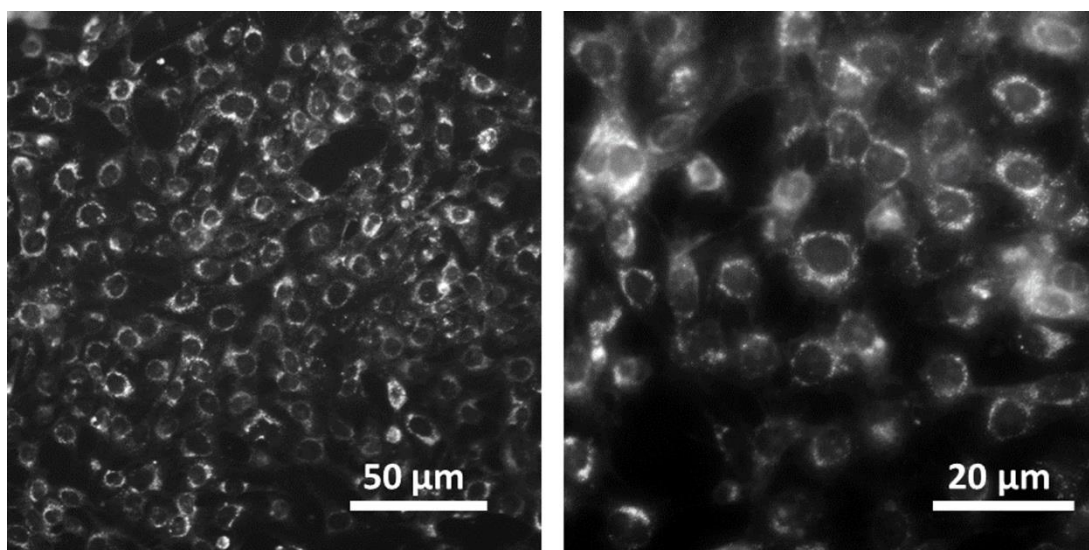
**6.7 Experiments with cell culture.** Preparation of cell culture for the experiments. 4T1 cell line (American Type Culture Collection) was cultured using RMPI 1640 medium supplemented with 10% fetal bovine serum and 1% penicillin– streptomycin solution. e cells were incubated under humid conditions at 37 °C and 5% CO. e cell line has not been authenticated or tested for mycoplasma 2 *NP uptake by cells*. 4T1 cells were incubated in fresh medium for 72 h to allow cell attachment and proliferation. The cell culture at 100% coverage of the cell culture dish was treated with a trypsin solution. The detached cells were separated by centrifugation (1,000 g for 10 min) and seeded in fresh medium. The cell culture was used after 24 h incubation at about 40% coverage of the cell culture dish. Afterwards, the cells were rinsed with fresh medium (the unattached and dead cells were removed).

*Internalization of NPs.* FD-labelled-silica-shell S-nanoparticles (labelled with APS- FITC as described above) were added to the incubation medium (concentration of NPs in the medium was 0.1 mg ml<sup>-1</sup>). After 12 h incubation, the cell culture was rinsed in fresh medium to remove uninternalized particles. The cells were examined using a laser confocal microscope.

*Magnetic field-triggered biocatalysis in cell culture.* S- and rhodamine-B-silica-shell- labelled E-nanoparticles loaded with FD-BSA and papain, respectively, were mixed in a 1:1 ratio and were

added to the incubation medium (the NP concentration in the medium was  $0.05 \text{ mg ml}^{-1}$ ). Two similar samples were incubated for 4.5 h: one sample was supplied with an attached magnet, while another sample was used for a control experiment with no magnet. The cells in both samples were rinsed in fresh medium to remove uninternalized particles. The cell samples were analyzed with optical microscopy using bright field and fluorescent microscopy modes (*Experimental Details* Figs. 16 and 17).

*Release of therapeutic drug DOX.* S- and E-nanoparticles loaded with BSA- conjugated-DOX and papain, respectively, were mixed in a 1:1 ratio and were



**Figure 6.16.** *Fluorescent microscopy images of 4T1 cell with internalized S-particles.*

added to the incubation medium at different concentrations, as shown in Fig. 5f. Uptake of the S-particles was evidenced by fluorescent microscopy imaging owing to the fluorescent properties of DOX (*Experimental Details* Fig. 16).

A calcein AM cell assay was performed after 24 h of incubation (Fig. 5b). The per cent cell viability was evaluated by cell counting. The assay was performed for a series of samples

including samples (i) with no NPs added (control experiment), (ii) with added NPs and no magnet attached, and (iii) with added NPs and an attached magnet. The experiment was repeated three times. Representative images of two experiments are shown in *Experimental Details* Fig. 17.

**Data availability.** The data that support the plots within this paper and other findings of this study are available from the corresponding author upon reasonable request.


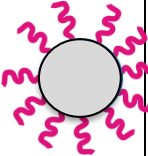
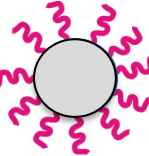
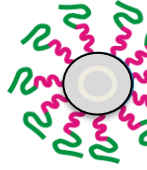
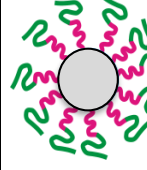
Received: 17 June 2017; Accepted: 11 October 2017; Published online: 20 November 2017

## **Experimental details Methods**

### **6.8 Characterization of the Polymer Brushes**

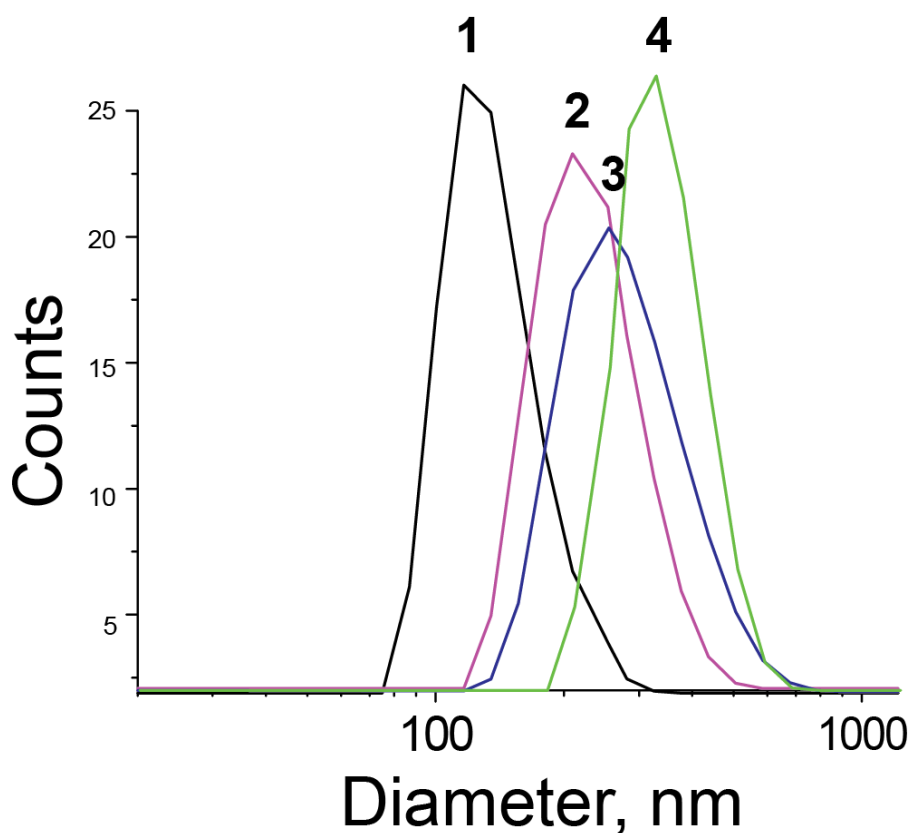
PAA-*b*-PPEGMA block copolymer brushes were grafted from the surface of NPs, reference 100 nm silica nanoparticles and reference Si-wafer substrates. The polymerization conditions described in Methods were optimized to obtain similar characteristics of the brushes decorating the model substrates: silica nanoparticles and Si-wafers, while the polymerization time was two-fold shorter for NPs than for silica nanoparticles and Si-wafers. The purpose of this alternation was to synthesize brush-decorated magnetic nanoparticles with a diameter of about 100 nm, which is compatible with many practical applications in biological systems. As for the model experiments, two times thicker brushes facilitated the analysis of the molecular characteristics of the brushes. The model substrates were used to apply different characterization tools and verify the structure and molecular characteristics of the polymer brushes since the analysis of polymer brushes grafted from NPs has multiple limitations.

**Table 6.1.** Molecular characteristics of the polymer brushes grafted from the surface of silica particles and Si-wafers

Schematics					
	Silica core	Core-shell particle with grafted PTBA	Core-shell particle with grafted PAA	Core-shell particle with grafted PAA- <i>b</i> -PPEGMA	Core-shell particle with grafted PAA- <i>b</i> -PPEGMA
Diameter, $\pm 10$ nm DLS measured at pH	100 4.5-5.0	-	190 4.5-5.0	230 4.5-5.0	275 7.4
Diameter, $\pm 5$ nm AFM (dry brushes)	100	125	115*	150	150
$\zeta$ -potential, $\pm 10$ mv measured at pH	-40 4.5		-50	-20 4.5	-10 7.4
Mw of grafted polymers, g/mol $\pm 5\%$ ; PDI	-	23500 1.45	13200* 1.45	48000*	48000*
Dry brush thickness, $\pm 1$ nm: AFM for particles/Ellipsometry for Si-wafers	-	12.5/14	7.3*	25	25
Water swollen brush thickness (DLS), $\pm 10$ nm	-	-	45	65	87
Swelling ratio of the brush at pH	-	-	6 4.5	2.6 4.5	3.5 7.4
Grafting density, $\pm 0.06$ nm <sup>-2</sup>	-	0.34	0.34	0.34	0.34
Distance between grafting points, $\pm 0.15$ nm	-	1.9	1.9	1.9	1.9

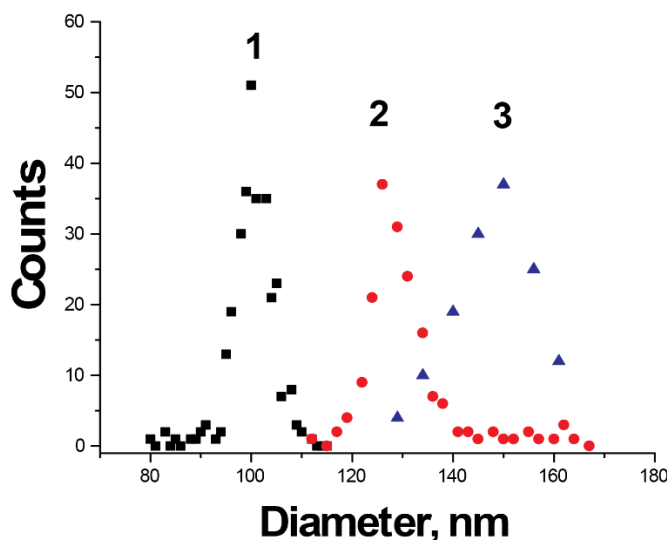
Dynamic light scattering (DLS), atomic force microscopy (AFM) and ellipsometry methods were used to estimate thickness of the polymer brushes grafted from the surface of silica nanoparticles

and Si-wafers in dry state (*Experimental Details* Table 1, Figure 4 and Figure 5). The results show that in both cases the brush thicknesses are identical suggesting that there is no substantial effect of the substrate curvature on the grafting. Molecular mass of PTBA in solution was characterized using gel-permeation chromatography (GPC):  $M_n = 23500$  g/mol;  $M_w = 31700$  g/mol, polydispersity index  $PDI = 1.45$ . We experienced problem to extract and analyze PAA and PAA-*b*-PEGMA from solutions. Hence, the molecular characteristics were estimated using molecular characteristics of



**Figure 6.4. DLS measurements of silica nanoparticles in aqueous suspensions.**

1) particles as received, pH 7.4; 2) NPs with grafted PAA, pH 7.4; and 3-4) NPs with grafted PAA-*b*-PPEGMA 3) at pH 4.5 and 4) at pH 7.4.



**Figure 6.5. AFM analysis of silica particles: 1) original unmodified NPs; 2) NPs with grafted PTBA; 3) NPs with grafted PAA-*b*-PPEGMA.**

PTBA brushes based on several assumptions. Assumption 1: the brush thickness change after post-polymerization treatment (hydrolysis of PTBA blocks) corresponds to 100% hydrolysis of PTBA. Thus, based on the difference of molecular mass of the monomeric units (acrylic acid 72.06 g/mol and *tert*-butyl acrylate 128.17 g/mol) the thickness of the dry PAA brush is 56% of the PTBA brush.<sup>129</sup> Assumption 2: The grafting density of the polymer chains on the surface remains unchanged after each polymerization and post-polymerization step. This assumption is applicable if side reaction in all steps is minimized. Assumption 3: The swelling degree of the brushes of the same composition and the same grafting density remains unchanged in the same solvent within the narrow range of molecular masses of the grafted chains. By applying these three assumptions we estimated molecular characteristics of the brushes as follows.

*For brushes grafted from the surface of silica nanoparticles*

*Grafting density* was estimated using the following relationship: grafting density  $\sigma = N_A \cdot H_{PTBA} \cdot d_{PTBA} / M_{nPTBA}$ , where  $N_A$  is the Avogadro's constant and  $d_{PTBA}$  is the density of PTBA

(1.023 g/cm<sup>3</sup>). The obtained value of  $\sigma = 0.34 \text{ nm}^{-2}$  corresponds to a 1.9 nm distance between the grafting points.

*Thickness of the PAA brush ( $H_{PAA}$ )* was estimated as a fraction of PTBA brush ( $H_{PTBA}$ ) after 44 % wt loss (hydrolysis) using an average thickness for the PTBA brush  $H_{PTBA}$  obtained by two measurement methods: AFM ( $H_{PTBA} = 12.5 \text{ nm}$ ) and ellipsometry ( $H_{PTBA} = 14 \text{ nm}$ ):  $H_{PAA} = 0.56 H_{PTBA} = 0.56 \cdot 13 \text{ nm} = 7.3 \text{ nm}$ .

*Molecular mass of PAA-brush  $M_{nPAA}$*  was estimated as a fraction of molecular mass of the PTBA brush ( $M_{nPTBA}$ ) after 44 % wt loss:  $M_{nPAA} = 0.56 \cdot 23500 \text{ g/mol} = 13\,200 \text{ g/mol}$ .

*Molecular mass of PAA-b-PPEGMA* was estimated using the relationship:

$$M_{nPAA-b-PPEGMA} = N_A \cdot H_{PAA-b-PPEGMA} \cdot d_{PAA-b-PPEGMA} / \sigma = 48000 \text{ g/mol};$$

where  $d_{PAA-b-PPEGMA}$  is the density of the copolymer estimated as 1.1 g/cm<sup>3</sup> (an average of PPEGMA 1.08 g/cm<sup>3</sup> and PAA 1.15 g/cm<sup>3</sup>).

*Molecular mass of PPEGMA block*

Estimated as a difference:  $M_{nPAA-b-PPEGMA} - M_{nPAA} = 48000 - 13200 = 34800 \text{ g/mol}$ .

*Swelling ratios* of the brushes were estimated as the ratio of the brush swollen in the solvent and the brush in the dry state.

*For brushes grafted from the surface of silica coated NPs:*

Thickness of the PAA brush was estimated as the thickness of the swollen brush divided by the swelling ratio:  $H_{PAA} = 16 \text{ nm} / 3.5 = 4.5 \text{ nm}$ ;

*Molecular mass of the PAA block* was estimated as  $M_{nPAA} = N_A \cdot H_{PAA} \cdot d_{PAA} / \sigma = 8600 \text{ g/mol}$ .

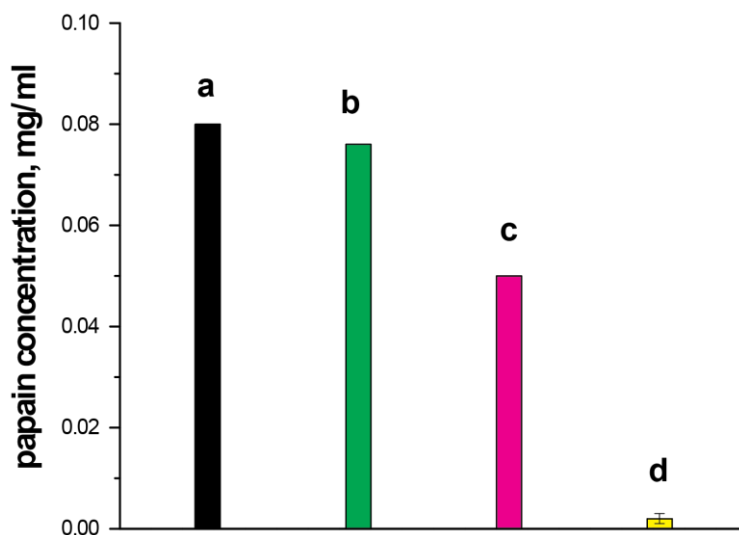
*Thickness of the PAA-b-PPEGMA brush* was estimated as the thickness of the swollen brush divided by the swelling ratio:  $H_{PAA-b-PPEGMA} = 32.5 \text{ nm} / 3.5 = 9.3 \text{ nm}$ ; this value is close to the value

of 12.5 nm obtained from the TEM images (Figure 6.1b). Using the TEM images, the grafted layer thickness was estimated as a half of the average distance between particles interconnected by polymer bridges. We assumed that in these areas the polymer layers were not degraded by the electron beam.

Molecular mass of the PAA-*b*-PPEGMA was estimated as  $M_{n\text{PAA-}b\text{-PPEGMA}} = N_A \cdot H_{\text{PAA-}b\text{-PPEGMA}} \cdot d_{\text{PAA-}b\text{-PEGMATBA}} / \sigma = 17000 \text{ g/mol}$ .

### 6.9 Evaluation of biocatalytic activity of the conjugated enzymes

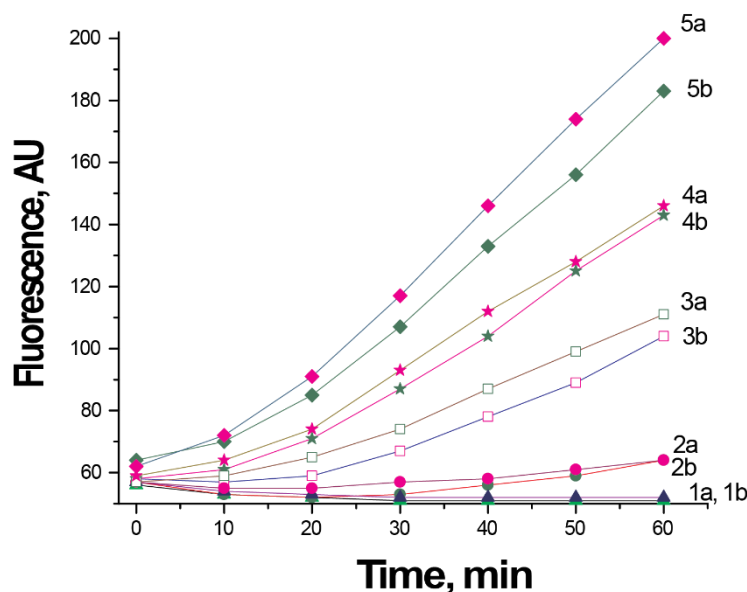
The effect of the conjugation on the biocatalytic activity of papain was studied using a series of model and reference experiments. In the experiments, papain and PAA ( $M_w = 240 \text{ kg/mol}$ ) were conjugated at different stoichiometric ratios using the EDC-NHS method as described in Methods yielding Papain-PAA conjugates. The conjugates were dialyzed for 16 h against MES buffer (pH 6.0) using a 100K membrane. In the control experiment, papain and PAA mixture (no EDC-NHS



**Figure 6.9. Concentration of papain in the dialysis flask.** a) Control: papain, prior to dialysis (black bar); b) Papain-PAA conjugate (green bar); c) mixture of papain (80 µg/ml) and PAA (1 mg/ml, red bar); and d) control, after dialysis of native papain (blue bar). The error bars show the standard deviation obtained from three repetitive experiments.



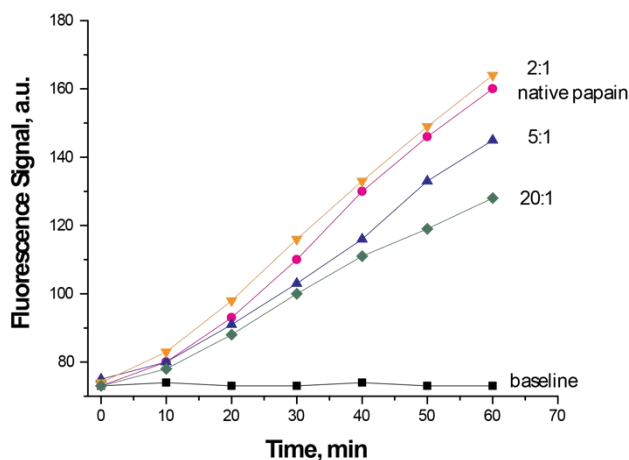
conjugation) was prepared and dialyzed. Dialysis of just papain solution was conducted as a



**Figure 6.10. Kinetics of proteolysis of FD-BSA catalyzed by Papain-PAA conjugates.** (1a,2a,3a,4a and 5a) at different conjugate concentrations (see *Experimental details Table 3*) vs the control kinetic data for FD-BSA proteolysis catalyzed by non-conjugated papain (1b, 2b, 3b, 4b and 5b) at the same concentrations of the enzyme.

control of the membrane permeability for papain. Papain concentrations in the dialysis flask were The control (*Experimental details* Figure 9) shows that the membrane is permeable for papain (compare (a) and (d) bars). About 60% of papain was bound to PAA in the mixture of papain and PAA prior to the conjugation reaction suggesting that papain has a high affinity to PAA due to the formation of a polyelectrolyte complex (compare (a) and (c) bars). After the EDC-NHS conjugation, only 5% of unbound papain was dialyzed out while 95% of papain were bound to PAA. (compare (a) and (b) bars). Thus, the conjugation of papain and BSA is highly efficient. The same results were obtained in the range of papain: PAA ratios from 2:1 to 20:1.

Biocatalytic activity of the Papain-PAA conjugates of different stoichiometric ratios was tested using kinetic experiments of proteolysis of FD-BSA. The kinetic curves



**Figure 6.11.** Kinetics of proteolysis of FD-BSA catalyzed by Papain-PAA conjugates with different PAA to papain molar ratios from 2:1 to 20:1 in the conjugates vs. control (native papain).

for a Papain-PAA conjugate with a stoichiometric ratio papain: PAA= 2:1 is shown in *Experimental Details* Figure 10 (concentrations are shown in *Experimental Details* Table 3).

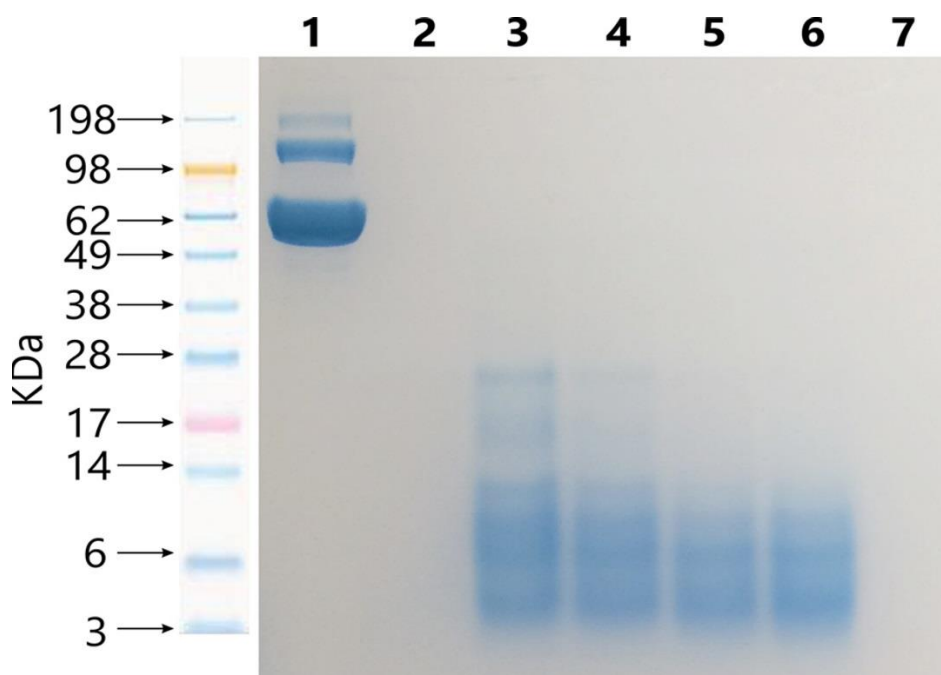
The control experiments were conducted for the same corresponding concentrations of non-conjugated papain. The results of the experiments are consistent with the statement that the effect of the conjugation on the biocatalytic performance of papain is minimal.

**Table 6.3.** Kinetic experiments for proteolysis of FD-BSA by Papain-PAA

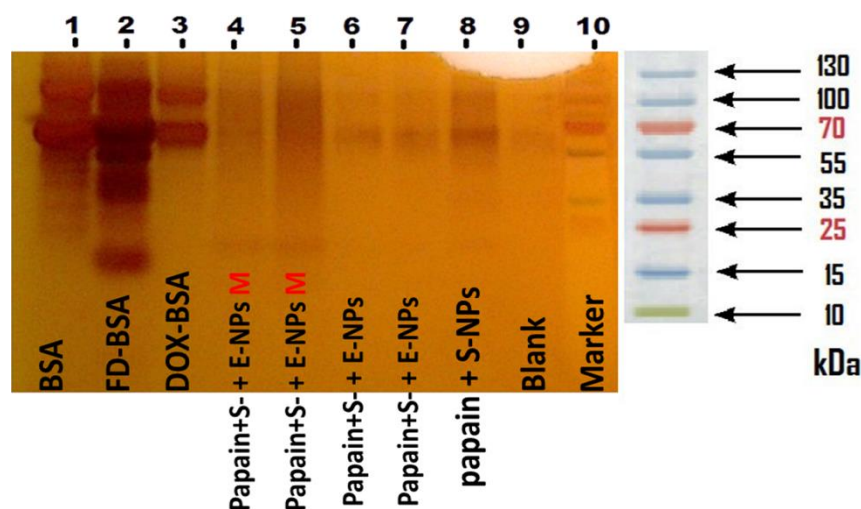
label	Enzyme form	Concentration of FD-BSA, $\mu\text{g/ml}$	Concentration of conjugate, $\text{ng/ml}$	Concentration of native papain	Concentration of conjugated papain, $\text{ng/ml}$
1a	conjugate	4.95	4.95	-	1.6
1b	native	4.95	-	1.6	-
2a	conjugate	4.76	23.8	-	7.9
2b	native	4.76	-	7.9	-
3a	conjugate	4.54	45.5	-	15.2
3b	native	4.54	-	15.2	-
4a	conjugate	4.16	83.3	-	27.8
4b	native	4.16	-	27.8	-
5a	conjugate	3.33	167	-	55.3
5b	native	3.33	-	55.3	-

### 6.10 Gel-electrophoresis method for testing of biocatalytic proteolysis of S-nanoparticles

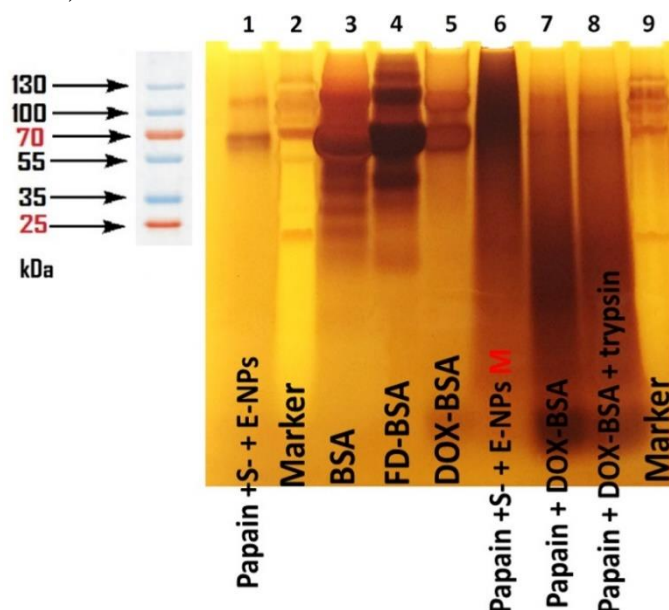
A series of experiments was conducted to monitor degradation of BSA loaded into S-nanoparticles and catalyzed by E-nanoparticles along with a number of reference experiments. After 1 h reaction time for a mixture of E-and S-nanoparticles in the PBS buffer, the mixture was separated by centrifugation and the supernatant was analyzed using gel-electrophoresis (*Experimental details* Figures 13-15).



**Figure 6.13. Proteolysis of FD-BSA (500  $\mu$ g) in PBS buffer solutions.** 1- Control, native BSA; 2-blank; 3-with added Papain-PAA (25 ng/ml); 4-with added Papain-PAA (50 ng/ml); 5-with added Papain-PAA (100 ng/ml); 6-control, with added papain (50 ng/ml); 7-blank.



**Experimental details Figure 6.14.** Release of products of proteolytic process (SDS-PAGE, silver staining) with involvement of S- and E-nanoparticles. (1) native BSA (control); (2) FD-BSA (control), (3) DOX-BSA (control); (4) and (5) S- and E-nanoparticles 1:1, magnetic field is ON; (6) and (7) S- and E-nanoparticles 1:1, magnetic field is OFF; (8) S-nanoparticles and papain mixture (control).



**Experimental details Figure 6.15.** Release of products of proteolytic process (SDS-PAGE, silver staining) with involvement of S- and E-nanoparticles. E- and S- nanoparticles mixture (1) – magnetic field OFF, (6) magnetic field ON and reference experiments for (7) papain mixed with DOX-BSA and (8) the same as (7) with added trypsin; (2) and (9) – markers, and controls: (3) BSA, (4) FD-BSA, (5) DOX-BSA. Concentration of proteins is 2 mg/ml in all cases.

In reference experiments, S-nanoparticles were mixed with papain and Papain-PAA conjugates. Additional reference experiments included mixtures of native BSA and BSA-PAA conjugates with native papain and Papain-PAA conjugates.

The reference experiments (*Experimental Details* Figure 13) demonstrate that that native and conjugated papain degrade BSA yielding short polypeptide fragments with molecular weight of several kg/mol and lower. Note, papain and Papain-PAA are not detected because of very small concentrations as compared with BSA.

We derived the following conclusions based on the experiments: a) BSA, FD-BSA and DOX-BSA are degraded in presence of papain into small fragments within a couple of hours; b) S-nanoparticles release fragments of DOX-BSA in presence of E-nanoparticles if magnetic field is ON while much less of low molecular mass fragments are observed if magnetic field is OFF; d) DOX-BSA is well preserved in S-nanoparticles as concluded from the control experiment with S-nanoparticles mixed with papain in solution.

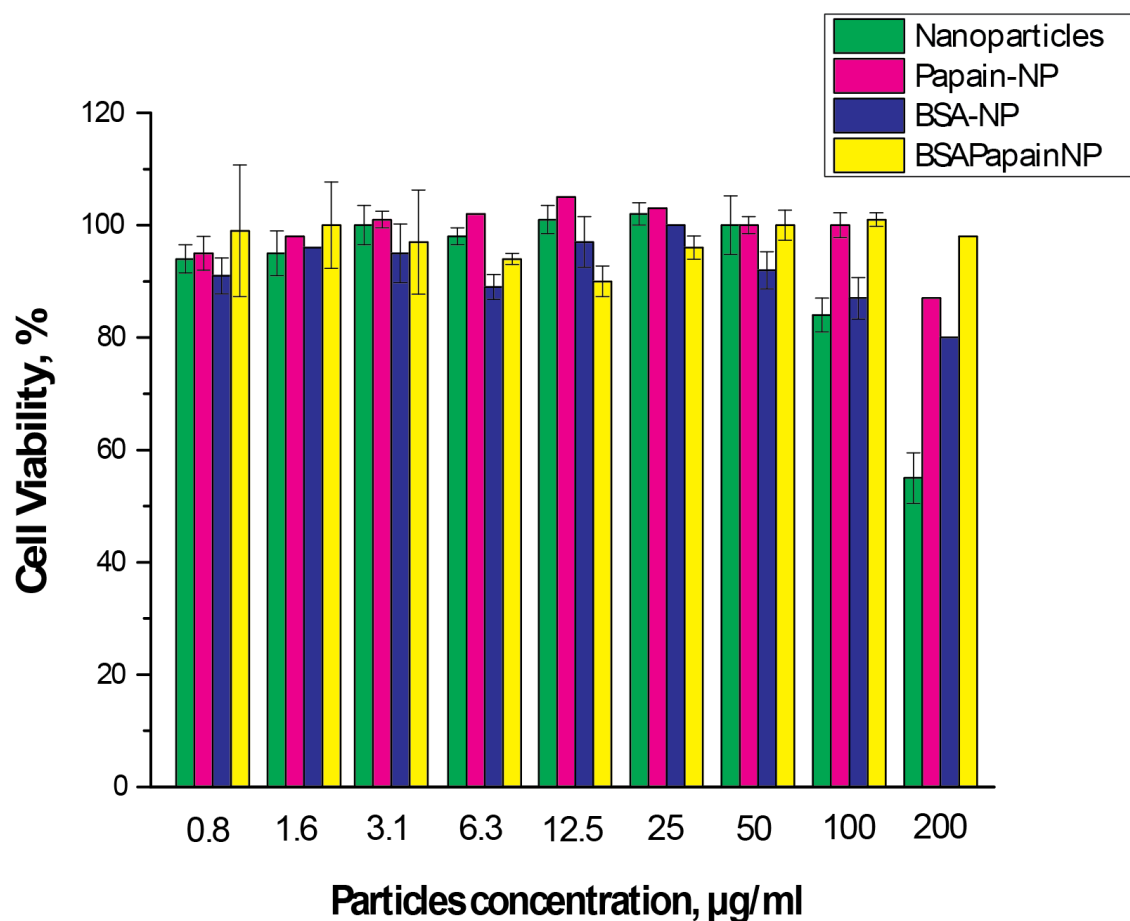
### **6.11 Spectroscopic estimation of loading and release of dox.**

Conjugation of DOX and BSA leads to changes of the molar extinction coefficient for absorbance at 495 nm and quantum yield of florescence emission (quenching). We have overcome the problem by using the following experiments.

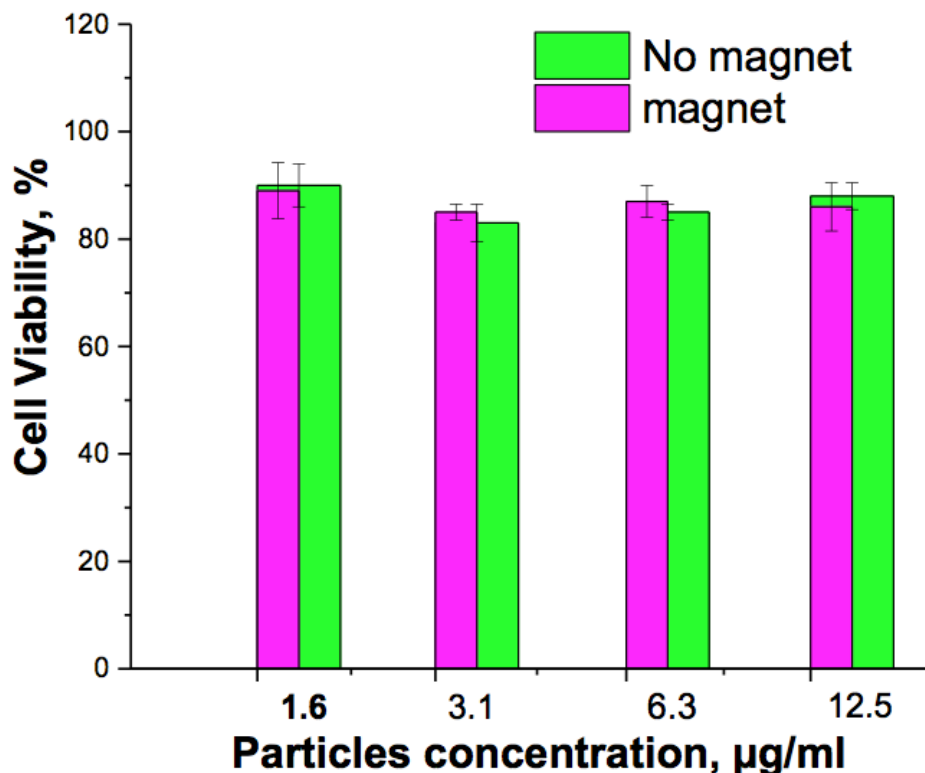
A DOX solution was prepared for conjugation as described above. Prior to conjugation, emission spectra were acquired. Upon the conjugation, the DOX-BSA emission spectrum was changed. Following the conjugation procedure, we have added papain and acquired spectra again. Upon proteolysis, the florescence spectra recovered (*Experimental Details* Figure 7). In this experiment, we proved that the degradation of the DOX-BSA conjugate into small fragments results in 95%

recovery of the spectrum and thus the spectrum obtained after magnetic release could be used for quantitative analysis. For example, similar reversible quenching of DOX was observed in the report by Farokhzad O.C. et al.<sup>161</sup>. The recovery of the spectra upon proteolysis was used for quantitative analysis of the DOX conjugation, DOX-BSA loading into S-nanoparticles, and DOX release upon application of the magnetic field to a mixture of S- and E-nanoparticles as schematically shown in *Experimental Details* Figure 8.

#### 6.12 Cell viability: reference experiments with no magnetic field applied



**Figure 6.18.** Cell viability. Reference experiments based on cell counts for cell cultures with added NPs:  $\text{Fe}_3\text{O}_4$  enveloped by  $\text{SiO}_2$  with no polymer shell (green), decorated with PAA-*b*-PPEGMA brush loaded with papain (red), decorated with PAA-*b*-PPEGMA brush loaded with FD-BSA (blue), decorated with PAA-*b*-PPEGMA brush loaded with FD-BSA and papain (no magnetic field). The error bars show the standard deviation obtained from three repetitive experiments.

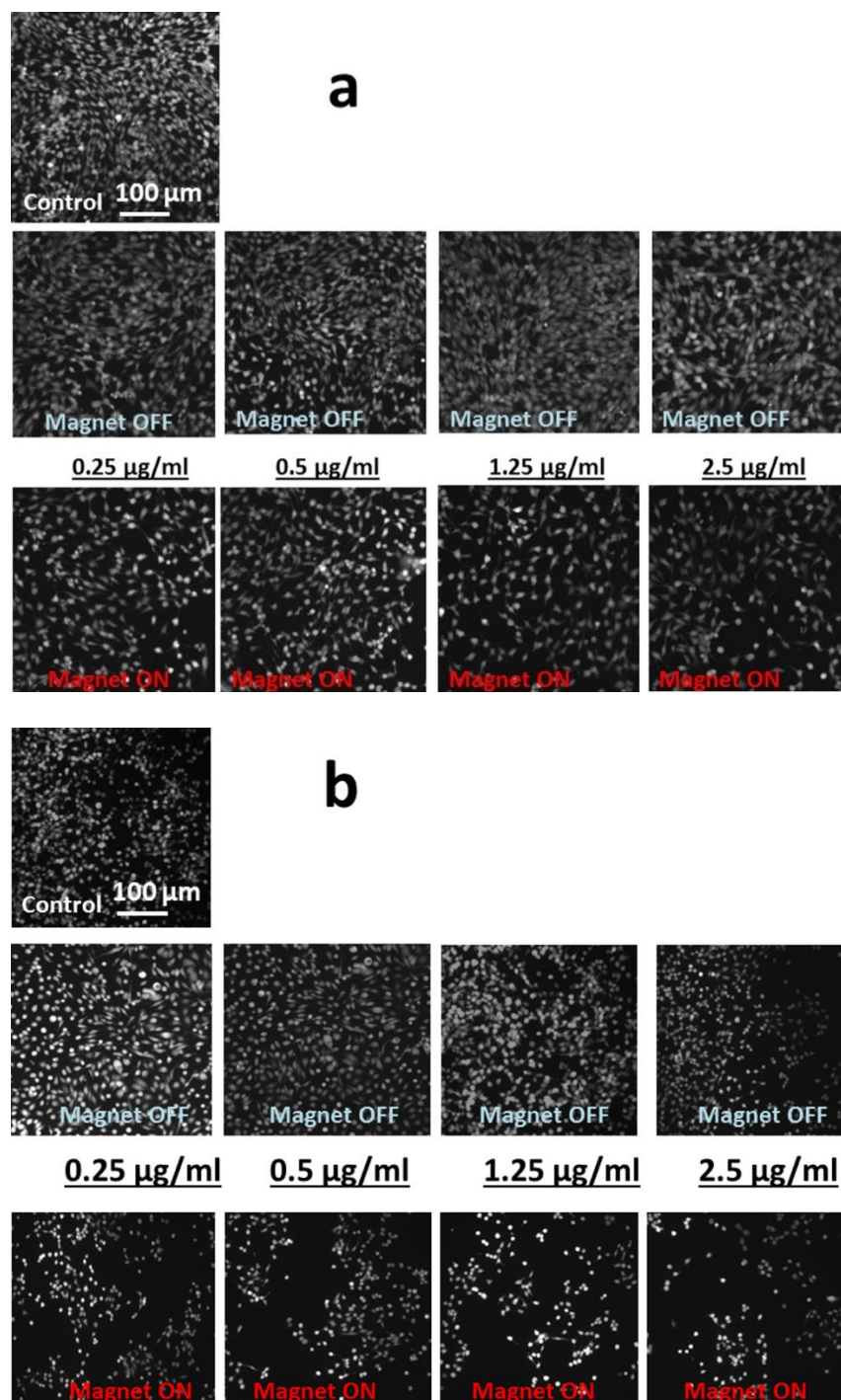


**Figure 6.19. Cell viability.** The reference experiments based on cell counts for cell cultures with added a 50:50 mixture of E- and S- nanoparticles (S-nanoparticles were loaded with FD-BSA with no conjugated DOX): no magnetic field applied (green bars) and with applied magnetic field (red bars) during the experiment. The error bars show the standard deviation obtained from three repetitive experiments.

The experimental methodology is the same as described in Methods. The results are shown in *Experimental Details* Figure 18. The NPs with no polymeric shell, and polymer brush decorated particles loaded with FD-BSA and papain with no magnetic field application demonstrate no obvious cytotoxicity at concentrations below 50  $\mu\text{g/ml}$ .

The results of a cell viability test for a 50:50 mixture of S-nanoparticles and E-nanoparticles, when the E-nanoparticles were loaded with FD-BSA only (no DOX conjugated) with magnetic field ON and OFF, are shown in *Experimental Details* Figure 19.





**Figure 6.17. Blocking cancer cell proliferation.** Representative images of two series of experiments (a and b) with 4T1 breast cancer cells incubated with a 1:1 mixture of S- and E-nanoparticles at different concentrations of NPs for 24 h with magnet OFF and ON vs control.



## **Instruments and Equipment**

Dynamic light scattering and zeta-potential measurements – Malvern Zetasizer Nano;

Atomic force microscopy (AFM) – Icon-PT from Bruker;

Ellipsometry – Nanofilm ep4 Null ellipsometer;

TEM – Philips FEI Tecnai20

Fluorescent microscope – Olympus IX83

Fluorescent spectrometer – Fluorolog-3 Research Spectrofluorometer, Horiba;

Microcalorimetry – Modular microcalorimetric systems TAM III, TA Instruments;

Confocal microscopy – Nikon U2000 confocal Eclipse C1 microscope

Viscotek Gel Permeation Chromatography with chloroform as the eluent at a flow rate of 1 ml/min.

## CHAPTER 7

### CONCLUSIONS

In this work, we used a combination of the synthesis of the composite nanoparticles with a superparamagnetic core, controlled radical polymerization for the modification of the nanoparticle surface and biocatalytic mechanism of drug release. This combination led to the development of the drug delivery system which is actuated remotely by application of magnetic field. It was found that a covalent attachment of the enzyme and substrate molecules to two corresponding populations of the polymer brush decorated nanoparticles does not block the biocatalytic degradation of the substrate in the specific conditions when the particles are merged together in an external force. At the same time, burying the enzyme and substrate in the polymer brush prevents their interaction between the substrate, enzyme and other biomolecules in the solution when the nanoparticles experience just Brownian motion. Such nanoparticle dispersion is stable while the brush architecture of the particle shell secures spatial separation of the reactive species. The catalytic reaction is triggered by magnetic field when the nanoparticles aggregate and the enzyme- and substrate-loaded brushes merge to form nanodomains of the catalytic reaction. We have demonstrated that our stimuli-responsive biocatalytic system is a powerful platform for novel biocatalytic processes. This biocatalytic platform possesses very important properties: (1) stimuli-triggered biocatalysis; (2) remote control of biocatalysis; and (3) high selectivity of biocatalysis when only authorized biocatalytic reactions are triggered. The developed system provides an example of a well-controlled magnetic-field-triggered anticancer

drug release. The proposed platform is a versatile tool capable of delivering various biological materials or therapeutic chemical molecules. It has promising potential for biotechnology and biomedical applications.

## CHAPTER 8

### FUTURE STUDIES

The developed system demonstrated efficient controlled release of model molecules and has a promising potential as a novel method for delivering poorly soluble or cytotoxic molecules.

Currently, there is an acute interest in conducting translational research of the system to test magnetically triggered release on mouse models to evaluate the efficiency of release in complex systems. Pharmacokinetic parameters should also be determined to understand nanoparticles accumulation, uptake, toxicity and clearance *in vivo*.

Based on the obtained results, magnetically-triggered enzymatic reactions in polymer brushes demonstrated high yield of the catalytic release and more studies are needed to understand the mechanism of enzyme-substrate interactions in the polymer brush. Previous experiments demonstrated enzymatic mobility in the polymer brush when adsorbed enzymes were labeled by fluorescent molecules. However, covalently bound enzymatic molecules will have restrictions in their diffusion and it is still unclear how the majority of the substrate is being digested.

Currently, there is an ongoing study to examine two theories of enzymatic catalysis in polymer brushes. The first assumption is that in an homogeneous magnetic field magnetic nanoparticles will undergo assembly into linear aggregates aligned with magnetic field lines. In these conditions, magnetic nanocarriers would not have conformational restrictions and could potentially undergo a dynamic behavior, e.g. rotation with increased probability of continuous enzyme-substrate interactions. Another theory, that is being evaluated, is that individual enzymes

conjugated to polymer brush molecules will have some degree of local displacement when polymer chains undergo conformational movements. Enzymatic molecules could be labeled by fluorescent molecules and time resolution spectroscopic measurements will be performed. To exclude the possible effect of nanoparticles rotation, polymer brush could be grafted onto solid surfaces, such as glass, and dynamic behavior of the fluorescent-labeled enzymes will be studied. Understanding of the mechanism of enzymatic catalysis inside the brush will help to maximize the loading of target molecules and improve system efficiency, reduce the toxicity of carriers and develop new applications.

## REFERENCES

- 1     Health, United States, 2016: With Chartbook on Long-term Trends in Health. . (National Center for Health Statistics. Hyattsville, MD. 2017, 2017).
- 2     Reddy, L. H., Arias, J. L., Nicolas, J. & Couvreur, P. Magnetic Nanoparticles: Design and Characterization, Toxicity and Biocompatibility, Pharmaceutical and Biomedical Applications. *Chemical Reviews* **112**, 5818-5878, doi:10.1021/cr300068p (2012).
- 3     Bakshi, S. F. *et al.* Nanoreactors based on DNAzyme-functionalized magnetic nanoparticles activated by magnetic field. *Nanoscale*, doi:10.1039/C7NR08581H (2018).
- 4     Wu, W., Wu, Z., Yu, T., Jiang, C. & Kim, W.-S. Recent progress on magnetic iron oxide nanoparticles: synthesis, surface functional strategies and biomedical applications. *Science and Technology of Advanced Materials* **16**, 023501, doi:10.1088/1468-6996/16/2/023501 (2015).
- 5     Zhao, X. *et al.* Pollen magnetofection for genetic modification with magnetic nanoparticles as gene carriers. *Nature Plants* **3**, 956-964, doi:10.1038/s41477-017-0063-z (2017).
- 6     Wang, P., Lombi, E., Zhao, F.-J. & Kopittke, P. M. Nanotechnology: A New Opportunity in Plant Sciences. *Trends in Plant Science* **21**, 699-712, doi:10.1016/j.tplants.2016.04.005.

- 7 Lee, J.-H., Kim, J.-w. & Cheon, J. Magnetic Nanoparticles for Multi-Imaging and Drug Delivery. *Molecules and Cells* **35**, 274-284, doi:10.1007/s10059-013-0103-0 (2013).
- 8 Gao, Y., Lim, J., Teoh, S.-H. & Xu, C. Emerging translational research on magnetic nanoparticles for regenerative medicine. *Chemical Society Reviews* **44**, 6306-6329, doi:10.1039/C4CS00322E (2015).
- 9 Latorre, M. & Rinaldi, C. Applications of magnetic nanoparticles in medicine: magnetic fluid hyperthermia. *Puerto Rico health sciences journal* **28**, 227-238 (2009).
- 10 Babu, A., K Templeton, A., Munshi, A. & Ramesh, R. *Nanodrug Delivery Systems: A Promising Technology for Detection, Diagnosis, and Treatment of Cancer*. Vol. 15 (2014).
- 11 Gao, Y. *et al.* Nanotechnology-based intelligent drug design for cancer metastasis treatment. *Biotechnology Advances* **32**, 761-777, doi:<https://doi.org/10.1016/j.biotechadv.2013.10.013> (2014).
- 12 Kudr, J. *et al.* Magnetic Nanoparticles: From Design and Synthesis to Real World Applications. *Nanomaterials* **7**, 243, doi:10.3390/nano7090243 (2017).
- 13 Lu, A. H., Salabas, E. L. & Schüth, F. Magnetic Nanoparticles: Synthesis, Protection, Functionalization, and Application. *Angewandte Chemie International Edition* **46**, 1222-1244, doi:doi:10.1002/anie.200602866 (2007).
- 14 Uthaman, S., Lee, S. J., Cherukula, K., Cho, C.-S. & Park, I.-K. Polysaccharide-Coated Magnetic Nanoparticles for Imaging and Gene Therapy. *BioMed Research International* **2015**, 14, doi:10.1155/2015/959175 (2015).

- 15 Veisesh, O., Gunn, J. W. & Zhang, M. Design and fabrication of magnetic nanoparticles for targeted drug delivery and imaging. *Advanced Drug Delivery Reviews* **62**, 284-304, doi:<https://doi.org/10.1016/j.addr.2009.11.002> (2010).
- 16 Siegwart, D. J., Oh, J. K. & Matyjaszewski, K. ATRP in the design of functional materials for biomedical applications. *Progress in polymer science* **37**, 18-37, doi:10.1016/j.progpolymsci.2011.08.001 (2012).
- 17 Zhu, W., Zhong, M., Li, W., Dong, H. & Matyjaszewski, K. Clickable Stars by Combination of AROP and Aqueous AGET ATRP. *Macromolecules* **44**, 1920-1926, doi:10.1021/ma102704g (2011).
- 18 in *Magnetic Nanoparticles*.
- 19 Moise, S. *et al.* The cellular magnetic response and biocompatibility of biogenic zinc- and cobalt-doped magnetite nanoparticles. *Scientific Reports* **7**, 39922, doi:10.1038/srep39922 (2017).
- 20 Amiri, S. & Shokrollahi, H. The role of cobalt ferrite magnetic nanoparticles in medical science. *Materials Science and Engineering: C* **33**, 1-8, doi:<https://doi.org/10.1016/j.msec.2012.09.003> (2013).
- 21 Pankhurst, Q. A., Connolly, J., Jones, S. K. & Dobson, J. Applications of magnetic nanoparticles in biomedicine. *Journal of Physics D: Applied Physics* **36**, R167 (2003).
- 22 in *The Physical Principles of Magnetism*.
- 23 Brown, W. F. Thermal Fluctuations of a Single-Domain Particle. *Physical Review* **130**, 1677-1686 (1963).
- 24 Mody Vicky, V., Singh, A. & Wesley, B. in *European Journal of Nanomedicine* Vol. 5 11 (2013).



- 25 Fatima, H. & Kim, K.-S. Magnetic nanoparticles for bioseparation. *Korean Journal of Chemical Engineering* **34**, 589-599, doi:10.1007/s11814-016-0349-2 (2017).
- 26 Xu, H. *et al.* Antibody Conjugated Magnetic Iron Oxide Nanoparticles for Cancer Cell Separation in Fresh Whole Blood. *Biomaterials* **32**, 9758-9765, doi:10.1016/j.biomaterials.2011.08.076 (2011).
- 27 Haddad, Y. *et al.* The Isolation of DNA by Polycharged Magnetic Particles: An Analysis of the Interaction by Zeta Potential and Particle Size. *International Journal of Molecular Sciences* **17**, 550, doi:10.3390/ijms17040550 (2016).
- 28 Shahbazi-Gahrouei, D. *et al.* Functionalized Magnetic Nanoparticles for the Detection and Quantitative Analysis of Cell Surface Antigen. *BioMed Research International* **2013**, 349408, doi:10.1155/2013/349408 (2013).
- 29 Hobson, D. W. Commercialization of nanotechnology. *Wiley Interdisciplinary Reviews: Nanomedicine and Nanobiotechnology* **1**, 189-202, doi:doi:10.1002/wnan.28 (2009).
- 30 Hoshyar, N., Gray, S., Han, H. & Bao, G. The effect of nanoparticle size on in vivo pharmacokinetics and cellular interaction. *Nanomedicine* **11**, 673-692, doi:10.2217/nnm.16.5 (2016).
- 31 Liu, L. *et al.* Decreased reticuloendothelial system clearance and increased blood half-life and immune cell labeling for nano- and micron-sized superparamagnetic iron-oxide particles upon pre-treatment with Intralipid. *Biochimica et biophysica acta* **1830**, 3447-3453, doi:10.1016/j.bbagen.2013.01.021 (2013).
- 32 Stephen, Z. R., Kievit, F. M. & Zhang, M. Magnetite Nanoparticles for Medical MR Imaging. *Materials today (Kidlington, England)* **14**, 330-338, doi:10.1016/S1369-7021(11)70163-8 (2011).

- 33 Zheng, S. W. *et al.* RGD-conjugated iron oxide magnetic nanoparticles for magnetic resonance imaging contrast enhancement and hyperthermia. *Journal of biomaterials applications* **28**, 1051-1059, doi:10.1177/0885328213493486 (2014).
- 34 Tefft, B. J. *et al.* Cell Labeling and Targeting with Superparamagnetic Iron Oxide Nanoparticles. *Journal of Visualized Experiments : JoVE*, 53099, doi:10.3791/53099 (2015).
- 35 Kolosnjaj-Tabi, J., Wilhelm, C., Clément, O. & Gazeau, F. Cell labeling with magnetic nanoparticles: Opportunity for magnetic cell imaging and cell manipulation. *Journal of Nanobiotechnology* **11**, S7-S7, doi:10.1186/1477-3155-11-S1-S7 (2013).
- 36 Kami, D. *et al.* Application of Magnetic Nanoparticles to Gene Delivery. *International Journal of Molecular Sciences* **12**, 3705-3722, doi:10.3390/ijms12063705 (2011).
- 37 Sandre, O. *et al.* In Vivo Imaging of Local Gene Expression Induced by Magnetic Hyperthermia. *Genes* **8**, 61, doi:10.3390/genes8020061 (2017).
- 38 Guardia, P., Pérez, N., Labarta, A. & Batlle, X. Controlled Synthesis of Iron Oxide Nanoparticles over a Wide Size Range. *Langmuir* **26**, 5843-5847, doi:10.1021/la903767e (2010).
- 39 Tancredi, P., Botasini, S., Moscoso-Londoño, O., Méndez, E. & Socolovsky, L. Polymer-assisted size control of water-dispersible iron oxide nanoparticles in range between 15 and 100nm. *Colloids and Surfaces A: Physicochemical and Engineering Aspects* **464**, 46-51, doi:<https://doi.org/10.1016/j.colsurfa.2014.10.001> (2015).
- 40 Kekalo, K., Koo, K., Zeitchick, E. & Baker, I. Microemulsion Synthesis of Iron Core/Iron Oxide Shell Magnetic Nanoparticles and Their Physicochemical Properties.

- Materials Research Society symposia proceedings. Materials Research Society* **1416**, 10.1557/opl.2012.1736 (2012).
- 41 Sugimoto, T. & Matijević, E. Formation of uniform spherical magnetite particles by crystallization from ferrous hydroxide gels. *Journal of Colloid and Interface Science* **74**, 227-243, doi:[https://doi.org/10.1016/0021-9797\(80\)90187-3](https://doi.org/10.1016/0021-9797(80)90187-3) (1980).
- 42 Bumb, A. *et al.* Synthesis and characterization of ultra-small superparamagnetic iron oxide nanoparticles thinly coated with silica. *Nanotechnology* **19**, 335601-335601, doi:10.1088/0957-4484/19/33/335601 (2008).
- 43 Unni, M. *et al.* Thermal Decomposition Synthesis of Iron Oxide Nanoparticles with Diminished Magnetic Dead Layer by Controlled Addition of Oxygen. *ACS Nano* **11**, 2284-2303, doi:10.1021/acsnano.7b00609 (2017).
- 44 Thanh, N. T. K., Maclean, N. & Mahiddine, S. Mechanisms of Nucleation and Growth of Nanoparticles in Solution. *Chemical Reviews* **114**, 7610-7630, doi:10.1021/cr400544s (2014).
- 45 MAITY, D., DING, J. & XUE, J.-M. SYNTHESIS OF MAGNETITE NANOPARTICLES BY THERMAL DECOMPOSITION: TIME, TEMPERATURE, SURFACTANT AND SOLVENT EFFECTS. *Functional Materials Letters* **01**, 189-193, doi:10.1142/s1793604708000381 (2008).
- 46 Daou, T. J. *et al.* Hydrothermal Synthesis of Monodisperse Magnetite Nanoparticles. *Chemistry of Materials* **18**, 4399-4404, doi:10.1021/cm060805r (2006).
- 47 Malumbres, A. *et al.* Continuous production of iron-based nanocrystals by laser pyrolysis. Effect of operating variables on size, composition and magnetic response. *Nanotechnology* **24**, 325603 (2013).

- 48 Norma, L. M., Dora, L. F. & Gustavo, A. H. Magnetic-luminescent spherical particles synthesized by ultrasonic spray pyrolysis. *Materials Research Express* **2**, 076103 (2015).
- 49 Cabrera, L., Gutierrez, S., Menendez, N., Morales, M. P. & Herrasti, P. Magnetite nanoparticles: Electrochemical synthesis and characterization. *Electrochimica Acta* **53**, 3436-3441, doi:<https://doi.org/10.1016/j.electacta.2007.12.006> (2008).
- 50 Polte, J. *et al.* Mechanism of Gold Nanoparticle Formation in the Classical Citrate Synthesis Method Derived from Coupled In Situ XANES and SAXS Evaluation. *Journal of the American Chemical Society* **132**, 1296-1301, doi:10.1021/ja906506j (2010).
- 51 Bigall, N. C. & Eychmüller, A. Synthesis of noble metal nanoparticles and their non-ordered superstructures. *Philosophical Transactions of the Royal Society A: Mathematical, Physical and Engineering Sciences* **368**, 1385-1404, doi:10.1098/rsta.2009.0274 (2010).
- 52 Wang, Z., Lam, A. & Acosta, E. Suspensions of Iron Oxide Nanoparticles Stabilized by Anionic Surfactants. *Journal of Surfactants and Detergents* **16**, 397-407, doi:10.1007/s11743-012-1425-1 (2013).
- 53 Choi, Y. W., Lee, H., Song, Y. & Sohn, D. Colloidal stability of iron oxide nanoparticles with multivalent polymer surfactants. *Journal of colloid and interface science* **443**, 8-12, doi:10.1016/j.jcis.2014.11.068 (2015).
- 54 Sara, M., Carmelo, D., Anna, M. F., Alessandra, P. & Alessandro, P. Colloidal stability of iron oxide nanocrystals coated with a PEG-based tetra-catechol surfactant. *Nanotechnology* **24**, 105702 (2013).

- 55 Rovira-Bru, M., Thompson, D. H. & Szleifer, I. Size and Structure of Spontaneously Forming Liposomes in Lipid/PEG-Lipid Mixtures. *Biophysical Journal* **83**, 2419-2439, doi:[https://doi.org/10.1016/S0006-3495\(02\)75255-7](https://doi.org/10.1016/S0006-3495(02)75255-7) (2002).
- 56 Ditsch, A., Laibinis, P. E., Wang, D. I. C. & Hatton, T. A. Controlled Clustering and Enhanced Stability of Polymer-Coated Magnetic Nanoparticles. *Langmuir* **21**, 6006-6018, doi:10.1021/la047057+ (2005).
- 57 Boyer, C., Whittaker, M. R., Bulmus, V., Liu, J. & Davis, T. P. The design and utility of polymer-stabilized iron-oxide nanoparticles for nanomedicine applications. *Npg Asia Materials* **2**, 23, doi:10.1038/asiamat.2010.6 (2010).
- 58 Hegazy, M. *et al.* Construction of polymer coated core-shell magnetic mesoporous silica nanoparticles with triple responsive drug delivery. *Polymer Chemistry* **8**, 5852-5864, doi:10.1039/C7PY01179B (2017).
- 59 Stöber, W., Fink, A. & Bohn, E. Controlled growth of monodisperse silica spheres in the micron size range. *Journal of Colloid and Interface Science* **26**, 62-69, doi:[https://doi.org/10.1016/0021-9797\(68\)90272-5](https://doi.org/10.1016/0021-9797(68)90272-5) (1968).
- 60 Deng, Y.-H., Wang, C.-C., Hu, J.-H., Yang, W.-L. & Fu, S.-K. Investigation of formation of silica-coated magnetite nanoparticles via sol-gel approach. *Colloids and Surfaces A: Physicochemical and Engineering Aspects* **262**, 87-93, doi:<https://doi.org/10.1016/j.colsurfa.2005.04.009> (2005).
- 61 Abbas, M. *et al.* Highly stable- silica encapsulating magnetite nanoparticles (Fe<sub>3</sub>O<sub>4</sub>/SiO<sub>2</sub>) synthesized using single surfactantless- polyol process. *Ceramics International* **40**, 1379-1385, doi:<https://doi.org/10.1016/j.ceramint.2013.07.019> (2014).

- 62 Luke, G. P. *et al.* Silica-coated gold nanoplates as stable photoacoustic contrast agents for sentinel lymph node imaging. *Nanotechnology* **24**, 455101, doi:10.1088/0957-4484/24/45/455101 (2013).
- 63 Jiaqi, W., Xiangxi, M., Enzhong, L. & Kezheng, C. Incorporation of magnetite nanoparticle clusters in fluorescent silica nanoparticles for high-performance brain tumor delineation. *Nanotechnology* **21**, 235104 (2010).
- 64 Viswanathan, K. Preparation and characterization of fluorescent silica coated magnetic hybrid nanoparticles. *Colloids and Surfaces A: Physicochemical and Engineering Aspects* **386**, 11-15, doi:<https://doi.org/10.1016/j.colsurfa.2011.06.017> (2011).
- 65 Park, K., Choi, D. & Hong, J. Nanostructured Polymer Thin Films Fabricated with Brush-based Layer-by-Layer Self-assembly for Site-selective Construction and Drug release. *Scientific Reports* **8**, 3365, doi:10.1038/s41598-018-21493-9 (2018).
- 66 Minko, S. in *Polymer Surfaces and Interfaces: Characterization, Modification and Applications* (ed Manfred Stamm) 215-234 (Springer Berlin Heidelberg, 2008).
- 67 Alvarez, N. J., Anna, S. L., Saigal, T., Tilton, R. D. & Walker, L. M. Interfacial Dynamics and Rheology of Polymer-Grafted Nanoparticles at Air–Water and Xylene–Water Interfaces. *Langmuir* **28**, 8052-8063, doi:10.1021/la300737p (2012).
- 68 Ionov, L. & Minko, S. Mixed Polymer Brushes with Locking Switching. *ACS Applied Materials & Interfaces* **4**, 483-489, doi:10.1021/am201736t (2012).
- 69 Motornov, M., Roiter, Y., Tokarev, I. & Minko, S. Stimuli-responsive nanoparticles, nanogels and capsules for integrated multifunctional intelligent systems. *Progress in Polymer Science* **35**, 174-211, doi:<https://doi.org/10.1016/j.progpolymsci.2009.10.004> (2010).

- 70 Sidorenko, A., Minko, S., Schenk-Meuser, K., Duschner, H. & Stamm, M. Switching of Polymer Brushes. *Langmuir* **15**, 8349-8355, doi:10.1021/la990869z (1999).
- 71 Minko, S. Responsive polymer brushes. *Polym Rev* **46**, 397-420, doi:10.1080/15583720600945402 (2006).
- 72 Motornov, M. *et al.* Stimuli-Responsive Colloidal Systems from Mixed Brush-Coated Nanoparticles. *Advanced Functional Materials* **17**, 2307-2314, doi:doi:10.1002/adfm.200600934 (2007).
- 73 Hackett, A. J. *et al.* Conductive surfaces with dynamic switching in response to temperature and salt. *Journal of Materials Chemistry B* **3**, 9285-9294, doi:10.1039/C5TB02125A (2015).
- 74 Delcroix, M. F., Laurent, S., Huet, G. L. & Dupont-Gillain, C. C. Protein adsorption can be reversibly switched on and off on mixed PEO/PAA brushes. *Acta Biomaterialia* **11**, 68-79, doi:<https://doi.org/10.1016/j.actbio.2014.09.010> (2015).
- 75 Stuart, M. A. C. *et al.* Emerging applications of stimuli-responsive polymer materials. *Nature Materials* **9**, 101, doi:10.1038/nmat2614 (2010).
- 76 Zdyrko, B. & Luzinov, I. Polymer Brushes by the “Grafting to” Method. *Macromolecular Rapid Communications* **32**, 859-869, doi:doi:10.1002/marc.201100162 (2011).
- 77 Lopez-Cruz, A., Barrera, C., Calero-DdelC, V. L. & Rinaldi, C. Water dispersible iron oxide nanoparticles coated with covalently linked chitosan. *Journal of Materials Chemistry* **19**, 6870-6876, doi:10.1039/B908777J (2009).

- 78 De Palma, R. *et al.* Silane Ligand Exchange to Make Hydrophobic Superparamagnetic Nanoparticles Water-Dispersible. *Chemistry of Materials* **19**, 1821-1831, doi:10.1021/cm0628000 (2007).
- 79 Pyun, J., Kowalewski, T. & Matyjaszewski, K. Synthesis of Polymer Brushes Using Atom Transfer Radical Polymerization. *Macromolecular Rapid Communications* **24**, 1043-1059, doi:doi:10.1002/marc.200300078 (2003).
- 80 Minko, S. *et al.* Radical Polymerization Initiated from a Solid Substrate. 2. Study of the Grafting Layer Growth on the Silica Surface by in situ Ellipsometry. *Macromolecules* **32**, 4532-4538, doi:10.1021/ma9813542 (1999).
- 81 Minko, S. S., Luzinov, I. A., Evchuk, I. Y. & Voronov, S. A. Synthesis and behaviour of the polymer covering on a solid surface: 1. Attachment of the polymer initiator to the solid surface. *Polymer* **37**, 177-181, doi:[https://doi.org/10.1016/0032-3861\(96\)81613-2](https://doi.org/10.1016/0032-3861(96)81613-2) (1996).
- 82 Pyun, J., Jia, S., Kowalewski, T., Patterson, G. D. & Matyjaszewski, K. Synthesis and Characterization of Organic/Inorganic Hybrid Nanoparticles: Kinetics of Surface-Initiated Atom Transfer Radical Polymerization and Morphology of Hybrid Nanoparticle Ultrathin Films. *Macromolecules* **36**, 5094-5104, doi:10.1021/ma034188t (2003).
- 83 von Werne, T. A. *et al.* A Versatile Method for Tuning the Chemistry and Size of Nanoscopic Features by Living Free Radical Polymerization. *Journal of the American Chemical Society* **125**, 3831-3838, doi:10.1021/ja028866n (2003).
- 84 Higaki, Y., Kobayashi, M., Hirai, T. & Takahara, A. Direct polymer brush grafting to polymer fibers and films by surface-initiated polymerization. *Polymer Journal* **50**, 101, doi:10.1038/pj.2017.61 (2017).



- 85 Tsarevsky, N. V., Bernaerts, K. V., Dufour, B., Du Prez, F. E. & Matyjaszewski, K. Well-Defined (Co)polymers with 5-Vinyltetrazole Units via Combination of Atom Transfer Radical (Co)polymerization of Acrylonitrile and “Click Chemistry”-Type Postpolymerization Modification. *Macromolecules* **37**, 9308-9313, doi:10.1021/ma048207q (2004).
- 86 Coca, S., Jasieczek, C. B., Beers, K. L. & Matyjaszewski, K. Polymerization of acrylates by atom transfer radical polymerization. Homopolymerization of 2-hydroxyethyl acrylate. *Journal of Polymer Science Part A: Polymer Chemistry* **36**, 1417-1424, doi:doi:10.1002/(SICI)1099-0518(19980715)36:9<1417::AID-POLA9>3.0.CO;2-P (1998).
- 87 Wang, X. S., F. Lascelles, S., A. Jackson, R. & P. Armes, S. Facile synthesis of well-defined water-soluble polymers via atom transfer radical polymerization in aqueous media at ambient temperature. *Chemical Communications*, 1817-1818, doi:10.1039/A904691G (1999).
- 88 Ouchi, M., Yoda, H., Terashima, T. & Sawamoto, M. Aqueous metal-catalyzed living radical polymerization: highly active water-assisted catalysis. *Polymer Journal* **44**, 51, doi:10.1038/pj.2011.59 [https://www.nature.com/articles/pj201159 - supplementary-information](https://www.nature.com/articles/pj201159-supplementary-information) (2011).
- 89 de Vos, W. M., Biesheuvel, P. M., de Keizer, A., Kleijn, J. M. & Cohen Stuart, M. A. Adsorption of the Protein Bovine Serum Albumin in a Planar Poly(acrylic acid) Brush Layer As Measured by Optical Reflectometry. *Langmuir* **24**, 6575-6584, doi:10.1021/la8006469 (2008).

- 90 Psarra, E. *et al.* Nanostructured Biointerfaces: Nanoarchitectonics of Thermoresponsive Polymer Brushes Impact Protein Adsorption and Cell Adhesion. *ACS Applied Materials & Interfaces* **7**, 12516-12529, doi:10.1021/am508161q (2015).
- 91 Reichhart, C. & Czeslik, C. Native-like Structure of Proteins at a Planar Poly(acrylic acid) Brush. *Langmuir* **25**, 1047-1053, doi:10.1021/la802905s (2009).
- 92 Trotsenko, O., Roiter, Y. & Minko, S. Structure of salted and discharged globules of hydrophobic polyelectrolytes adsorbed from aqueous solutions. *Journal of Polymer Science Part B: Polymer Physics* **48**, 1623-1627, doi:doi:10.1002/polb.21970 (2010).
- 93 Trotsenko, O., Roiter, Y. & Minko, S. Conformational Transitions of Flexible Hydrophobic Polyelectrolytes in Solutions of Monovalent and Multivalent Salts and Their Mixtures. *Langmuir* **28**, 6037-6044, doi:10.1021/la300584k (2012).
- 94 Chen, S., Li, L., Zhao, C. & Zheng, J. Surface hydration: Principles and applications toward low-fouling/nonfouling biomaterials. *Polymer* **51**, 5283-5293, doi:<https://doi.org/10.1016/j.polymer.2010.08.022> (2010).
- 95 Nalam, P. C. *et al.* Nanomechanics of pH-Responsive, Drug-Loaded, Bilayered Polymer Grafts. *ACS Applied Materials & Interfaces* **9**, 12936-12948, doi:10.1021/acsami.6b14116 (2017).
- 96 Eisenberg, J. L., Piper, J. L. & Mrksich, M. Using Self-Assembled Monolayers to Model Cell Adhesion to the 9th and 10th Type III Domains of Fibronectin. *Langmuir* **25**, 13942-13951, doi:10.1021/la901528c (2009).
- 97 Navarro, M., Benetti, E. M., Zapotoczny, S., Planell, J. A. & Vancso, G. J. Buried, Covalently Attached RGD Peptide Motifs in Poly(methacrylic acid) Brush Layers: The

- Effect of Brush Structure on Cell Adhesion. *Langmuir* **24**, 10996-11002, doi:10.1021/la800999y (2008).
- 98 Harris, B. P. *et al.* Photopatterned Polymer Brushes Promoting Cell Adhesion Gradients. *Langmuir* **22**, 4467-4471, doi:10.1021/la053417x (2006).
- 99 Takahashi, H. *et al.* Terminally Functionalized Thermoresponsive Polymer Brushes for Simultaneously Promoting Cell Adhesion and Cell Sheet Harvest. *Biomacromolecules* **13**, 253-260, doi:10.1021/bm201545u (2012).
- 100 Masuda, S., Shimizu, T., Yamato, M. & Okano, T. Cell sheet engineering for heart tissue repair. *Advanced Drug Delivery Reviews* **60**, 277-285, doi:<https://doi.org/10.1016/j.addr.2007.08.031> (2008).
- 101 Goddard, J.-P. & Reymond, J.-L. Recent advances in enzyme assays. *Trends in Biotechnology* **22**, 363-370, doi:10.1016/j.tibtech.2004.04.005.
- 102 Bhat, M. K. Cellulases and related enzymes in biotechnology. *Biotechnol Adv* **18**, 355-383 (2000).
- 103 Yonghua, L. & Ian, R. H. Treating Cotton with Cellulases and Pectinases: Effects on Cuticle and Fiber Properties. *Textile Research Journal* **68**, 671-679, doi:10.1177/004051759806800908 (1998).
- 104 You-Lo, H. & Ian, R. H. Effects of Selected Inorganic Salts on Cotton Flammability: Part I: Untreated Cotton in the Vertical Test and Oxygen Index Test. *Textile Research Journal* **54**, 171-179, doi:10.1177/004051758405400306 (1984).
- 105 Vellard, M. The enzyme as drug: application of enzymes as pharmaceuticals. *Current opinion in biotechnology* **14**, 444-450 (2003).

- 106 Sanchez, S. & Demain, A. L. Enzymes and Bioconversions of Industrial, Pharmaceutical, and Biotechnological Significance. *Organic Process Research & Development* **15**, 224-230, doi:10.1021/op100302x (2011).
- 107 Czeslik, C., Jackler, G., Steitz, R. & von Grünberg, H.-H. Protein Binding to Like-Charged Polyelectrolyte Brushes by Counterion Evaporation. *The Journal of Physical Chemistry B* **108**, 13395-13402, doi:10.1021/jp0488766 (2004).
- 108 Wittemann, A. & Ballauff, M. Interaction of proteins with linear polyelectrolytes and spherical polyelectrolyte brushes in aqueous solution. *Physical Chemistry Chemical Physics* **8**, 5269-5275, doi:10.1039/B609879G (2006).
- 109 Haupt, B., Neumann, T., Wittemann, A. & Ballauff, M. Activity of Enzymes Immobilized in Colloidal Spherical Polyelectrolyte Brushes. *Biomacromolecules* **6**, 948-955, doi:10.1021/bm0493584 (2005).
- 110 Wittemann, A. & Ballauff, M. Secondary Structure Analysis of Proteins Embedded in Spherical Polyelectrolyte Brushes by FT-IR Spectroscopy. *Analytical Chemistry* **76**, 2813-2819, doi:10.1021/ac0354692 (2004).
- 111 Kudina, O. *et al.* Highly Efficient Phase Boundary Biocatalysis with Enzymogel Nanoparticles. *Angewandte Chemie International Edition* **53**, 483-487, doi:10.1002/anie.201306831 (2014).
- 112 Allen, T. M. & Cullis, P. R. Liposomal drug delivery systems: From concept to clinical applications. *Advanced Drug Delivery Reviews* **65**, 36-48, doi:<https://doi.org/10.1016/j.addr.2012.09.037> (2013).

- 113 Zylberberg, C. & Matosevic, S. Pharmaceutical liposomal drug delivery: a review of new delivery systems and a look at the regulatory landscape. *Drug delivery* **23**, 3319-3329, doi:10.1080/10717544.2016.1177136 (2016).
- 114 Li, J. & Mooney, D. J. Designing hydrogels for controlled drug delivery. *Nature Reviews Materials* **1**, 16071, doi:10.1038/natrevmats.2016.71 <https://www.nature.com/articles/natrevmats201671-supplementary-information> (2016).
- 115 Northfelt, D. W. *et al.* Doxorubicin encapsulated in liposomes containing surface-bound polyethylene glycol: pharmacokinetics, tumor localization, and safety in patients with AIDS-related Kaposi's sarcoma. *Journal of clinical pharmacology* **36**, 55-63 (1996).
- 116 Maeda, H. & Matsumura, Y. Tumoritropic and lymphotropic principles of macromolecular drugs. *Critical reviews in therapeutic drug carrier systems* **6**, 193-210 (1989).
- 117 Matsumura, Y. & Maeda, H. A new concept for macromolecular therapeutics in cancer chemotherapy: mechanism of tumoritropic accumulation of proteins and the antitumor agent smancs. *Cancer research* **46**, 6387-6392 (1986).
- 118 Deatsch, A. E. & Evans, B. A. Heating efficiency in magnetic nanoparticle hyperthermia. *Journal of Magnetism and Magnetic Materials* **354**, 163-172, doi:<https://doi.org/10.1016/j.jmmm.2013.11.006> (2014).
- 119 Revia, R. A. & Zhang, M. Magnetite nanoparticles for cancer diagnosis, treatment, and treatment monitoring: recent advances. *Materials Today* **19**, 157-168, doi:<https://doi.org/10.1016/j.mattod.2015.08.022> (2016).

- 120 Mallidi, S. *et al.* Visualization of molecular composition and functionality of cancer cells using nanoparticle-augmented ultrasound-guided photoacoustics. *Photoacoustics* **3**, 26-34, doi:10.1016/j.pacs.2014.12.003 (2015).
- 121 Li, S.-D. & Huang, L. Stealth Nanoparticles: High Density but Sheddable PEG is a Key for Tumor Targeting. *Journal of controlled release : official journal of the Controlled Release Society* **145**, 178-181, doi:10.1016/j.jconrel.2010.03.016 (2010).
- 122 Kievit, F. M. *et al.* PEI-PEG-Chitosan Copolymer Coated Iron Oxide Nanoparticles for Safe Gene Delivery: synthesis, complexation, and transfection. *Adv Funct Mater* **19**, 2244-2251, doi:10.1002/adfm.200801844 (2009).
- 123 Thomas, C. R. *et al.* Noninvasive Remote-Controlled Release of Drug Molecules in Vitro Using Magnetic Actuation of Mechanized Nanoparticles. *Journal of the American Chemical Society* **132**, 10623-10625, doi:10.1021/ja1022267 (2010).
- 124 Louguet, S. *et al.* Thermoresponsive polymer brush-functionalized magnetic manganite nanoparticles for remotely triggered drug release. *Polymer Chemistry* **3**, 1408-1417, doi:10.1039/C2PY20089A (2012).
- 125 Oliveira, H. *et al.* Magnetic field triggered drug release from polymersomes for cancer therapeutics. *J Control Release* **169**, 165-170, doi:10.1016/j.jconrel.2013.01.013 (2013).
- 126 Gao, W., Chan, J. M. & Farokhzad, O. C. pH-Responsive Nanoparticles for Drug Delivery. *Molecular Pharmaceutics* **7**, 1913-1920, doi:10.1021/mp100253e (2010).
- 127 Zhang, X. *et al.* pH-Triggered Doxorubicin Delivery Based on Hollow Nanoporous Silica Nanoparticles with Free-Standing Superparamagnetic Fe<sub>3</sub>O<sub>4</sub> Cores. *The Journal of Physical Chemistry C* **115**, 1436-1443, doi:10.1021/jp1075498 (2011).

- 128 Isojima, T., Lattuada, M., Vander Sande, J. B. & Hatton, T. A. Reversible Clustering of pH- and Temperature-Responsive Janus Magnetic Nanoparticles. *ACS Nano* **2**, 1799-1806, doi:10.1021/nn800089z (2008).
- 129 Boyes, S. G., Akgun, B., Brittain, W. J. & Foster, M. D. Synthesis, characterization, and properties of polyelectrolyte block copolymer brushes prepared by atom transfer radical polymerization and their use in the synthesis of metal nanoparticles. *Macromolecules* **36**, 9539-9548, doi:10.1021/ma035029c (2003).
- 130 Torchilin, V. P. Multifunctional, stimuli-sensitive nanoparticulate systems for drug delivery. *Nat. Rev. Drug Discov.* **13**, 813-827, doi:10.1038/nrd4333 (2014).
- 131 Kudina, O. *et al.* Highly efficient phase boundary biocatalysis with enzymogel nanoparticles. *Angew. Chem.-Int. Edit.* **53**, 483-487, doi:10.1002/anie.201306831 (2014).
- 132 Popat, A. *et al.* Mesoporous silica nanoparticles for bioadsorption, enzyme immobilisation, and delivery carriers. *Nanoscale* **3**, 2801-2818, doi:10.1039/c1nr10224a (2011).
- 133 Katz, E. & Willner, I. Integrated nanoparticle-biomolecule hybrid systems: Synthesis, properties, and applications. *Angew. Chem.-Int. Edit.* **43**, 6042-6108, doi:10.1002/anie.200400651 (2004).
- 134 Tokarev, A., Yatvin, J., Trotsenko, O., Locklin, J. & Minko, S. Nanostructured soft matter with magnetic nanoparticles. *Adv. Funct. Mater.* **26**, 3761-3782, doi:10.1002/adfm.201504443 (2016).

- 135 Hu, J. M., Zhang, G. Q. & Liu, S. Y. Enzyme-responsive polymeric assemblies, nanoparticles and hydrogels. *Chem. Soc. Rev.* **41**, 5933-5949, doi:10.1039/c2cs35103j (2012).
- 136 de la Rica, R., Aili, D. & Stevens, M. M. Enzyme-responsive nanoparticles for drug release and diagnostics. *Adv. Drug Deliv. Rev.* **64**, 967-978, doi:10.1016/j.addr.2012.01.002 (2012).
- 137 Stuart, M. A. C. *et al.* Emerging applications of stimuli-responsive polymer materials. *Nat. Mater.* **9**, 101-113 (2010).
- 138 Reddy, L. H., Arias, J. L., Nicolas, J. & Couvreur, P. Magnetic nanoparticles: Design and characterization, toxicity and biocompatibility, pharmaceutical and biomedical applications. *Chem. Rev.* **112**, 5818-5878, doi:10.1021/cr300068p (2012).
- 139 Mura, S., Nicolas, J. & Couvreur, P. Stimuli-responsive nanocarriers for drug delivery. *Nat. Mater.* **12**, 991-1003, doi:10.1038/nmat3776 (2013).
- 140 Katz, E., Lioubashevski, O. & Willner, I. Magnetic field effects on cytochrome c-mediated bioelectrocatalytic transformations. *J. Am. Chem. Soc.* **126**, 11088-11092, doi:10.1021/ja048699m (2004).
- 141 Katz, E., Weizmann, Y. & Willner, I. Magnetoswitchable reactions of DNA monolayers on electrodes: Gating the processes by hydrophobic magnetic nanoparticles. *J. Am. Chem. Soc.* **127**, 9191-9200, doi:10.1021/ja0517771 (2005).
- 142 Katz, E. & Willner, I. Switching of directions of bioelectrocatalytic currents and photocurrents at electrode surfaces by using hydrophobic magnetic nanoparticles. *Angew. Chem.-Int. Edit.* **44**, 4791-4794, doi:10.1002/anie.200501126 (2005).



- 143 Tam, T. K., Ornatska, M., Pita, M., Minko, S. & Katz, E. Polymer brush-modified electrode with switchable and tunable redox activity for bioelectronic applications. *J. Phys. Chem. C* **112**, 8438-8445, doi:10.1021/jp801086w (2008).
- 144 Weizmann, Y., Elnathan, R., Lioubashevski, O. & Willner, I. Endonuclease-based logic gates and sensors using magnetic force-amplified readout of DNA scission on cantilevers. *J. Am. Chem. Soc.* **127**, 12666-12672, doi:10.1021/ja0533287 (2005).
- 145 Hayashi, K. *et al.* Magnetically responsive smart nanoparticles for cancer treatment with a combination of magnetic hyperthermia and remote-control drug release. *Theranostics* **4**, 834-844, doi:10.7150/thno.9199 (2014).
- 146 Uline, M. J., Rabin, Y. & Szleifer, I. Effects of the salt concentration on charge regulation in tethered polyacid monolayers. *Langmuir* **27**, 4679-4689, doi:10.1021/la104906r (2011).
- 147 Halsey, T. C. & Toor, W. Fluctuation-induced couplings between defect lines or particle chains. *J. Stat. Phys* **61**, 1257-1281, doi:10.1007/bf01014374 (1990).
- 148 Furst, E. M. & Gast, A. P. Particle dynamics in magnetorheological suspensions using diffusing wave spectroscopy. *Phys. Rev. E* **58**, 3372-3376, doi:10.1103/PhysRevE.58.3372 (1998).
- 149 Gulley, G. L. & Tao, R. Structures of an electrorheological fluid. *Phys. Rev. E* **56**, 4328-4336, doi:10.1103/PhysRevE.56.4328 (1997).
- 150 Tan, Z. J., Zou, X. W., Zhang, W. B. & Jin, Z. Z. Structure transition in cluster-cluster aggregation under external fields. *Phys. Rev. E* **62**, 734-737, doi:10.1103/PhysRevE.62.734 (2000).

- 151 Silva, A. S., Bond, R., Plouraboue, F. & Wirtz, D. Fluctuation dynamics of a single magnetic chain. *Phys. Rev. E* **54**, 5502-5510, doi:10.1103/PhysRevE.54.5502 (1996).
- 152 Cheng, R., Zhu, L., Huang, W. J., Mao, L. D. & Zhao, Y. P. Dynamic scaling of ferromagnetic micro-rod clusters under a weak magnetic field. *Soft Matter* **12**, 8440-8447, doi:10.1039/c6sm01485b (2016).
- 153 Townsend, J., Burtovyy, R., Galabura, Y. & Luzinov, I. Flexible chains of ferromagnetic nanoparticles. *ACS Nano* **8**, 6970-6978, doi:10.1021/nn501787v (2014).
- 154 Motornov, M. *et al.* Field-directed self-assembly with locking nanoparticles. *Nano Lett.* **12**, 3814-3820, doi:10.1021/nl301780x (2012).
- 155 Wilhelm, S. *et al.* Analysis of nanoparticle delivery to tumours. *Nat. Rev. Mater.* **1**, Article number #16014, doi:10.1038/natrevmats.2016.14 (2016).
- 156 Sawant, R. M. *et al.* Nanosized cancer cell-targeted polymeric immunomicelles loaded with superparamagnetic iron oxide nanoparticles. *J. Nanopart. Res.* **11**, 1777-1785, doi:10.1007/s11051-009-9611-4 (2009).
- 157 Liao, C. D., Sun, Q. Q., Liang, B. L., Shen, J. & Shuai, X. T. Targeting EGFR-overexpressing tumor cells using Cetuximab-immunomicelles loaded with doxorubicin and superparamagnetic iron oxide. *Euro. J. Radiol.* **80**, 699-705, doi:10.1016/j.ejrad.2010.08.005 (2011).
- 158 Zhu, L. *et al.* Targeted delivery of methotrexate to skeletal muscular tissue by thermosensitive magnetoliposomes. *Int. J. Pharm.* **370**, 136-143, doi:10.1016/j.ijpharm.2008.12.003 (2009).
- 159 Yang, L. L. *et al.* Receptor-targeted nanoparticles for in vivo imaging of breast cancer. *Clin. Cancer Res.* **15**, 4722-4732, doi:10.1158/1078-0432.ccr-08-3289 (2009).

- 160 Liu, D. F. *et al.* Conjugation of paclitaxel to iron oxide nanoparticles for tumor imaging and therapy. *Nanoscale* **4**, 2306-2310, doi:10.1039/c2nr11918h (2012).
- 161 Bagalkot, V. *et al.* Quantum dot - Aptamer conjugates for synchronous cancer imaging, therapy, and sensing of drug delivery based on Bi-fluorescence resonance energy transfer. *Nano Lett.* **7**, 3065-3070, doi:10.1021/nl071546n (2007).
- 162 Karlsson, H. L., Gustafsson, J., Cronholm, P. & Moller, L. Size-dependent toxicity of metal oxide particles-A comparison between nano- and micrometer size. *Toxicol. Lett.* **188**, 112-118, doi:10.1016/j.toxlet.2009.03.014 (2009).
- 163 Villanueva, A. *et al.* The influence of surface functionalization on the enhanced internalization of magnetic nanoparticles in cancer cells. *Nanotechnology* **20**, doi:10.1088/0957-4484/20/11/115103 (2009).
- 164 Bumb, A. *et al.* Synthesis and characterization of ultra-small superparamagnetic iron oxide nanoparticles thinly coated with silica. *Nanotechnology* **19**, doi:10.1088/0957-4484/19/33/335601 (2008).
- 165 Deng, Y. H., Wang, C. C., Hu, J. H., Yang, W. L. & Fu, S. K. Investigation of formation of silica-coated magnetite nanoparticles via sol-gel approach. *Colloids Surf., A* **262**, 87-93, doi:10.1016/j.colsurfa.2005.04.009 (2005).
- 166 Jakubowski, W. & Matyjaszewski, K. Activator generated by electron transfer for atom transfer radical polymerization. *Macromolecules* **38**, 4139-4146, doi:10.1021/ma047389l (2005).
- 167 Miyajima, T., Mori, M., Ishiguro, S., Chung, K. H. & Moon, C. H. On the complexation of Cd(II) ions with polyacrylic acid. *J. Colloid Interface Sci.* **184**, 279-288, doi:10.1006/jcis.1996.0621 (1996).

- 168 Schiller, A. A., Schayer, R. W. & Hess, E. L. Fluorescein-conjugated bovine albumin - physical and biological properties. *J. Gen. Physiol.* **36**, 489-&, doi:10.1085/jgp.36.4.489 (1953).
- 169 Leermakers, F. A. M., Ballauff, M. & Borisov, O. V. On the mechanism of uptake of globular proteins by polyelectrolyte brushes: A two-gradient self-consistent field analysis. *Langmuir* **23**, 3937-3946, doi:10.1021/la0632777 (2007).